

Daisy-chained floating wind turbines

Jesper Tom Bryan

Delft University of Technology

This page is intentionally left blank

Daisy-chained floating wind turbines

by

Jesper Tom Bryan

to obtain the degree of Master of Science
at the Delft University of Technology,
to be defended publicly on the 15th of November, 2024.

Student number: 4579917
Project duration: 20th of April, 2024 – 8th of November, 2024
Thesis committee: Dr. J. O. Colomes Gene TU Delft supervisor
S. Agarwal MSc TU Delft supervisor
Prof. Dr. A. Metrikine, TU Delft
Dr. Ir. J. Breukels Allseas

Cover: J.T. Bryan (2023)

This page is intentionally left blank

Preface

This thesis was written and submitted to obtain the degree of Master of Science in Hydraulic and Off-shore Structures at Delft University of Technology. It was completed in the Innovations Department of Allseas Engineering B.V. As the cover depicts, with this thesis, the sun also sets on my time as a student at TU Delft. A time filled with ups and downs, learning moments, and, most importantly, memories that I look back on with a great deal of joy. The same goes for the last few months that I spent working on this thesis. This achievement wouldn't have been possible without the following people.

To start, I would like to thank my supervisors from TU Delft: Oriol Colomes, Shagun Agarwal, and Andrei Metrikine. I am grateful to Oriol and Shagun for our bi-weekly meetings and for providing me with insights, advice, and additional knowledge on the subject. Andrei, I would like to thank for his valuable feedback and reassurance during our progress meeting. An extra thanks goes to my fellow student Benjamin for his support and advice throughout my time as a student in Delft.

As mentioned, I conducted my research at Allseas, and this would not have been possible without the supervision of Jeroen Breukels. Jeroen guided me from start to finish with weekly meetings, through which I learned not only about the subject but also how to think and act like an engineer. I would also like to thank my colleagues for the wonderful time I had at the office and for their support. A special thanks goes to Max for all the lunches, coffee breaks, and Friday drinks. I look forward to starting my career next year at the Heavy Lift Department.

Finally, I would like to thank all my friends, my parents, my sister Lotte, and my girlfriend Sanne for believing in me and supporting me through this journey. Thank you all from the bottom of my heart. Without you, my studies and time in Delft wouldn't have been the life-changing experience it has been.

*Jesper Tom Bryan
Delft, November 2024*

This page is intentionally left blank

Abstract

The offshore wind industry has grown significantly since the installation of the first offshore wind farm in Vindeby, Denmark, in 1991. In recent years, the need to expand offshore wind capacity has led to an increased interest in floating offshore wind turbines (FOWTs), especially for deeper waters where bottom-fixed structures are impractical. This research explores the feasibility and behavior of daisy-chaining FOWTs to reduce mooring costs and anchor points, which currently account for a significant portion of installation expenses and are challenging to install.

The study focuses on spar-type FOWTs, investigating how daisy-chaining impacts the motion, stability, and mooring line forces in different wave and wind conditions. By conducting dynamic simulations with OrcaFlex software, two configurations, triangular and hexagonal, were analyzed to assess the effects of connecting multiple FOWTs. Results indicate that the daisy-chaining doesn't increase the amplitude of roll and pitch motions compared to a single FOWT, but the system is susceptible to resonance in high sea states, causing excessive yaw motions around the z-axis. These resonances occur due to certain modes in the system being excited by peak wave frequencies, leading to amplified loads.

Despite these challenges, the study demonstrates that daisy-chaining can be feasible if the mooring and connection line design parameters are optimized to avoid resonance issues. The forces experienced in the mooring lines were found to be well within the available safe working load of industry-standard steel wire ropes, but careful design considerations are necessary to mitigate fatigue and ensure stability. This research contributes to the limited literature on shared mooring systems for FOWTs and offers insights into potential cost saving and design strategies for future offshore wind farm projects.

Keywords: Floating Offshore Wind Turbines, Daisy-Chaining, Mooring Systems, Spar Floater

This page is intentionally left blank

Contents

Preface	ii
Nomenclature	xi
1 Introduction	1
1.1 Problem statement	1
1.2 Research objective	2
1.3 Scope	2
1.4 Research outline	3
2 Background	4
2.1 History of floating wind turbines	4
2.2 Substructures	4
2.3 Mooring lines	5
2.4 Anchors	8
3 Theory	10
3.1 Motions	10
3.1.1 Response amplitude operator	11
3.1.2 Stability	11
3.2 Waves	12
3.2.1 Wave period and height	12
3.2.2 Airy wave theory	13
3.2.3 JONSWAP spectrum	13
3.2.4 Dynamic loading	14
3.3 Wind loading	16
3.4 Mooring equations	17
3.4.1 Catenary mooring equations	18
3.4.2 Taut mooring equations	19
4 Method and model	21
4.1 Methodology	21
4.1.1 Multibody dynamics	21
4.1.2 Dynamic modeling of the mooring lines	21
4.1.3 Implicit integration scheme	22
4.1.4 Overview of the model	23
4.2 Model	23
4.2.1 Base case	23
4.2.2 Daisy-chained model	25
4.2.3 Load cases	26
5 Validation of the model	28
5.1 Hywind Scotland wind farm	28
5.2 Natural frequency of lines	32
5.3 Convergence study	33
6 Results	36
6.1 Design limitations	36
6.2 Yaw rotation	38
6.2.1 Viscous yaw damping	39
6.2.2 Crowfoot compared to single mooring line	40
6.2.3 Modes yaw movement	42

6.3	Comparison hexagonal configuration to a single wind turbine	44
6.4	Nacelle movements	46
7	Conclusion	51
8	Discussion and recommendations	53
	References	56
A	Elastic mooring equations	59
B	NREL 5MW and OC3 Hywind spar	61
B.1	NREL 5 MW wind turbine	61
B.2	Tower	62
B.3	OC3 Hywind spar floater	62
C	Load RAOs, added mass and damping matrices	64
C.1	Load RAOs	64
C.2	Added mass matrices	65
C.3	Damping matrices	66
C.4	Viscous damping matrix	67
D	Loadcases	68
E	Validation data	70
E.1	Environmental conditions for the validation cases	70
E.2	Loads in the delta lines	70
F	Results graphs	77
F.1	Graphs viscous damping	78
F.2	Spectral density graphs	79

List of Figures

1.1	Designs for offshore floating wind turbines (Principal power, 2013)[14]	1
2.1	Substructure types (DNVGL, 2018)[11]	4
2.2	Different types of chains (Damen, 2016)[8]	6
2.3	Polyester rope (Lankhorst, 2024)	7
2.4	Steel wire (Ma et al., 2019)[34]	7
2.5	Different types of anchors (Vryhof, 2015)[53]	8
3.1	Six degrees of freedom in a vessel (Tanaka, 2018)[51]	10
3.2	Stability of a floating structure (Sharma, n.d.)[46]	12
3.3	Definition of a wave as two downward zero-crossings (L. H. Holthuijsen, 2007)[25]	12
3.4	Surface elevation and corresponding Jonswap spectrum	14
3.5	Force regimes (Chakrabarti, 1987)[6]	15
3.6	Rated power and thrust curve [9]	16
3.7	Wind speed and pressure on an actuator disc (TU Delft, 2023) [9]	17
3.8	Types of mooring designs (Ma et al., 2019)[31]	18
3.9	Forces on an element of a mooring line (Ma et al., 2019)[32]	18
3.10	Geometry of a catenary line (Ma et al., 2019)[32]	19
4.1	Lumped mass model, (M. Hall, 2015)[22]	22
4.2	Overview of the multibody dynamic model	23
4.3	Base case, 5MW spar floater wind turbine	24
4.4	Base case mooring configuration	25
4.5	Daisy-chained configurations	26
4.6	Color coding of the different spar floaters with wind direction	26
5.2	Comparison inclination for real-life and simulations	30
5.3	Boxplots for the real-life data and the average COG simulations	30
5.4	Load in mooring line 2, delta line 1 for case 1	31
5.5	Load in mooring line 3, delta line 2 for case 1	31
5.6	Load in mooring line 1, delta line 1 for case 7	32
5.8	Difference for different node distances	33
5.9	Zoomed image for difference for node distances of 1 and 2 meter	34
5.10	Difference for different time steps	34
6.1	Design regions, water depth - rotor diameter relation	37
6.2	Rotation around the z-axis during an aborted simulation	38
6.3	Views of the swaying motion of the connection line	39
6.4	Yaw motion blue spar floater for different viscous damping	39
6.5	Yaw motion for different periods for mode 6 with crowfoot mooring for the base case	41
6.6	Yaw motion for different periods for mode 6 without crowfoot mooring for the base case	41
6.7	Yaw motion for periods of 16 and 17 seconds for mode 6 with and without crowfoot mooring	41
6.8	Yaw motion for periods of 16 and 17 seconds for mode 6 with and without crowfoot mooring	42
6.9	Spectral density yaw rotation for green and white spar floater in the hexagonal configuration.	43
6.10	Spectral density yaw rotation for the green spar floater in the triangular configuration for LC7 and LC9.	43
6.11	Acceleration and inclination for the nacelle for HLC1 and HLC3	46
6.12	Inclination for downwind and upwind nacelles at rated wind speed	47
6.13	Inclination for red nacelle for different EC directions	47

6.14	Inclination for all three nacelles for LC1 and LC3	48
6.15	Inclination for three load cases with different pretension	48
6.16	Spectral density yaw rotation for the green spar floater in the triangular configuration for LC7 and LC16.	49
A.1	Forces on an element of a mooring line with elasticity(Ma et al., 2019)[32]	59
B.1	Wind turbine system (A. Ross, 2018) [43]	62
B.2	Spar floater	63
E.1	Load in mooring line 1, delta line 1 for case 1	70
E.2	Load in mooring line 1, delta line 2 for case 1	71
E.3	Load in mooring line 2, delta line 1 for case 1	71
E.4	Load in mooring line 2, delta line 2 for case 1	71
E.5	Load in mooring line 3, delta line 1 for case 1	71
E.6	Load in mooring line 3, delta line 2 for case 1	72
E.7	Load in mooring line 1, delta line 1 for case 3	72
E.8	Load in mooring line 1, delta line 2 for case 3	72
E.9	Load in mooring line 2, delta line 1 for case 3	72
E.10	Load in mooring line 2, delta line 2 for case 3	73
E.11	Load in mooring line 3, delta line 1 for case 3	73
E.12	Load in mooring line 3, delta line 2 for case 3	73
E.13	Load in mooring line 1, delta line 1 for case 7	73
E.14	Load in mooring line 1, delta line 2 for case 7	74
E.15	Load in mooring line 2, delta line 1 for case 7	74
E.16	Load in mooring line 2, delta line 2 for case 7	74
E.17	Load in mooring line 3, delta line 1 for case 7	74
E.18	Load in mooring line 3, delta line 2 for case 7	75
E.19	Load in mooring line 1, delta line 1 for case 11	75
E.20	Load in mooring line 1, delta line 2 for case 11	75
E.21	Load in mooring line 2, delta line 1 for case 11	75
E.22	Load in mooring line 2, delta line 2 for case 11	76
E.23	Load in mooring line 3, delta line 1 for case 11	76
E.24	Load in mooring line 3, delta line 2 for case 11	76
F.1	Yaw motions for the three spar floaters in the triangular configuration with different viscous damping	78
F.2	Spectral densities Rz spar floaters hexagonal configuration	79
F.3	Spectral densities Rz spar floaters triangular configuration for two environmental directions 80	80

List of Tables

3.1	Degrees of freedom and motion	10
4.1	Mooring line parameters	25
4.2	Sea-states	27
4.3	Horizontal pretension for the base case	27
4.4	Horizontal pretension for the triangular configuration	27
5.1	Calculated COG	29
6.1	Period for mode 6 per mooring line length with crowfoot	40
6.2	Period mode 6 per mooring line length without crowfoot	40
6.3	Modes exciting the yaw movement in a hexagonal configuration	42
6.4	Modes exciting the yaw movement in a triangular configuration	43
6.5	inclination Hywind turbine model simulations	44
6.6	Wind direction for all eleven cases	45
6.7	Inclination 5MW wind turbine model simulations	45
6.8	Highest load in mooring lines in kN	45
6.9	Highest load in kilonewton in mooring and connection lines for rated wind speed	50
B.1	Data overview of the 5MW turbine	61
B.2	Properties of the 5MW blades	61
B.3	Drivetrain properties	61
B.4	Geometric properties of the tower	62
B.5	Physical properties of the tower	62
B.6	Spar floater geometric properties	62
B.7	Spar floater structural properties	63
B.8	Spar floater hydrodynamic properties	63
C.1	Haskind load RAOs	64
C.2	Diffraction load RAOs	65
D.1	Loadcases triangular configuration	68
D.2	Loadcases hexagonal configuration	69
D.3	Parameters for the loadcases	69
E.1	Environmental conditions for the validation cases	70

Nomenclature

Abbreviations

Abbreviation	Definition
BEM	Blade element momentum
COB	Center of buoyancy
COG	Center of gravity
DEA	Drag-embedded anchor
DNV	Det Norske Veritas
DOF	Degree of freedom
EC	Environmental condition
EOM	Equation of motion
FEM	Finite element method
FOWT	Floating offshore wind turbine
HLC	Hexagonal load case
IEA	International Energy Agency
JONSWAP	Joint North Sea Wave Project
LC	Load case
MBD	Multibody dynamics
MBL	Minimum breaking load
NREL	National Renewable Energy Laboratory
OC3	Offshore Code Comparison Collaboration
OD	Outer diameter
PM	Pierson-Moskowitz
QTF	Quadratic transfer function
RAO	Response amplitude operator
ROV	Remotely operated vehicle
Rz	Rotation around z-axis
SD	Spectral density
SWL	Still water level or Safe working load
TLP	Tension leg platform
VLA	Vertical load anchor

Symbols

Symbol	Definition	Unit
A_{WL}	Area water level	$[m^2]$
a	Wave amplitude	$[m]$
C_D	Drag coefficient	$[-]$
C_M	Inertia coefficient	$[-]$
C_P	Power coefficient	$[-]$
C_T	Thrust coefficient	$[-]$
D	Diameter	$[m]$
E	Energy	$[J]$
g	Gravitational acceleration	$[m/s^2]$
\overline{GM}	Metacentric height	$[m]$
H_s	Significant wave height	$[m]$

Symbol	Definition	Unit
h	Water depth	[m]
I_T	Transverse moment of inertia	[kg.m ²]
k	Wave number	[1/m]
P	Power	[W]
T	Thrust force or tension	[N]
T_S	Significant wave period	[s]
U	Wind speed	[m/s]
u	Water particle velocity	[m/s]
γ	Peak enhancement factor	[-]
η	Surface elevation	[m]
λ	Wave length	[m]
ρ	Mass density	[kg/m ³]
ω	Wave frequency	[1/s]
∇	Volume of displacement	[m ³]

1

Introduction

Since the construction of the first offshore wind farm in Vindeby, Denmark, in 1991 the offshore wind industry has grown annually. In 2023 alone, 10.8 GW of offshore wind energy was installed. It is projected that by 2030 the offshore wind energy supply will need to increase by 320 GW to reach the IEA's 2050 goals [21]. Currently there are four operational offshore floating wind farms with a combined production of 193 MW. Compared to the energy supplied by monopile or other bottom-fixed offshore wind turbines, this is a small amount. However, DNV predicts that by 2050 this amount will have grown to almost 270 GW [12].

One of the reasons for such growth in offshore floating wind farms is the limited suitable area to install bottom-fixed offshore wind farms. Various factors determine whether a location is suitable for an offshore wind farm. The water depth, it has to be close to populated land and the area has to have suitable winds. The largest limiting factor herein is the water depth, from a depth of more than 50 meters it becomes difficult and expensive to install bottom-fixed structures. When the water depth becomes too large other solutions need to be found such as floating wind turbines.

In this chapter the problem statement will be explained followed by the objective and scope of this research.

1.1. Problem statement

There are currently four commonly used types of FOWTs: TLP, semi-submersible, floating barge and spar designs, as seen in figure 1.1, apart from the floating barge design. The TLP uses one or multiple mooring lines connecting it to the seabed. For the semi-submersible, barge and the spar design at least three mooring lines are needed to keep the FOWT in place to prevent it from drifting.

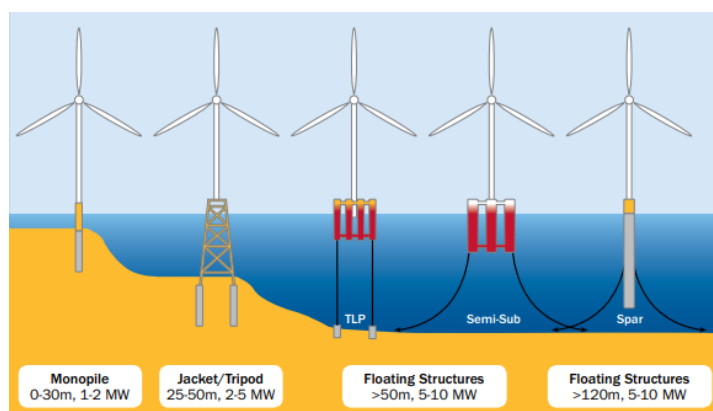


Figure 1.1: Designs for offshore floating wind turbines (Principal power, 2013)[14]

According to a report written by BVG Associates the costs for the mooring chains and anchors make up seven percent of all installation costs [4]. The largest portion of the costs go to the construction of the FOWT, with 27 percent and 22 percent allocated to the floating substructure and the nacelle, respectively. It is likely that the construction costs of these parts of the FOWT will increase in the future to be able to make larger structures capable of producing more power. However, it should be possible to save on mooring expenses. By using multi-line anchor points as proposed by C. Fontana the number of anchor points per turbine can be reduced by 60 percent [16]. Another way to save on expenses of anchors might be to connect FOWT to each other to keep the entire system stable. One of the main functions of mooring is to keep a FOWT from drifting by connecting it to an anchor, another function is that the weight helps as a dampener and a stiffness for motions. This secondary function doesn't specifically need the mooring line to be connected to an anchor on the seabed. An option could be to connect it to another FOWT so that the weight of the mooring line can keep them both stable. Another advantage would be that towing the system for installation, maintenance and decommissioning becomes easier. Instead of having to tow all FOWTs separately it might be possible to tow the system using fewer tugboats. There might be other methods than connecting floating wind turbines together that might be more cost effective like the multi-line anchor, however working this out is outside the scope of this research. Connecting FOWTs together will be called "daisy-chaining" throughout this report.

1.2. Research objective

The first objective of this research is to assess the effects that daisy-chaining FOWTs will have on the motions and the stability of the system. The second objective is to assess the feasibility of the system by verifying that the forces in the mooring chains don't exceed the safe working load (SWL). A literature gap review was done but no significant amount of research was found in the daisy-chaining of FOWT so this will therefore be a contribution to the existing knowledge. The only research that was found on this topic is from M.A. Van der Giessen who did a thesis on the feasibility of mooring optimization for floating wind turbines in deep water based on static analyses.[17] C. Schreuder did an evaluation of the feasibility of shared mooring systems on a combined solar and wind farm. [45]

To reach this objective a research question and multiple working questions are set-up that need to be answered:

How does daisy-chaining spar floaters influence the motion and stability response in a wind farm?

To find the answer to this question a set of working questions has been set-up.

1. *What parameters have influence on the motion response in a floating wind turbine farm?*
2. *How are the motions of a floating wind turbine influenced by connecting it to another floating wind turbine?*
3. *How do the motions and forces in the daisy-chained configuration compare to the base case?*
4. *What is the magnitude of the forces in the mooring and connection lines relative to the safe working load of available industry equipment?*

1.3. Scope

There are a large number of variables in a daisy-chained floating wind farm. The main groups into which these can be divided are the mooring, the FOWT design, the system configuration, and the external elements. To keep this research structured and specific, a scope needs to be set to limit the number of variables and establish boundary conditions. For the mooring, the type of line will remain constant in the model. This includes the weight and drag coefficient. The minimum breaking load (MBL) isn't relevant in the model because lines can't break within it; however, it should still be verified that the loads in the lines don't exceed this value. The main variable in the mooring is the length of the line, as altering it changes the pretension in the line. For the FOWT a public available model is used supplied

by Orcina, which is the company behind OrcaFlex software. More on this is explained in chapter 4. There are two models available, a semi-submersible and a spar floater type. The spar floater design has been chosen to limit the number of simulations to be run. Two configurations are chosen to be examined: a triangular configuration and a hexagonal configuration. Each configuration has a single mooring line leading outwards towards the seafloor. Figure 4.5 in section 4.2.2 shows a top view of these configurations and explains why these have been chosen. Finally, the external factors need to be determined. The main parameters are the wave and wind conditions, these have the most influence in deep water. Current has a relatively low velocity in deep water, for that reason it will be neglected. The water depth will also be set to a certain level and will not be changed.

1.4. Research outline

This thesis consists of the following chapters. Chapter two starts by providing a comprehensive background on floating wind turbines, looking at their historical development, substructures, mooring lines, and anchoring systems. Chapter three then delves into the theoretical aspects, covering the motions of floating structures, wave interactions, wind effects, and mooring dynamics. Chapter four employs a detailed methodological approach, utilizing multibody dynamics (MBD) and modeling techniques to simulate different configurations and load cases. Chapter five validated the model using data from the Hywind Scotland wind farm and a convergence study is conducted. In chapter six the results are analyzed to assess design limitations, yaw movements and nacelle responses. Chapter seven gives a conclusion to the thesis by answering the research and working questions. Finally, chapter eight offers a discussion and recommendations for future work.

2

Background

This chapter provides background information on FOWTs, including a brief history, the different types of FOWTs, as well as the types of mooring lines and anchors used in the offshore industry.

2.1. History of floating wind turbines

This section provides a brief history of FOWTs to illustrate how far the industry has progressed in the past decades since the first prototype was launched. The first prototype was built in 2007 off the coast of Italy and was decommissioned in 2008. It was used to gather test data on wind and sea conditions [42]. A year later, in 2009, the first commercial floating wind turbine became operational in the North Sea near the coast of Norway. It is still operating in 2024 and has withstood wind speeds of up to 30 m/s and wave heights of 19 meters [13]. In 2011, a full-scale prototype was installed in Portugal but was later decommissioned in 2016. Japan built a floating prototype in 2013, and China followed in 2021 with a 5.5 MW turbine near a larger bottom-fixed park. Spain installed its first FOWT in 2023 and connected it to their power grid. However, these are all single wind turbines built as prototypes or tests. Currently, there are four active floating offshore wind farms in Europe: two in Scotland, one in Portugal, and one in Norway, with a total capacity of 193 MW. The first park was commissioned in 2017 in Scotland.

2.2. Substructures

There are two different types of substructures used in existing wind parks: the spar type and the semi-submersible platform. Additionally, there are two other types for which prototypes have been developed: the barge and the TLP. All types can be seen in Figure 2.1.

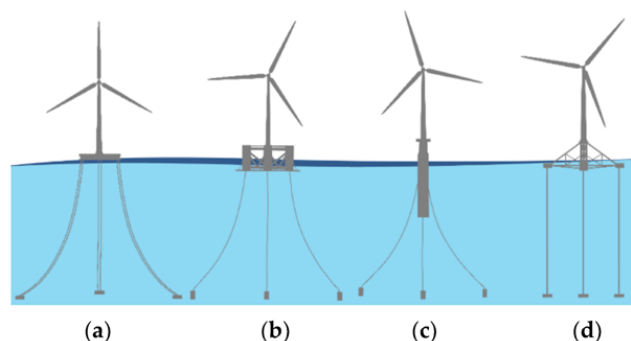


Figure 2.1: Substructure types (DNVGL, 2018)[11]

Barge type (a)

Barge types are similar to the semi-submersible platform. It consists of a circular or square shaped moon pool. The barge has a large floating area to achieve stability. It has a low draft which makes it easier to tow in shallow waters. These floaters are relatively inexpensive to construct and easy to tow to different locations. However, they are less suitable for deep-water applications because they are more susceptible to wave and wind forces. Currently there is a prototype built in Japan. [44]

Semi submersible platform (b)

The Kincardine and WindFloat Atlantic farms in Scotland and Portugal, respectively, utilize a semi-submersible platform as their substructure. This platform consists of three or four wide legs spread out to create a large second moment of inertia, which helps prevent the FOWT from tipping. Their design minimizes wave impact, allowing operations to continue in harsh weather conditions. However, these platforms are more complex and expensive to build and maintain compared to other types of floating structures.

Spar Type (c)

The Hywind parks, with one located in Scotland and the other in Norway, both utilize spar-type substructures. Spar structures consist of a tall cylindrical housing with dense ballast at the bottom to counteract pitching and rolling motions, thereby maintaining stability. They are particularly well-suited for deep-water environments due to their ability to remain steady even in extreme wave conditions. However, the main disadvantage is their high construction and installation costs.

Tension Leg Platform (d)

TLP designs are stabilized by a tensioned mooring system. When the structure shifts, the tensioned mooring generates a counterforce to stabilize the platform. This tension arises from the significant buoyancy of the design. TLPs are ideal for deep-water applications, as they can handle large vertical and horizontal loads. Despite their advantages, TLPs are costly to design, construct, and install, and their tendons require careful maintenance to ensure long-term reliability.

2.3. Mooring lines

There are different types of commonly used mooring lines. Chain, steel wire rope and polyester rope. It is possible to combine these different types into one mooring line. Each type has its advantages and disadvantages.

Chain

There are two different types of steel chains: studless and stud link. A stud link chain has a horizontal steel bar in each link, as seen in Figure 2.2b. This stud provides additional strength and weight, and it also serves to prevent entanglement of the chain while retrieving it. For this reason, stud link chains are more commonly used for temporary offshore projects. The main parameters of the chains which define the MBL are their diameter and steel grade. Damen provides an overview of different chains along with their respective MBL values [8].

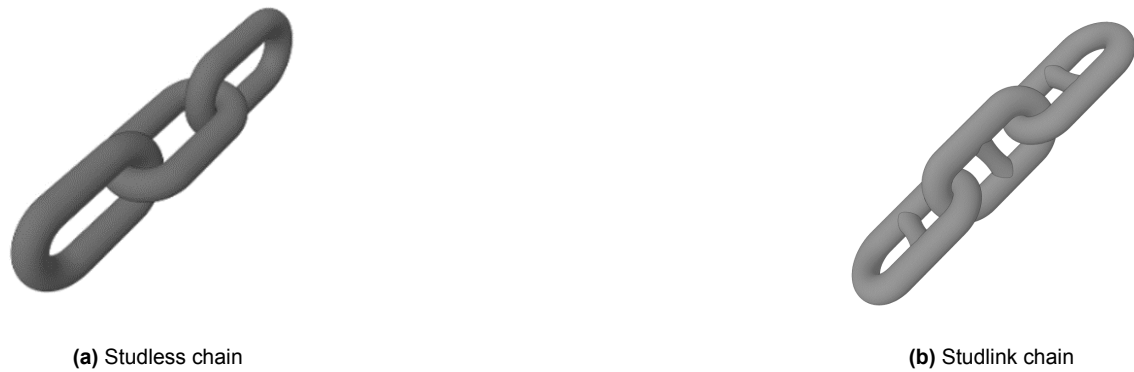


Figure 2.2: Different types of chains (Damen, 2016)[8]

Polyester rope

Polyester rope has emerged as the preferred choice for deepwater permanent mooring applications due to its light weight and high elasticity. This elasticity allows for the use of taut mooring systems in deep and ultradeep water, eliminating the need for catenary compliance to limit dynamic tensions typically caused by vessel motions from waves. It has been extensively employed in permanent moorings at depths ranging from 1000 to 3000 meters. In such depths, polyester mooring systems can maintain a smaller vessel offset compared to steel chain-wire-chain systems. Additionally, polyester ropes can sometimes reduce the number of mooring lines needed to achieve the same performance as chain-wire-chain systems for similar facilities [34].

The advantages of polyester moorings include reduced hull structural costs due to smaller vertical loads and a decrease in extreme line dynamic tension due to lower stiffness. Overall, polyester rope offers four main benefits: reduced vessel offset, a smaller mooring footprint, improved vessel payload capacity, and excellent fatigue properties. Beyond permanent moorings, polyester ropes are increasingly used in preset moorings and in extending the water depth range for mobile offshore drilling units.

Polyester ropes are typically constructed from multiple smaller subropes arranged in a parallel configuration. These subropes are wrapped with a soil filter to prevent soil ingress and enclosed in a protective jacket to guard against wear as illustrated in figure 2.3. The bundle of subropes forms a core that withstands tensile loads, while the jacket is non-load-bearing.

The subropes can be constructed in different ways: parallel, braided, or laid. The choice of construction depends on specific requirements. Parallel strand construction keeps load-bearing yarns aligned with the rope axis, resulting in minimal interaction between fibers or strands and thus achieving higher strength efficiency. A slight twist might be added to provide structure to the yarns and strands, enhancing load sharing among the rope components. Braided ropes feature half the strands oriented clockwise and the other half counterclockwise, resulting in a rotation-free rope with excellent handling characteristics. However, the point contact between strands can affect fatigue and strength. Laid subropes have all strands oriented in one direction, creating line contact between strands, which offers excellent fatigue performance in both tension and bending but can cause the rope to rotate under load. This rotation can be mitigated in laid ropes by using non-rotating designs, similar to steel wire ropes.

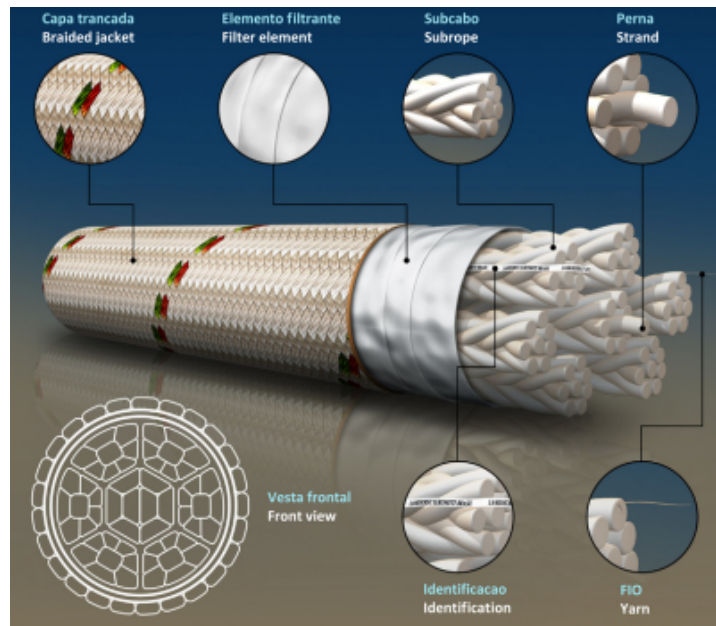


Figure 2.3: Polyester rope (Lankhorst, 2024)

There are also other types of synthetic ropes that are used in the industry but are less common. These include nylon, high modulus polyethylene, aramid and more. Polyester is the most used due to its low cost, light weight, low axial stiffness and good fatigue properties. [34]

Steel wire rope

Steel wire ropes are lighter and more elastic than chains with the same breaking load, making them preferable for mooring lines in deeper water where all-chain designs become too heavy. Common wire ropes used in offshore mooring lines include six-strand, eight-strand, and spiral strand types, as depicted in figure 2.4. The six-strand and eight-strand ropes are more flexible, allowing them to bend easily on sheaves, making them ideal for temporary moorings. Spiral strand ropes, which are torque neutral and can have a protective polyurethane sheath, are better suited for permanent mooring.

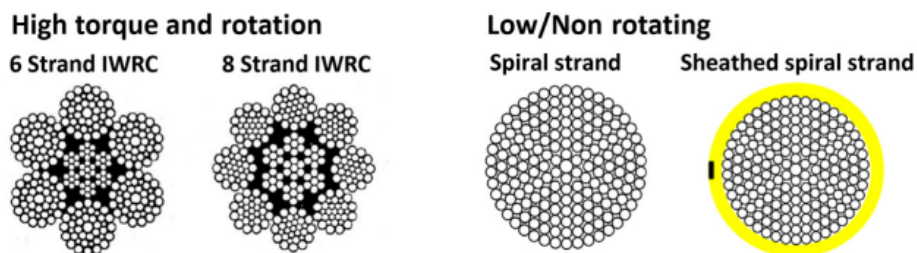


Figure 2.4: Steel wire (Ma et al., 2019)[34]

For corrosion resistance in permanent mooring, high-density polyethylene or polyurethane jacketing is typically used. These jackets, usually yellow for better underwater visibility as shown in figure 2.4, protect the wire ropes. Additionally, all wires can be galvanized, either with or without the use of sheathing. Zinc filler wires may also be incorporated to provide extra corrosion protection. A blocking compound, essentially grease, is used as a lubricant and to fill the spaces between the wires, minimizing the spread of corrosion due to saltwater ingress.

2.4. Anchors

Anchors are crucial components in marine and offshore engineering, providing stability to vessels and structures. The right anchor must be chosen based on specific conditions to ensure safety and functionality. For instance, in shallow waters with firm soil, simpler and less expensive anchors might be sufficient. Conversely, in deep waters with soft soil, more advanced and robust anchoring systems are necessary to withstand the greater loads and challenging conditions. The choice of anchoring is primarily influenced by several key factors: the depth of the water, soil conditions, and the load the anchor must support. As water depth increases and the mooring location becomes more remote, other factors such as environmental conditions, loads and the practicality and cost of transporting and installing the anchor point become significant considerations. Figure 2.5 categorizes the main types of anchor points according to water depth (from shallow to ultra-deep water) and soil type (from hard to soft soil).

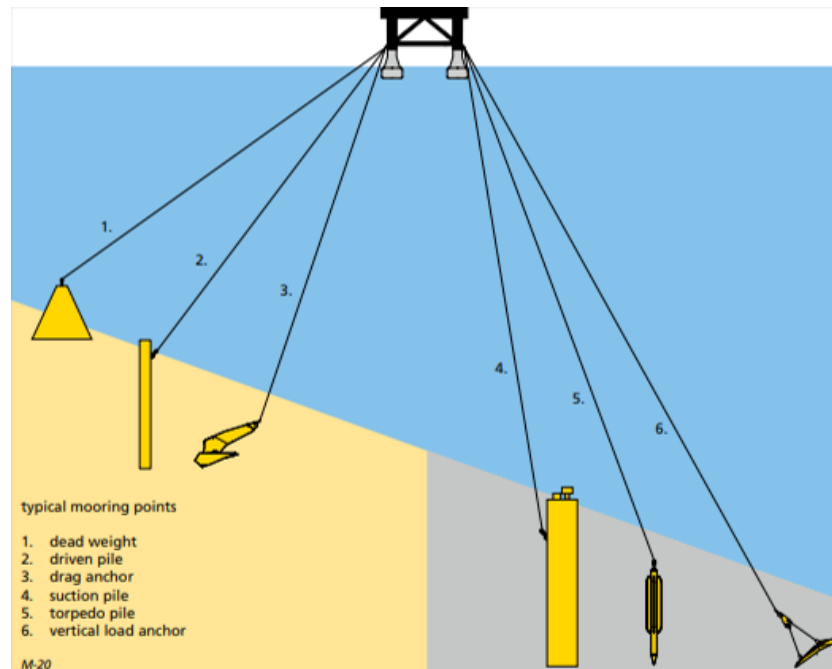


Figure 2.5: Different types of anchors (Vryhof, 2015)[53]

Dead weight anchor (1)

Dead weight anchors, also known as gravity anchors, are a type of anchoring system that relies on their mass to provide holding power. These anchors are typically made from heavy materials such as concrete, steel, or other dense substances. They are used in various marine and offshore applications where simplicity and reliability are essential. One of the primary advantages of dead weight anchors is their simplicity of design and installation. These anchors are straightforward to fabricate, with fewer mechanical parts, which reduces the likelihood of malfunction. Installation is relatively simple, often requiring just the placement of the anchor at the desired location. This makes them suitable for emergency or temporary anchoring needs. Since they rely on sheer weight, they remain extremely stable once positioned. This stability makes them less susceptible to shifting due to changes in soil or underwater currents, and their performance is predictable, which is critical in environments where precise holding capacity is essential. Dead weight anchors can be used in different soil types, including rocky, sandy, or muddy seabeds. However, in very soft soils they have the risk of partially sinking. Dead weight anchors are capable of withstanding both vertical and horizontal loads.

Driven pile (2)

Driven piles are large diameter (1-3 meters) open-ended pipes that are relatively simple to fabricate. They can be installed in a wide range of soil conditions and can be driven 100 meters or more into the seabed. At these depths, they can engage the high soil strengths, allowing them to develop very large uplift resistances. This makes them particularly well-suited for TLP support, which requires direct

uplift capabilities. Additionally, driven piles can handle horizontal or inclined loads, making them a good option for taut or catenary mooring systems. However, as pile hammer-driving and handling become more challenging in deeper water, driven piles are less common for ultra-deepwater applications. Despite these challenges, this method has been successfully used in water depths of up to 2400 meters [33]. The installation of driven piles creates a lot of noise and disturbances for surrounding marine wildlife. Solutions for this problem exist such as liquefying the soil within the pile to reduce resistance or by vibratory driving.

Drag-embedded anchor (3)

The DEA is widely used due to its simple installation, cost-effectiveness, and strong performance. It consists of a bearing plate attached to a shank connected to the mooring line, which ensures self-embedment by dragging the anchor through the soil. Initially designed for temporary moorings, DEAs have been improved for permanent use, although they typically have lower vertical capacity compared to horizontal capacity, depending on soil type and penetration depth. DEAs are best suited for catenary mooring systems but offer relatively low positioning accuracy during installation compared to suction and driven piles. Despite this, they are easy to install and provide a high holding capacity relative to their weight. Modern DEAs feature adjustable bearing plate-shank angles for different soil types, enhancing their efficiency in various conditions. Advances in DEA technology have led to the development of fixed bearing plate DEAs, which offer significantly higher holding capacities and reliability in soft soils.

Suction pile (4)

Suction piles are similar to driven piles except for the installation technique. The pile has a cap on the top with a system to be able to pump water through. They are driven for the first few meters or use their own gravity to sink through the soil. When the pile is at a sufficient depth a remotely operated vehicle (ROV) connects to the cap and pumps the water out. Due to the negative pressure, the pile pulls itself deeper into the soil. This type of anchor is well suited for vertical and horizontal loads and is possible to install at large water-depths. The advantage of the suction pile compared to the driven pile is the mitigated noise and vibrations.

Torpedo pile (5)

Torpedo piles, also known as drop anchors, penetrate the seabed through the kinetic energy gained from their free fall. This method reduces installation time and does not require vessels with significant bollard pull. They typically are cylindrical with a nose cone and stabilizing fins. They are suitable for soft to medium clay, torpedo anchors embed deeply and can resist both horizontal and vertical loads, making them ideal for catenary and taut mooring systems. The anchor's orientation post-installation is not a concern due to the padeye design, which accommodates mooring line loads in any direction. The torpedo anchor developed by Petrobras, is a notable example [37]. It measures approximately 20 meters in length, 1 meter in diameter, and weighs up to 120 metric tons. Dropped from a height of 100 meters above the seabed, it reaches terminal velocities of 30-50 meters per second. Installation typically requires two vessels, but Petrobras has used a single anchor handling vessel with the assistance of a ROV. This innovative and economical anchor has been successfully used for permanent mooring systems offshore Brazil.

Vertical load anchor (6)

The VLA functions similarly to a conventional DEA but is designed to penetrate much deeper into the seabed. It transitions from an installation mode to a vertical loading mode, allowing it to withstand both horizontal and vertical loads effectively. While primarily intended for deep-water mooring, its omnidirectional load capacity makes it suitable for use near pipelines and cables in confined subsea environments. To improve pullout resistance in soft clay, VLAs have been developed with a releasable shank that can be deployed after installation. They typically use a shear pin or mechanical release mechanism to ensure proper deployment. VLAs are effective in soft clay or layered soil conditions but are not recommended for use in sand or stiff clay. Capacity prediction methods for VLAs often rely on charts that estimate ultimate pull-out capacity and installation loads based on factors such as bearing plate area and mooring line diameter. However, these methods involve significant uncertainties. Predicting anchor trajectory during installation is crucial, typically done through empirical correlations or detailed geotechnical analysis of the anchor system and installation scenario [33].

3

Theory

3.1. Motions

There are six motions for floating rigid bodies. Three translational motions, surge, sway and heave and three rotational motions, roll, pitch and yaw. They are given in table 3.1. These motions occur due to loading of the structure due to waves, wind and current. Each motion can be visualized as a degree of freedom (DOF) as shown in figure 3.1. The motions can be assessed in the frequency domain by a frequency domain analysis and in the time domain by a time domain analysis. The time domain can be defined by the Equation of motion (EOM) given in equation (3.1).

Table 3.1: Degrees of freedom and motion

DOF	1	2	3	4	5	6
Motion	Surge	Sway	Heave	Roll	Pitch	Yaw

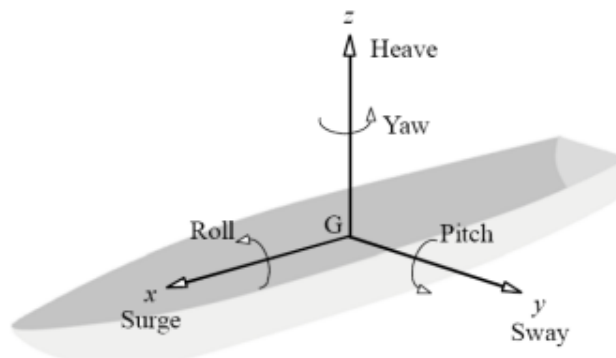


Figure 3.1: Six degrees of freedom in a vessel (Tanaka, 2018)[51]

$$(M + A(\omega))\ddot{x}(t) + B(\omega)\dot{x}(t) + Kx(t) = F(t) \quad (3.1)$$

Here M and A are the 6 by 6 mass and added mass matrices, B is the damping matrix, K is the stiffness matrix and $F(t)$ is the time dependent external environmental forcing vector. x , \dot{x} and \ddot{x} are respectively displacement, velocity and acceleration. The added mass in the EOM is due to the mass of the water displaced during the movements of the rigid body. It is frequency dependent and often represented by the coefficient C_M in the Morison equation as shown in equation 3.22. The damping is

due to the effects of the fluid flowing around the structure, which are also frequency-dependent.

The 6 by 6 stiffness matrix is influenced by the mooring and buoyancy of a floating body depending on the DOF. If a moored floating body is displaced the mooring will have a counteracting restoring force, this force can be seen as a spring acting on the body. This force is dependent of the amount of displacement. For a free floating body the buoyancy of the structure acts as the restoring spring stiffness for the 3rd, 4th and 5th DOFs .

It is possible to write the EOM in the frequency domain. Displacement, velocity and acceleration are expressed in terms of a sine wave. Equation 3.2 shows this.

$$-\omega^2(M + A)\tilde{x}e^{i\omega t} + i\omega B\dot{\tilde{x}}e^{i\omega t} + K\tilde{x}e^{i\omega t} = Fe^{i\omega t} \quad (3.2)$$

3.1.1. Response amplitude operator

In the field of ship design and other floating structures, the term response amplitude operator (RAO) is used to describe the likely behavior of the structure when operating under conditions with a specific frequency. It is a frequency-domain representation that quantifies how a floating structure responds to wave excitation at different frequencies. For DOFs 1-3, the RAO is given in kN/m for each frequency. This can be interpreted as the amount of force on the structure per meter of wave height at a specific wave period. The unit of $kN.m/m$ is used for the three rotational DOFs. The RAO for different frequencies can be determined by rewriting equation 3.2. Assuming $x = \tilde{x}e^{i\omega t}$ and $\zeta = \zeta_a e^{i\omega t}$ with ζ_a being the wave amplitude, the RAO can be found using the following equation [15].

$$RAO(\omega) = \frac{F_0}{K - (M + A(\omega))\omega^2 + iB(\omega)\omega} = \frac{x}{\zeta_a} \quad (3.3)$$

F_0 is the linear complex excitation force amplitude per wave height.

3.1.2. Stability

A floating structure can be in a stable, unstable and neutral state. This applies to vessels, as well as to FOWTs, floating oil rigs, icebergs and any other floating rigid body. A stable condition occurs when, after being rotated around a certain axis, the structure returns to its original position due to counteracting buoyancy forces. An unstable condition arises when the structure is rotated and does not return to its original state but continues to rotate and eventually turns over. A neutral state exists when, after being rotated, the structure remains in that position. A structure is considered stable when the metacenter is located above the center of gravity (COG) of a structure or the metacentric height, GM , is positive. The metacenter is the intersection between the centerline of the structure through the COG and the upward line through the center of buoyancy (COB). Figure 3.2 shows an example of a stable ship with the GM being positive. The formula for the metacentric height for small angles (less than 5°) is as follows:

$$GM = KB + BM - KG \quad (3.4)$$

$$BM = \frac{I_T}{\nabla} \quad (3.5)$$

Here KB is the height of the center of buoyancy above the keel, BM is the distance between the center of buoyancy and the metacenter and KG is the distance from the keel to the center of gravity. BM can be calculated by dividing the transverse moment of inertia (I_T) by the volume of displacement (∇).

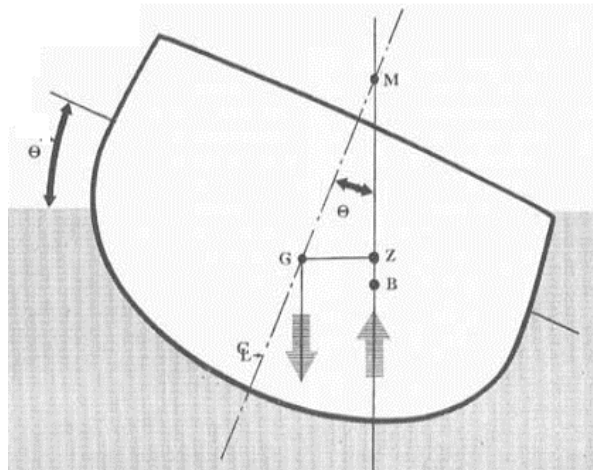


Figure 3.2: Stability of a floating structure (Sharma, n.d.)[46]

The buoyancy stiffness is represented in the EOM in the K matrix for the 3rd, 4th and 5th degree as a function of the wet surface or the metacentric height. This is shown in equation (3.6) as stated by J.M.J. Journée [29].

$$k_{33} = \rho g A_{WL} ; k_{44} = \rho g \nabla \overline{GM} ; k_{55} = \rho g \nabla \overline{GM}_L \quad (3.6)$$

3.2. Waves

There are two types of waves, wind waves and swell waves. Wind waves are generated by wind blowing over the water surface in the near vicinity. They are also called sea waves or local waves. Swell waves are waves created by a storm in another system far away. They travel to the local system and are not affected by the local wind blowing over the water surface. Swell waves tend to have a higher and more regular peak period. This section elaborates on the period and height for waves and the different theories to describe them.

3.2.1. Wave period and height

A wave is defined as the profile of the surface elevation between two downward zero-crossings of the elevation [25]. The surface elevation is the height at a certain instance and thus not the same as the wave height as seen in figure 3.3. The wave period is the time between these two zero-crossings, the wave height is the distance between the lowest and highest surface elevation of a certain wave.

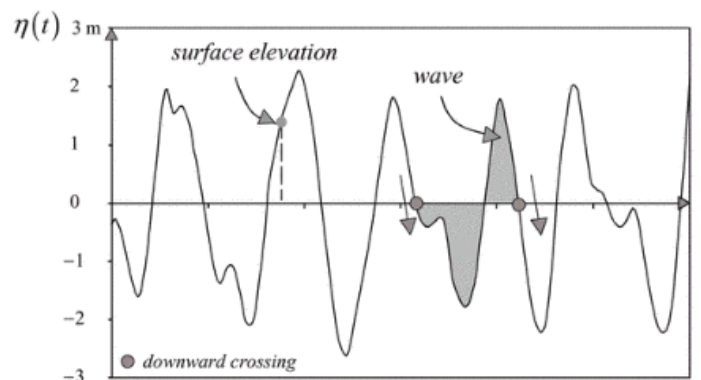


Figure 3.3: Definition of a wave as two downward zero-crossings (L. H. Holthuijsen, 2007)[25]

For most applications with waves the significant wave height (H_s) is determined. H_s is the average of

the largest third of all the waves. For reliable results at sea, a time frame of 15-30 minutes is commonly used. The same method can be applied to find the significant wave period. Both formulas can be written as:

$$H_s = \frac{1}{N/3} \sum_{j=1}^{N/3} H_j \quad (3.7)$$

$$T_s = \frac{1}{N/3} \sum_{j=1}^{N/3} T_{0,j} \quad (3.8)$$

3.2.2. Airy wave theory

Airy wave theory is a simplified theory to describe waves. It assumes the wave as a sinusoidal linear wave. For ocean waters or deep seas it is assumed that the sea bed does not affect the waves. The formula for the surface elevation at a certain location and time is given in equation 3.9.

$$\eta(x, t) = a \sin(\omega t - kx) \quad (3.9)$$

Here a is the amplitude of the wave, k is the wavenumber which can be expressed in deep waters as equation 3.10 where λ is the wave length, ω is the wave frequency which can be expressed as equation 3.11.

$$k = \frac{2\pi}{\lambda} \quad (3.10)$$

$$\omega = \frac{2\pi}{T} \quad (3.11)$$

For water waves, but also with other physical phenomena, propagating waves with a non-zero amplitude have their wave frequency, ω and wavenumber, k , satisfy a functional relationship. This is called the dispersion relation. For these waves this is given in equation 3.12 and 3.13. Where h is the water depth.

$$\omega^2 = g k \tanh(kh) \quad (3.12)$$

$$\lambda = \frac{g}{2\pi} T^2 \tanh\left(2\pi \frac{h}{\lambda}\right) \quad (3.13)$$

From equation 3.9 it is possible to take the velocity potential functions and eventually the particle velocities in a sideways and upwards direction as given in equations 3.14 and 3.15. These are of importance in section 3.2.4

$$u_x = \omega a e^{kz} \sin(\omega t - kx) \quad (3.14)$$

$$u_z = \omega a e^{kz} \cos(\omega t - kx) \quad (3.15)$$

3.2.3. JONSWAP spectrum

In the offshore industry, irregular wave spectra are used to determine the environmental loading. The irregular wave spectrum is a summation of a finite number of Fourier components to obtain the surface elevation $\eta(t)$, as shown in equation 3.16 and figure 3.4a, here ω_j is a fixed frequency, a_j is the amplitude determined from the assumed energy spectrum of which the corresponding spectrum to the time series in figure 3.4a is given in figure 3.4b and ϵ_j is a random phase.[52]

$$\eta(t) = \sum_{j=1}^N a_j \sin(\omega_j t + \epsilon_j) \quad (3.16)$$

$$a_j = \sqrt{2S(\omega_j)\Delta\omega_j} \quad (3.17)$$

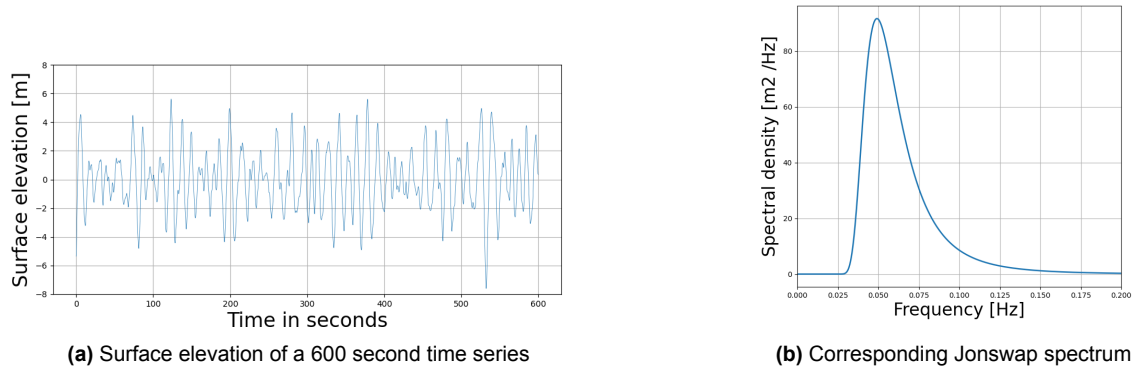


Figure 3.4: Surface elevation and corresponding Jonswap spectrum

The expression $S(\omega_j)$ is the energy spectrum of the environment. There are a lot of different spectra that are used but the most common ones are the Pierson-Moskowitz (PM) and the Joint North Sea Wave Project (JONSWAP) spectrum. JONSWAP is for still developing seas and PM is used for fully developed seas. These two spectra have the same formula but the JONSWAP has an extra peak enhancement parameter γ as can be seen in equation 3.18. [24]

$$S_j(\omega) = \frac{\alpha g^2}{16\pi^4} \omega^{-5} \exp\left[-\frac{5}{4}\left(\frac{\omega_p}{\omega}\right)^4\right] \gamma^r \quad (3.18)$$

$$r = \exp\left[-\frac{(\omega - \omega_p)^2}{2\sigma^2\omega_p^2}\right] \quad (3.19)$$

Where:

- ω is the wave frequency
- α is the spectral energy parameter
- g is the acceleration due to gravity
- ω_p is the peak frequency
- γ is the peak enhancement factor, normally taken as 3.3
- σ is the spectral width parameter
 - $\sigma = 0.07$ if $\omega \leq \omega_p$
 - $\sigma = 0.09$ if $\omega > \omega_p$

α can be defined by following equation where U_{10} is the ten meter high wind speed and F is the distance from the lee shore.

$$\alpha = 0.076 \left(\frac{U_{10}^2}{Fg}\right)^{0.22} \quad (3.20)$$

3.2.4. Dynamic loading

The force on a structure is due to the hydrostatic force, the drag force, the inertia force and the viscous friction force as seen in equation 3.21. The viscous force is often neglected.

$$F(t) = F_h + F_d(t) + F_i(t) + F_v(t) \quad (3.21)$$

To determine which parts need to be included in the formula it must be determined in which force regime it falls. The force regimes are shown in figure 3.5. This is a function of the wave height, the diameter of the structure and the wave lengths.

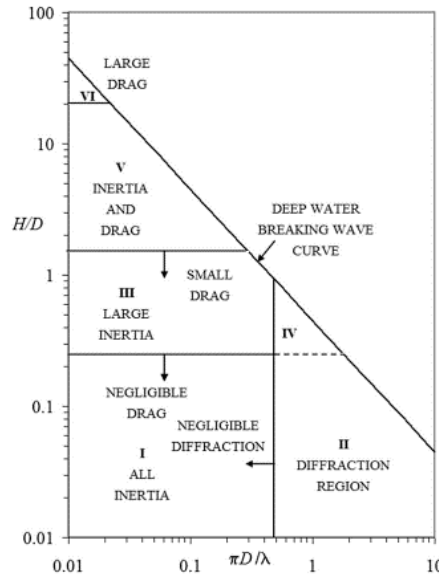


Figure 3.5: Force regimes (Chakrabarti, 1987)[6]

Diffraction and radiation

If an object falls in Region II, the forces are calculated using the EOM. These forces are due to Froude-Krylov incident waves and diffraction forces. Diffraction occurs when waves bounce off the impermeable structure. Radiation forces are accounted for on the left side of the EOM. The radiation problem represents the structure moving with the frequency of the incoming wave field, assuming no waves are present. The movement of the structure generates waves on its own, thereby producing the added mass, damping, and hydrostatic restoring coefficients in the EOM [45].

Morison equation

In the other regimes diffraction and radiation can be neglected. This is usually the case in slender structures such as mooring lines and jacket tower legs. The forces are then calculated with the Morison equation given in equation 3.22. The first part is the inertia force and the second part is the drag force. Depending on which regime the structure falls one of these two can then sometimes be neglected.

$$dF = \rho C_M \frac{\pi D^2}{4} \dot{u} dz + \frac{\rho}{2} C_d D |u| u dz \quad (3.22)$$

The inertia coefficient C_M and the drag coefficient C_D are dependent on the material properties and the shape of the structure. The water particle velocity u has been established in section 3.2.2. However, this is assuming that the waves are regular airy waves as described in section 3.2.2, if this is not the case, a wave force spectrum, $S_F(f)$ should be determined. This can be done by multiplying the wave spectrum by the square of the wave force ratio or RAO, which can be calculated by equation 3.23[3]. Equation 3.24 shows the relationship.

$$RAO = \rho V (1 + C_m) g k \frac{\cosh k(z+h)}{\cosh kh} \quad (3.23)$$

$$S_F(f) = (f_w(f))^2 S_{JONSWAP}(f) \quad (3.24)$$

The force amplitude then becomes:

$$F_{Amp} = 2 \sqrt{\int_f S_F(f) df} \quad (3.25)$$

The wave forces are parameters on the right hand side of the EOM.

3.3. Wind loading

This section will elaborate on how wind forcing is incorporated into the EOMs. To begin with, it is important to understand the wind speeds at which a wind turbine operates. The three main terms for wind speeds relevant to a wind turbine are the cut-in wind speed, the rated wind speed, and the cut-out wind speed.

The **cut-in wind speed** is the minimum wind speed required for the turbine to start turning its blades and begin producing power. The **rated wind speed** is the wind speed at which a control system is activated to limit the aerodynamic forces on the blades, ensuring that the power generated remains constant by adjusting the blade pitch angle. The **cut-out wind speed** is the point at which the blades are turned into the wind, and the turbine is stopped to prevent damage.

These speeds might vary slightly for different wind turbines, but they are generally quite similar. In Figure 3.6a, the relationship between wind speed and power production is shown. The rated wind speed is also indicated on the graph. At the rated wind speed, the turbine cannot produce more power than its rated capacity; exceeding this could cause damage. Figure 3.6b illustrates the thrust curve, showing that the maximum thrust force is generated at the rated wind speed. This is due to the pitch control system being activated as the wind speed increases, which helps reduce the force on the rotor.

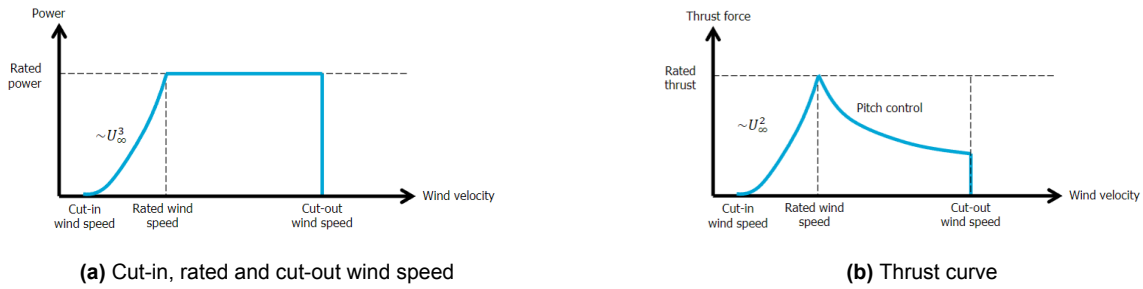


Figure 3.6: Rated power and thrust curve [9]

Wind turbines extract kinetic energy from wind and with a rotor and generator converts it into electrical energy. Wind exerts a thrust force on the nacelle through the rotor blades and a drag force on the tower. The thrust force can be derived from a one-dimensional momentum theory. The laws of conservation for energy and mass are used. These two laws are respectively:

$$E = \frac{1}{2}\rho U^2 + p + \rho gh = \text{constant} \quad (3.26)$$

$$\dot{m} = \rho AU = \text{constant} \quad (3.27)$$

Using the law of conservation of mass and energy the thrust force and extracted power can be written as follows due to loss of wind speed and pressure difference as seen in figure 3.7:

$$T = \frac{1}{2}\rho A_D C_T U_\infty^2 \quad (3.28)$$

$$P = T U_D = \frac{1}{2}\rho A_D C_P U_\infty^3 \quad (3.29)$$

Here U_D represents the difference in wind speed, while C_T and C_P are the thrust coefficient and the power coefficient, respectively. These coefficients are related to the unknown induction coefficient a through the following relationship:

$$C_T = 4a(1 - a) \quad (3.30)$$

$$C_P = 4a(1 - a)^2 \quad (3.31)$$

To maximize power extraction, the induction coefficient a should be optimized. The theoretical maximum power coefficient is determined by setting the derivative of C_P with respect to the axial induction factor a to zero. This results in a theoretical maximum power coefficient of $\frac{16}{27}$, which is known as the Lanchester-Betz limit. Correspondingly, the thrust coefficient at this maximum power coefficient is $\frac{8}{9}$.

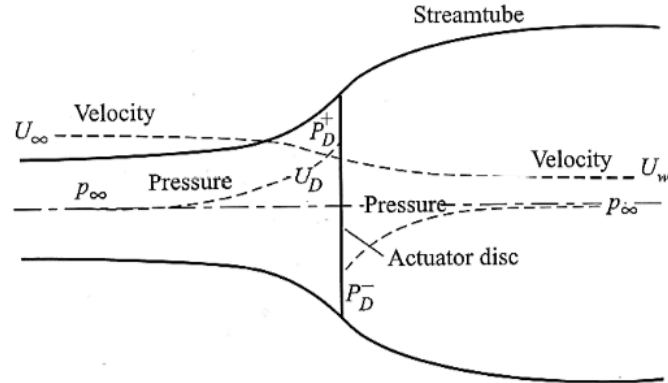


Figure 3.7: Wind speed and pressure on an actuator disc (TU Delft, 2023) [9]

In reality the power and thrust are less due to wake losses and wake rotation so the Lanchester Betz limit will not be reached. By using the Blade Element Momentum (BEM) method more precise values can be calculated for the thrust and power. It combines the momentum-theory with wake rotation and the airfoil characteristics of the wind turbine blades. BEM evaluates smaller pieces of the entire blade and includes forces induced by the velocity of the rotor disk. It then integrates the forces over the entire blade to find the total force. More on this can be found in 'Aerodynamics of wind turbines' by M. Hansen [23].

As mentioned, there is also a drag force acting on the tower of the wind turbine. This can be evaluated by using the drag component of the Morison equation given in section 3.2.4. The velocity here would be the wind velocity, due to the blades passing in front of the tower a mean wind velocity should be estimated. The contribution of the wind drag force will be especially important for cases above the cut-out speed, in this situation the rotor will not be rotating due to the blades being pitched into the wind.

All these forces exerted on the wind turbine are included on the right hand side of the EOM.

3.4. Mooring equations

Offshore structures are subjected to extreme environmental loads such as wind, waves, and currents. Bottom-fixed structures utilize their substructure to stay in place, while floating structures rely on mooring systems to prevent drifting. Mooring not only anchors the structure but also plays an additional role in limiting other motions, primarily heave, pitch, and roll. It acts as a stiffness constraint, as mentioned previously. There are two main types of mooring designs: **catenary mooring** and **taut mooring**. Catenary mooring relies on the weight of the suspended mooring chain to provide both vertical and horizontal restoring forces. The mooring system is designed to ensure that there is no uplift at the anchor point. In contrast, taut mooring relies on both the weight of the mooring chain and the resistance to uplift force at the anchor point to keep the floating structure in place. It's important to note that a taut mooring design is not the same as a TLP. A TLP is held in position due to the tension acting on the buoyancy of the structure.

The design of a mooring system is dependent on the environment and the operations. For certain operations only temporary mooring is needed (e.g. the anchoring of a ship), in these cases only one or in case of a large vessel a few small mooring lines are used. For operations that are of longer duration

(e.g. floating offshore wind turbine) a sturdier design is used. This design will be a spread design around the system to prevent drifting. The material used for the mooring line is also an important part of the design, section 2.3 explains more on this topic.

In this report, two definitions will be used for mooring lines to improve clarity. **Mooring lines** will refer to the lines between the seabed and the FOWT. **Connection lines** will refer to the lines between two FOWTs.

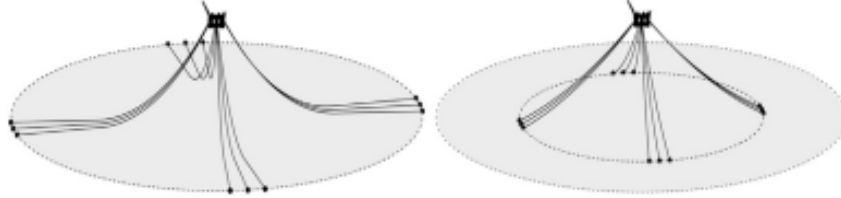


Figure 3.8: Types of mooring designs (Ma et al., 2019)[31]

3.4.1. Catenary mooring equations

For simplicity inelastic mooring is assumed and will be explained in this section, this is also called the static solution. The formulas for elastic mooring will be provided in appendix A. Mooring lines follow a catenary shape before touching down on the seabed as long as it has uniform mass and is solely acted on by gravity [5]. The catenary function is a hyperbolic cosine function, here a is the constant defining the shape of the hyperbolic cosine function:

$$y = a \cosh(x/a) \quad (3.32)$$

Assuming inelasticity ($EA = \infty$), there is no stretching of the mooring line. From Figure 3.9, it is possible to derive equations 3.33 and 3.34 for the tangential and normal directions of each element of the mooring line [32]. Here, P represents the weight of the line, and F is the hydrodynamic force, which is neglected in this section because its effect is small enough that the shape of the mooring line is primarily a function of the top-end location. T denotes the tension in the cable.

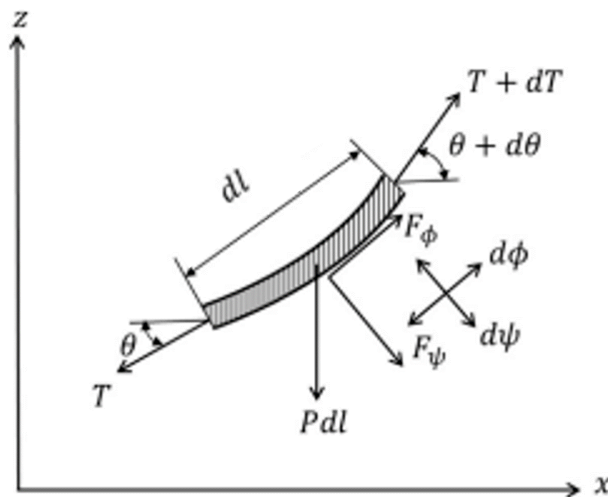


Figure 3.9: Forces on an element of a mooring line (Ma et al., 2019)[32]

$$dT - P \sin \theta dl = 0 \quad (3.33)$$

$$T d\theta - P \cos \theta dl = 0 \quad (3.34)$$

Knowing the boundary conditions of the locations at the seabed and the location of the top end it is possible to rewrite the catenary equation (3.32) with these two equations as a function for suspended cable length and height at a certain location.

$$l(x) = \frac{T_0}{P} \sinh\left(\frac{P}{T_0} x\right) \quad (3.35)$$

$$h(x) = \frac{T_0}{P} \cosh\left(\frac{P}{T_0} x\right) - \frac{T_0}{P} \quad (3.36)$$

Figure 3.10 shows the different parameters according to these formulas. When given a horizontal pretension T_0 it is possible to write the profile of the suspended section as equation 3.37 and the tension along this section as equation 3.38.

$$l = \sqrt{h(h + 2\frac{T_0}{P})} \quad (3.37)$$

$$T(l) = T_0 + P h \quad (3.38)$$

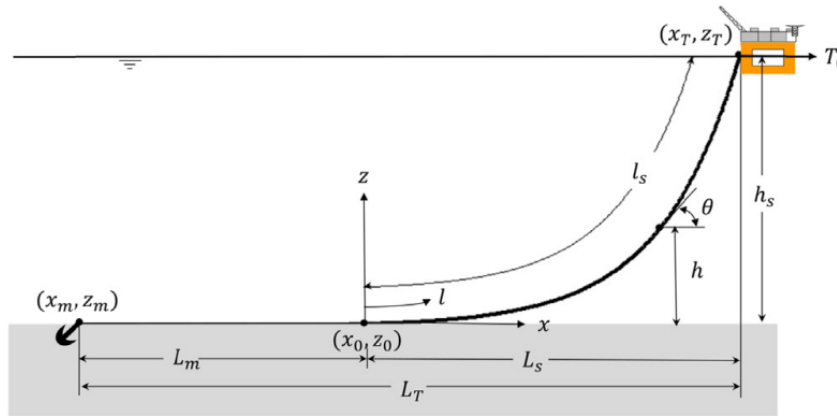


Figure 3.10: Geometry of a catenary line (Ma et al., 2019)[32]

3.4.2. Taut mooring equations

For taut mooring systems, different equations are applicable, but the fundamental concept remains unchanged. When the mooring chain is fully lifted from the seabed, the anchor must be capable of withstanding an upward vertical force. It is important to note that not all types of anchors are suitable for this application; further details on this topic are provided in section 2.4. The line configuration for a taut leg system can be determined using the equations below [17].

$$x = \frac{T_H}{w} \log\left(\frac{\sqrt{T_H^2 + T_Z^2} + T_Z}{T_H}\right) + \frac{T_H}{EA} l_s \quad (3.39)$$

$$l_s = \frac{T_Z}{w} \quad (3.40)$$

$$T_H = \frac{(T_Z^2 - (wh - \frac{1}{2} \frac{w^2}{EA} l_s^2))^2}{2(wh - \frac{1}{2} \frac{w^2}{EA} l_s^2)} \quad (3.41)$$

By using these equations in an iterative process and starting with an initial guess for the vertical tension T_Z the taut mooring design can be defined. The mooring system works as a stiffness defined by the K matrix in the EOM. There is a geometrical stiffness that is material dependent and a tensional stiffness

that is the same as the elastic stiffness in the catenary mooring. These are respectively given by the equations:

$$K_g = \frac{x_0^2 K_{33}}{h^2} \quad (3.42)$$

$$K_l = \frac{EA}{l_0} \quad (3.43)$$

Here K_{33} is the buoyant heave stiffness given in equation 3.6, x_0 is the anchor radius. As the structure is displaced in the surge direction due to environmental loading, the horizontal force in the mooring line increases. Consequently, due to the geometry of the mooring system, the vertical force also increases, exerting a downward pull on the structure. The surge stiffness for a single taut leg mooring line is defined by equation 3.44. To determine the surge stiffness of the entire system, this value is multiplied by the squared cosine of the angle between the mooring lines.

$$K_{taut} = \frac{1}{\frac{h^2}{x_0^2 K_{33}} + \frac{l_0}{EA}} \quad (3.44)$$

4

Method and model

In this chapter the methodology and model are explained. MBD, dynamic modeling of lines and an implicit integration scheme are explained briefly. The base case model that is used is described. Furthermore the modifications that were made to transform it into a daisy-chained configuration with added mass and damping are explained. Finally the load cases will be listed.

4.1. Methodology

The problem was modeled using OrcaFlex software, which is a MBD analysis tool used in the offshore industry for analysis and design purposes [41]. In addition to MBD, OrcaFlex employs a finite element method (FEM) to solve the mooring equations and uses an implicit integration scheme to solve the EOMs. This section briefly explains how these different techniques function.

4.1.1. Multibody dynamics

MBD is a field of mechanics that deals with the modeling, analysis, and simulation of systems consisting of interconnected rigid or flexible bodies. These bodies can move relative to each other and are subjected to various forces and constraints. The primary goal of MBD is to predict the motion and behavior of these complex mechanical systems under the influence of internal and external forces. In MBD, bodies are typically classified as rigid or flexible. Rigid bodies do not deform under load, simplifying the analysis, while flexible bodies can deform, providing a more accurate representation of real-world systems. There are two types of analyses: kinematic and dynamic. Kinematic analysis involves studying the motion of bodies without considering the forces causing the motion. Dynamic analysis, on the other hand, incorporates forces and torques to determine the resultant motion. In multibody systems such as the case of daisy-chained mooring the number of DOFs needs to be determined, in this case the DOFs are the six mentioned in section 3.1. An example of a single DOF system could be a weight hanging on a spring. The behavior of multibody systems is governed by EOMs derived from Newton's laws, Lagrange's equations, or other principles. These equations form the foundation for analyzing the dynamic response of the system.

4.1.2. Dynamic modeling of the mooring lines

OrcaFlex has a fully dynamic approach for the mooring. This is done with a FEM where the mooring lines are represented as lumped masses. The lines are discretized in nodes over the length of the cable with evenly-sized line segments. The model calculates all internal and external forces on these different nodes. The dynamic approach includes damping and inertia in each node. Matthew Hall and Andrew Goupee elaborate further on this method in their research in mooring line modelling for semi-submersibles [22]. Figure 4.1 shows how the mooring lines are represented.

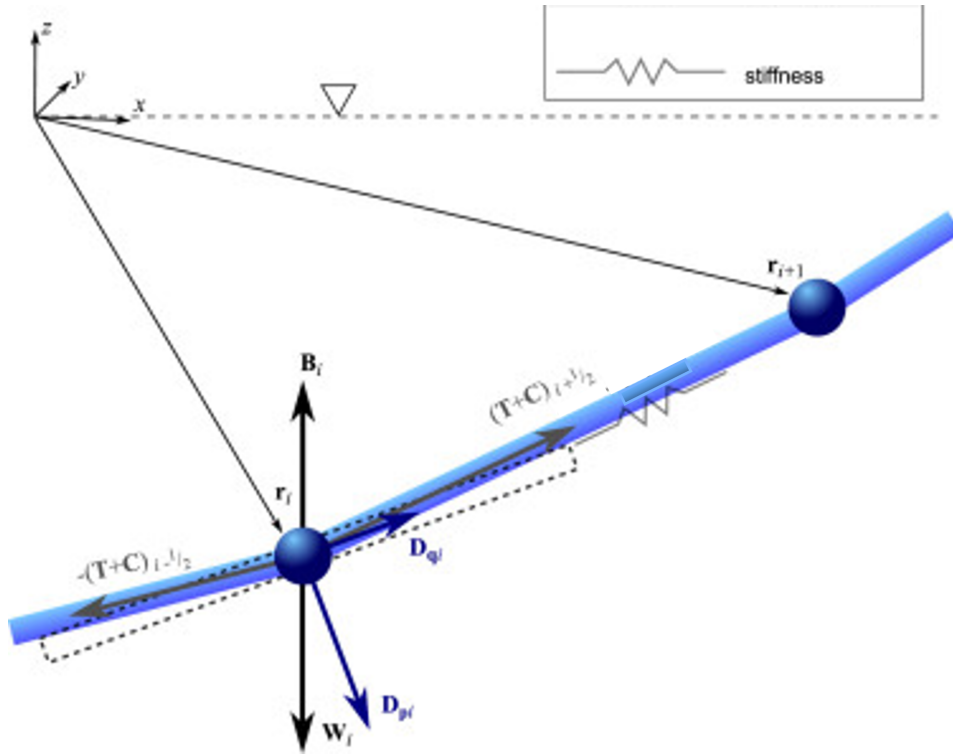


Figure 4.1: Lumped mass model, (M. Hall, 2015)[22]

4.1.3. Implicit integration scheme

An implicit integration scheme was used to solve the EOMs. This scheme finds a solution by solving equations for both the current state and the future state. The generalized- α integration scheme, as described by Chung and Hulbert [7], is employed. Forces, moments, damping, mass, and other factors are calculated in the same way as in an explicit scheme. However, the system's EOM is solved at the end of each time step. The position, velocity, and acceleration for the later time step are unknown and are solved iteratively. While this iterative process makes an implicit solver initially slower than an explicit solver, the implicit scheme is typically stable for much longer time steps, making it more efficient overall. The EOM being solved is presented in section 3, and the formulas for acceleration, velocity, and displacement for the generalized- α method are as follows, where p , v , and a represent displacement, velocity, and acceleration, respectively:

$$p_{n+1} = p_n + \Delta t v_n + \Delta t^2 \left(\left(\frac{1}{2} - \beta \right) a_n + \beta a_{n+1} \right) \quad (4.1)$$

$$v_{n+1} = v_n + \Delta t \left((1 - \gamma) a_n + \gamma a_{n+1} \right) \quad (4.2)$$

$$p_0 \approx p \quad (4.3)$$

$$v_0 \approx v \quad (4.4)$$

$$a_0 = M^{-1} (F(0) - Bv - Kp) \quad (4.5)$$

where:

$$p_{n+1-\alpha_f} = (1 - \alpha_f) p_{n+1} + \alpha_f p_n \quad (4.6)$$

$$v_{n+1-\alpha_f} = (1 - \alpha_f) v_{n+1} + \alpha_f v_n \quad (4.7)$$

$$a_{n+1-\alpha_m} = (1 - \alpha_m) a_{n+1} + \alpha_m a_n \quad (4.8)$$

$$t_{n+1-\alpha_f} = (1 - \alpha_f) t_{n+1} + \alpha_f t_n \quad (4.9)$$

Here n is the number of the time step and Δt the time step size. It is crucial to determine relationships between the algorithmic parameters α_f , α_m , β and γ . This is determined by the software. The tolerance for the implicit solver in the model is set to $25 * 10^{-6}$

4.1.4. Overview of the model

Figure 4.2 shows an overview of the MBD model which is modeled using OrcaFlex software. Section 4.1.2 is used in the box with line properties and mooring forces and the implicit solver explained in section 4.1.3 can be seen in the blue boxes.

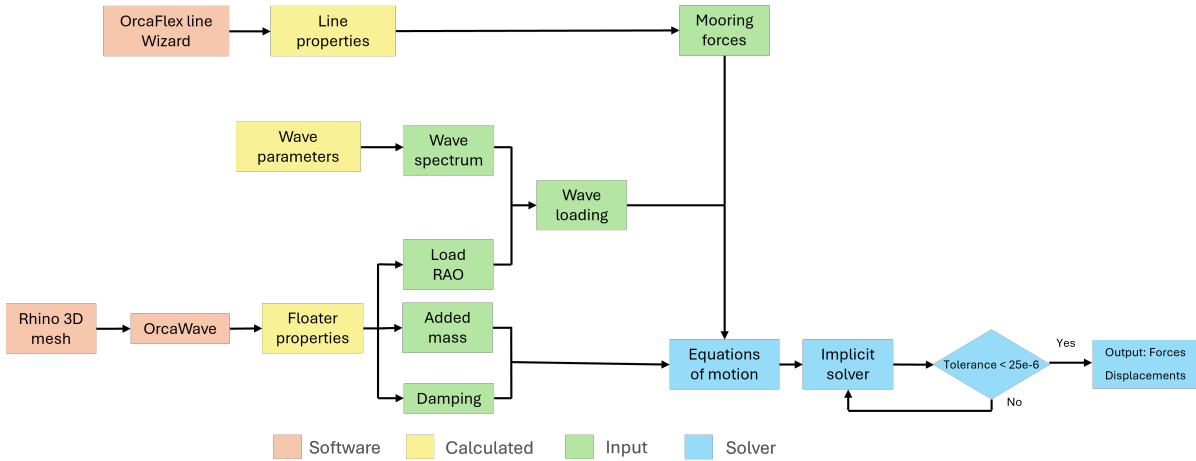


Figure 4.2: Overview of the multibody dynamic model

4.2. Model

This section explains how the model is built and which different design choices are implemented.

4.2.1. Base case

A publicly available base case model was used, that was provided by Orcina. In this report the base case will often be referred to as a single FOWT. It is a model of the National Renewable Energy Laboratory (NREL) 5 MW baseline turbine which is mounted on the Offshore Code Comparison Collaboration (OC3) Hywind spar, from here on this spar and turbine combination will be known as the 5 MW turbine [39][43]. This floating turbine can be seen in figure 4.3. The properties of the turbine tower or floater will remain unchanged throughout this research, as their alteration falls outside the scope of this study. These main properties will also remain the same for the daisy-chained configuration. All specific properties can be found in appendix B. There are also other models that could have been chosen, like the 15 MW turbine developed by the IEA as part of Wind Task 37 mounted on the UMaine VoltturnUS-S [40]. The reason the 5 MW turbine was chosen is that the scope of the research focuses on the mooring configuration and not the type of floater or the amount of power that can be produced. The 5 MW turbine is a lighter model which made it possible to run more simulations.

Inertia effects wind turbine

The wind turbine isn't simply modelled by a force on top of the tower. This thrust force is evidently included in the model but besides that the inertia effects of the blades are also taken into account. This includes gyroscopic stabilisation and rotor inertia. The tower itself is modelled as a stiff pipe allowing for bending and torsion. The aerodynamic loads on the blades are modeled using the BEM including axial and tangential induction.

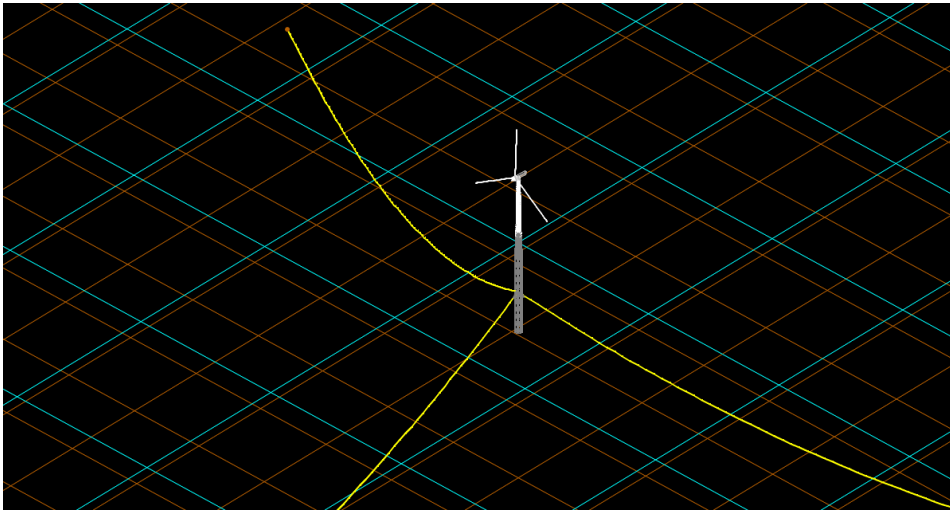


Figure 4.3: Base case, 5MW spar floater wind turbine

Added mass and damping

In the provided model, added mass and damping wasn't added to the floater. To be able to implement this a diffraction analysis had to be done. Rhinoceros 3D was used to make a 3D mesh of the floater. This is a commercial computer aided design software package developed by Robert McNeel & Associates [35]. This software meshes the structure to be able to use it as input in OrcaWave. A figure of this mesh is given in appendix B.3. The tower, blades and nacelle of the turbine aren't modeled because only the submerged part of the structure is relevant for a diffraction analysis. OrcaWave uses linear potential theory to calculate the loading and responses of a structure to waves. It outputs the load RAOs, added mass matrices and damping matrices. These matrices for each different wave period used in the model are given in appendix C. For each wave period there is a different added mass and damping matrix. The added mass and the damping matrix respectively represent the $A(\omega)$ and the $B(\omega)$ in the EOM. When looking at figure 3.5 the spar floater falls in regime *III* and *V* depending on the wave period. The added mass and the damping are thus not negligible. In addition to the damping term proportional to the free surface provided by OrcaWave, there is also a component of viscous damping. A viscous damping matrix was provided by Jonkman who in turn received it from Statoil that performed experiments[28]. These terms were needed to match a free decay test. Additional linear damping of 100,000 N/(m/s) was needed for surge and sway motions, 130,000 N/(m/s) was needed for heave motions, and 13,000,000 Nm/(rad/s) was needed for yaw motions. These are values that match this specific situation and conditions for the free decay test. Viscous damping in reality is a non-linear term due to the velocity of the fluid flowing past being squared. OrcaFlex however doesn't incorporate adaptable damping matrices in a single simulation for buoy types. The spar floater is modelled as a buoy type in the simulations. This means that the damping isn't always precise but should be a realistic value instead of a zero-value which would have a much larger influence on the results. For that reason this matrix is simply added on top of the free surface damping matrix. This isn't completely correct but it gives an approximation.

Mooring

The mooring lines provide damping to the system through linear damping terms, with drag coefficients for both normal and axial directions. The normal drag accounts for the resistance of the line moving through water, while the axial drag represents skin friction along the line's surface. For a smooth line surface, the axial drag coefficient is set to 0.008. No internal friction damping is modeled within the line, though Rayleigh damping could be used to account for this. However, it was excluded from the model because the amount of damping could be neglected. Friction with the seabed is accounted for with a coefficient of 0.5. The lines also have a normal added mass coefficient of 1.0.

The mooring was modified in the model. The original base case model employed a 'crowfoot' connection, using a 3-DOF delta plate to split the mooring line into two delta lines, with half of the mass located

near the spar floater, as shown in Figure 4.4a. The model was modified to remove the two delta-lines. The reason these were removed is to improve the calculation times, for easier sanity checks and because the software aborts the calculations when the lines are too slack and thus can't find a solution. The latter happens often with delta lines. The crowfoot however has the function to create additional yaw stiffness. It isn't possible to simply connect the single mooring line to the spar floater, this will reduce the yaw stiffness drastically since it will take a larger rotational distance to create the same restoring moment. To compensate for this the mooring line will be attached a certain distance from the center of the spar floater. Simulations were run where the distance from the center was gradually increased and the yaw movement was compared to the crowfoot simulation. Eventually a distance of 5 meter from the floater surface and 9.7 meter from the floater center was determined. The horizontal distance from the floater to the anchor is 853.87 meter. The crowfoot mooring configuration and the new mooring configuration can be seen in figure 4.4b. A mesh size of ten meters was chosen for the mooring lines, section 5.3 shows that this distance gives accurate results.

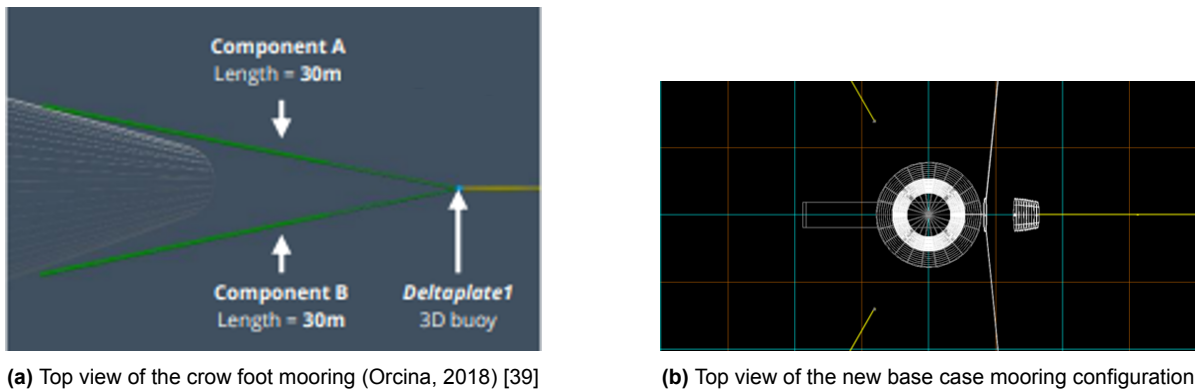


Figure 4.4: Base case mooring configuration

The mooring lines have added mass and drag coefficients, all mooring parameters that will remain constant during the simulations for the mooring lines are given in table 4.1 [43]. The only parameter of the mooring lines that will be modified is the length. This has an effect on the horizontal pretension.

Table 4.1: Mooring line parameters

Coefficient	Value	Unit
C_d	1.2	[-]
C_a	1	[-]
Axial stiffness	384,200	[kN]
Torsional stiffness	80	[kN.m ²]
Poisson ratio	0.5	[-]

4.2.2. Daisy-chained model

Two different daisy-chained models were created. A triangular and a hexagonal model. The hexagonal model is the most similar to the base case due to the two connection lines and the mooring lines creating equal angles of 120 degrees. The triangular model has an angle of 60 degrees between the two connection lines and two angles of 150 degrees between the mooring line and a connection line. This difference in angles is another reason why the crowfoot mooring is altered as explained in section 4.2.1. With an angle of 60 degrees the crowfoot mooring would cause clashing between the delta lines if the angle of the crowfoot wouldn't be reduced. If the crowfoot angle would be reduced the yaw stiffness effects of the crowfoot would be lost. A triangular configuration was chosen for simplicity and a hexagonal configuration was chosen due to the physical strength of hexagonal systems as explained in 'Hexagons are the bestagons'[18].

The hexagonal and triangular configurations still have the same floater and wind turbine properties as

the base case. The distance between the wind turbines is set to seven times the diameter of the rotor. This distance is conventionally used in existing wind farms to limit wake losses [36]. This distance is 882 meter, the horizontal distance from the floater to the anchor is the same as in the base case model. Figure 4.5 shows both configurations.

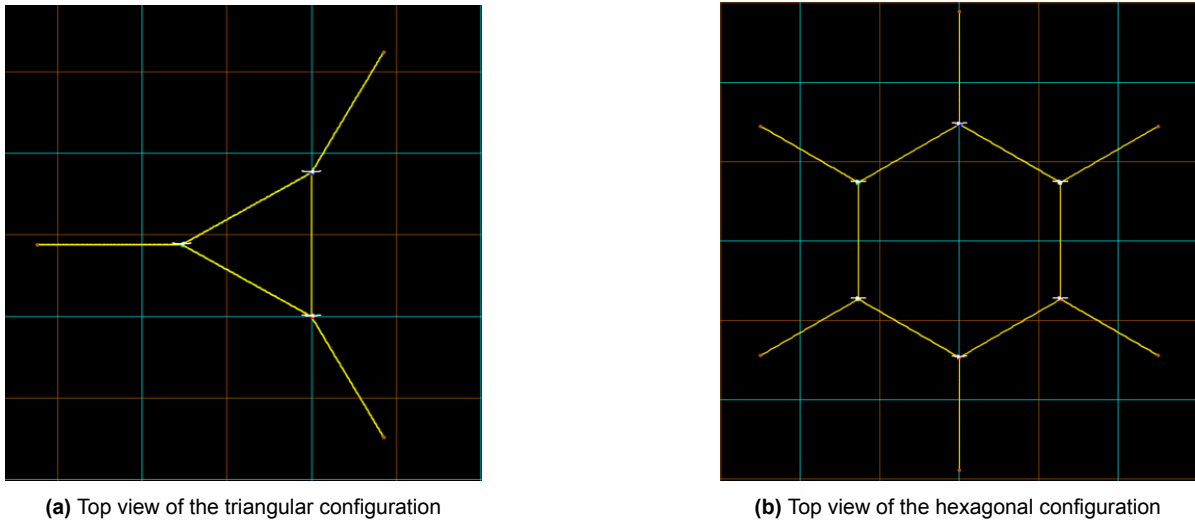


Figure 4.5: Daisy-chained configurations

The different spar floaters in the model have each been given a different color to make it easier for identification in the results chapter. Figure 4.6 shows this color coding for the triangular and hexagonal configuration. A wind rose is shown as well to show which direction is meant when speaking of wind or wave direction.

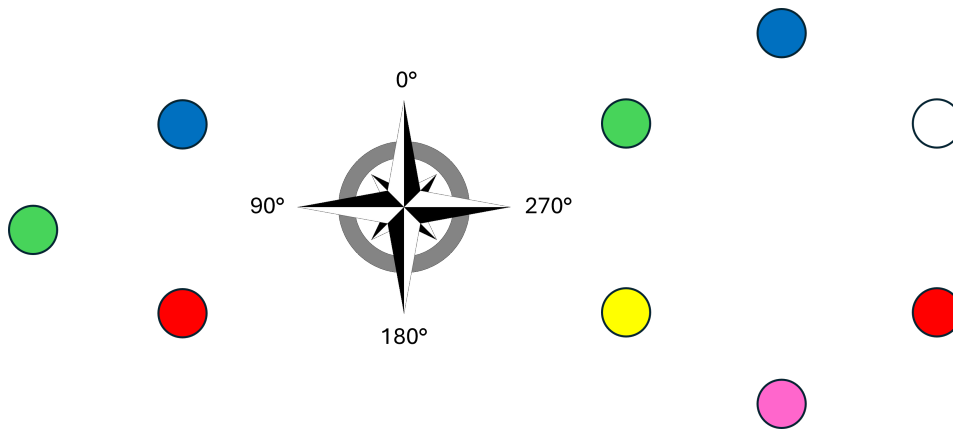


Figure 4.6: Color coding of the different spar floaters with wind direction

4.2.3. Load cases

A set of load cases is simulated to be able to compare results. It is important to run similar simulations where only one parameter differs to be able to make well-founded conclusions. The different parameters that will be altered are the environmental conditions (EC) or sea-states (this includes wave height, period and wind speed), the direction of the EC, the mooring horizontal pretension and the mooring configuration. Water depth is kept constant at 320m.

The amount of directions of the environmental loading is dependent on the shape of the configuration. For the single wind turbine and the triangular configuration three directions are needed to be able to include all 360 degrees in steps of 30 degrees. For the hexagonal configuration only two directions are needed due to its symmetrical properties.

The sea-states are based on combining wave heights and wind speeds from the Beaufort scale [2]. Three different sea-states are determined one with a strong breeze, one with a strong gale but where the wind-speed is below the cut-off speed of the wind turbine and a storm sea-state where the wind speed is higher than the cut-out speed of the wind turbine. The peak frequency of the waves was determined by following formula with V being the wind speed [49].

$$f_0 = \frac{0.87g}{2\pi V} \quad (4.10)$$

The significant wave height and peak period were used to produce a JONSWAP spectrum with $\gamma = 3.3$. The wind speed is kept constant. The following sea-states are used in the load cases.

Table 4.2: Sea-states

Sea-state	H_s [m]	T_p [s]	V_s [m/s]
1	5	11	15
2	8	16	22
3	11	20	27

For the horizontal pretension the length of the mooring lines is altered to be able to compare the base case with the triangular configuration. The weight of the lines remained constant at 77.71 kilograms per meter. The different pretensions and corresponding mooring and connection line lengths for the base case can be found in table 4.3 and for the triangular configuration in table 4.4. For the hexagonal configuration the pretension wasn't altered.

Table 4.3: Horizontal pretension for the base case

Horizontal pretension	T_H [kN]	L_M [m]
1	993	947.5
2	2333	931.9
3	600	961.6

Table 4.4: Horizontal pretension for the triangular configuration

Horizontal pretension	T_H [kN]	L_M [m]	L_C [m]
1	993	905	880
2	2333	890	850
3	600	940	900

The simulations have a ramp-up stage of 240 seconds, this is done so that the waves and wind forces are applied gradually. This makes the simulation run smoother and prevents the implicit integration scheme to require very fine time steps. After the ramp-up stage the simulation was run for 2000 seconds for the hexagonal configuration and 2400 seconds for the triangular configuration and base case to make sure that enough data was collected. A time step of 0.25 seconds is used for the daisy-chained configurations and a time step of 0.1 is used for the base case simulations. Section 5.3 shows that this gives a good enough accuracy without drastically increasing computation time. All load case combinations can be found in appendix D. The triangular load cases are labeled as LC and the hexagonal load cases are labeled as HLC, these abbreviations will be used throughout this report. Due to the wind turbine activating at a certain wind speed, a sudden force is applied to the system. This causes the turbine to roll until it stabilizes at its dynamic equilibrium position. This transient data is disregarded when analyzing the data and calculating mean inclinations and main loads.

5

Validation of the model

Before results can be generated and interpreted the model needs to be validated. OrcaFlex is an industry wide used standard software. This makes it difficult to independently validate it. It is however possible to test if the model is accurate enough to simulate real-life systems. This can be done by comparing it to real life data and see if it performs similar. It is also possible to do simple hand calculations to see if the results are likely to occur in real-life. Besides that there is a document provided with the Orcina 5 MW wind turbine model to validate it [43]. This document however only compares the model to other MBD software such as FAST and ADAMS. This doesn't independently validate it.

5.1. Hywind Scotland wind farm

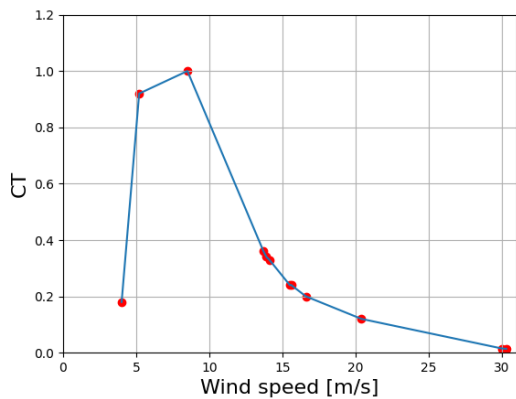
ORE Catapult provided real-life data from the Hywind Scotland wind farm [38]. ORE Catapult is an United Kingdom based research center for offshore renewable energy. The Hywind Scotland wind farm is the worlds first floating wind farm built in 2017. It has five turbines each producing 6 MW. The floater is a spar design with a height of 85 meter. The turbine type is a SWT-6.0-154 with a rotor diameter of 154 meter [27]. The different parameters for which data is provided are:

- Latitude and longitude drift off
- Delta line loads
- Nacelle pitch and roll
- Tower pitch, roll and yaw
- Yaw direction

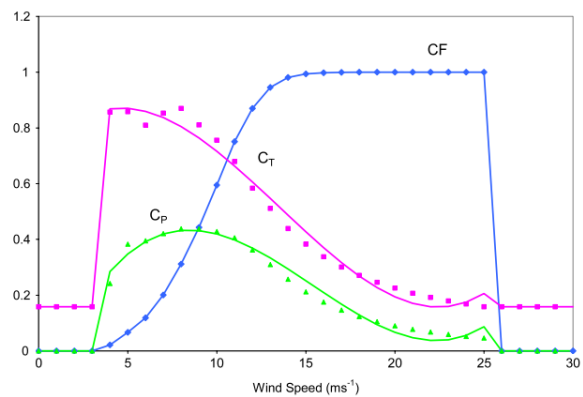
The data consists of eleven cases each for a time interval of thirty minutes. All eleven cases take place in 2018, a year after the wind farm was installed. Two of these cases have an idle turbine due to high wind speeds. Together with these datasets a description file is supplied which details the dimensions of the floating wind turbine and the environmental conditions per case which can be found in table E.1 in appendix E. It has the significant wave height, peak period, wave direction, current velocity, current direction, wind speed and the wind direction. With this description file it is possible to build a MBD model and compare the results with the accompanying data. This way it is possible to validate that MBD is a correct way to model FOWTs. It is important to note that this is not the same type of floater or turbine that is used in the model for the daisy-chained configurations. This validates the software and method by seeing if the results are similar, not the model itself. One thing to note is that there is no detailed description of the turbine properties, for this reason the 5MW turbine was used for the simulations.

After running simulations for the first nine cases where the turbine is not idle the results show a large inclination for the FOWTs. The average inclinations for the thirty minute intervals are between 20 and 40 degrees with one outlier of 10 degrees. This deviated significantly from the provided data where the averages are between 3 and 5.3 degrees with the outlier being 1.3 degrees. Clearly something is wrong

with the model. The provided data description file gives a height difference between the COB and the COG of 7.99 meters with the COG a distance of 27.57 meters from the base of the floater. Considering that the concept of a spar floater relies on a significant distance between the COB and the COG to generate a restoring moment when the structure is slightly overturned, it is assumed that the provided distance between COB and COG is incorrect. The COB is near the halfway point of the submerged part of the structure which indicates that this is likely correct, the given COG is thus misplaced. It is possible to calculate new COG's using the provided inclination data, equation 3.28 and the sum of moments around the COB. It is assumed that the system is quasi-static at the average inclination to be able to equate the sum of moments to zero. The loads of the mooring lines are neglected, the mooring lines have opposing moments so the resulting moment of the mooring will be low. Equation 3.28 requires a thrust coefficient, C_T . To be able to find the correct value one of two things is required. A thrust coefficient graph which supplies a value for C_T for each wind speed or the the induction coefficient a . The first is not provided with the data description and the second can't be calculated because you both need the wind speed in front of and behind the rotor and only the general wind speed is supplied. It is however possible to estimate the thrust coefficient for the different wind speeds and line up the values so that it fits the general shape of a thrust coefficient curve. A wind turbine that has a larger inclination will have a larger thrust force working on it, when ordering the inclinations of the different cases and adjusting the thrust coefficients the following values are found for the different cases as can be seen in figure 5.1a. Figure 5.1b shows another thrust curve from a 2 MW wind turbine [1]. Using these thrust coefficients it is possible to find thrust forces for each case. When placing these forces in ascending order they match the ascending order of the average inclination for each case. The shape in figure 5.1a matches the shape of the pink dots in figure 5.1b showing that the estimated thrust coefficients are in the correct order.



(a) Estimated thrust coefficient per wind speed for all eleven cases



(b) Thrust coefficient curve from a 2.0 MW wind turbine (Adams & Keith, 2013) [1]

Using all this information new COGs per case are calculated and given in table 5.1. This distance is from the base of the floater. The location of the COB remains constant. It is clear that all new COGs are far below the value provided in the data description file.

Table 5.1: Calculated COG

Case	1	2	3	4	5	6	7	8	9	10	11
COG [m]	23.82	20.09	18.26	21.78	21.74	22.25	23.52	21.43	22.12	19.98	20.34

With the new COG locations, simulations are conducted for each case using their respective newly determined COGs. Since the COG cannot occupy multiple locations simultaneously, the results will help identify the most accurate COG. When looking at figure 5.2 it is seen that for case 3 the simulation of the newly calculated COG lines up perfectly with the real-life data, the red dot falls behind the green dot just above the blue dot. This difference in the average of inclination is 0.05 degrees. Simulations are then also run for a COG of 18.26 meter and for the average of all newly calculated COGs. This

average is 21.39 meter. When looking at the results it is seen that the COG of 18.26 gives a conservative inclination. The calculated COG mostly gives a too large inclination, this is probably due to the lack of the mooring lines in the sum of the moments. When the structure is tilted the working line of the force in the downwind mooring line will become more perpendicular to the center line of the spar floater and vice versa for the upwind mooring line. This creates a overturning moment that has been neglected.

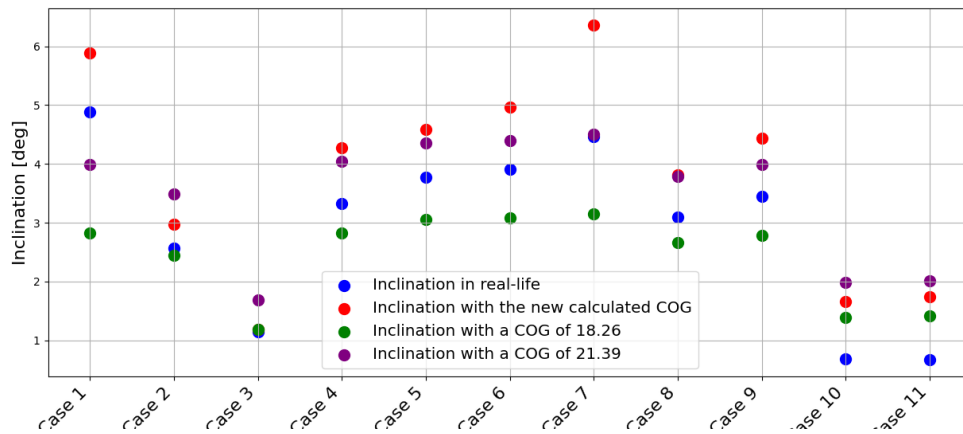


Figure 5.2: Comparison inclination for real-life and simulations

When looking at the root mean square of the average inclinations the COG of 21.39 meter performs the best with a value of 0.65 compared to a value of 0.95 for the COG of 18.26 meter and a value of 0.99 for all the separately calculated COGs. Figure 5.3 shows the boxplots of the real-life data and the simulations for the average COG. The simulated boxplots have a smaller range, this is due to the wind speed being constant in the simulations, in real-life this is obviously not the case and the inclination of the wind turbines will vary more.

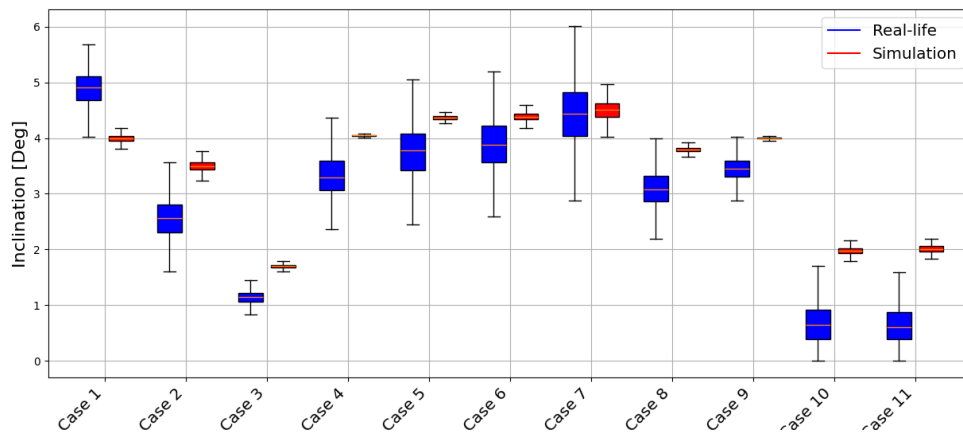


Figure 5.3: Boxplots for the real-life data and the average COG simulations

For most cases the numerical results with the COG of 21.39 meter line up well with the real-life data. Only in the case of the idle wind turbine it doesn't match as well and the aforementioned COG even performs the worst. A reason for this could be that the diameter of the real-life tower isn't given, so the element catching the most wind in these cases causing the inclination isn't modeled properly.

Loads in the delta lines

The loads in the delta lines can be compared between the real-life data and the simulations to see how the model performs. The data of case 1, 3, 7 and 11 is chosen because these are two well performing cases, one less performing case and an idle case. The simulations with the average COG of 21.39 meters is chosen to compare to. The first thing that is noticeable is the fluctuation in the data. Just as in the inclination the real-life data has a larger range than the simulation data. This is again due to the wind in the simulations being constant. It is however not as large of a difference as the inclination data. The displacement of the wind turbine has the largest influence on the loads in the mooring lines. The wind causes a part of this displacement but the waves and the current have a relative larger influence on this displacement.

For case 1 the loads between the data and the simulations are for most lines pretty similar being less than a 10 percent difference as can be seen in figure 5.4. However for lines that have a lower load or in other words are more slack there is a larger difference as can be seen in figure 5.5.

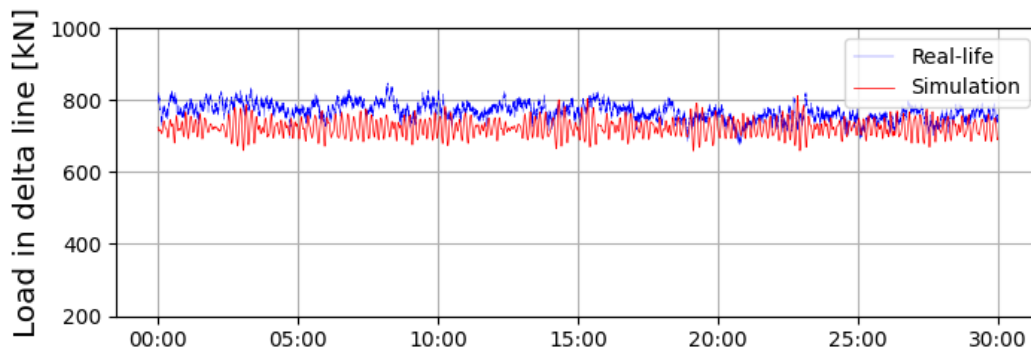


Figure 5.4: Load in mooring line 2, delta line 1 for case 1

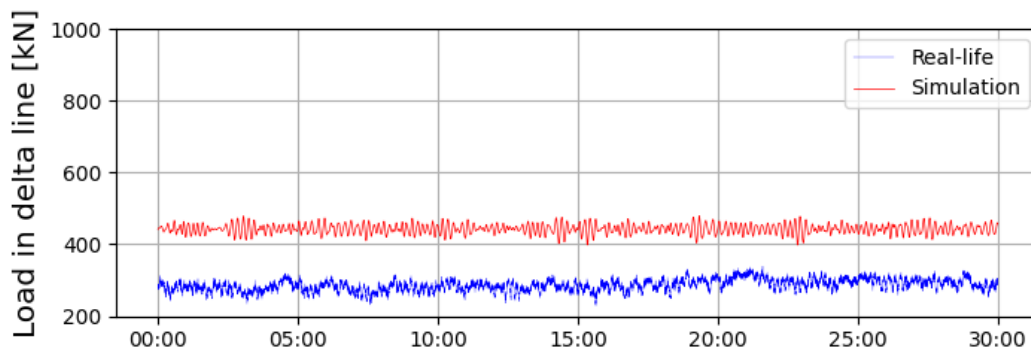


Figure 5.5: Load in mooring line 3, delta line 2 for case 1

Case 1 has already been shown to be less precise compared to real-life data. In contrast, Case 7 performed better, as evidenced by the loads in the delta lines, illustrated in Figure 5.6. The graphs in Appendix E indicate that the model is capable of simulating forces to a certain degree, allowing it to approximate the general load in a mooring or delta line. However, it lacks the precision needed to accurately determine the exact load location at any given moment.

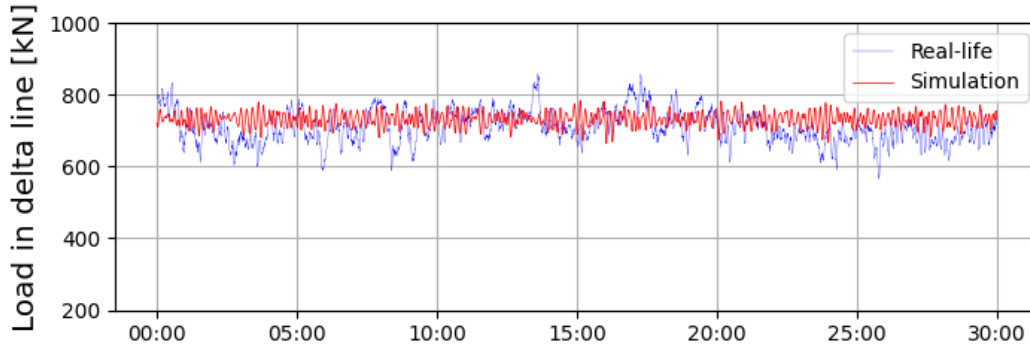


Figure 5.6: Load in mooring line 1, delta line 1 for case 7

5.2. Natural frequency of lines

When performing a modal analysis, the software provides all modes and natural frequencies of the system, including all loose elements. This is achieved by considering the lines as an undamped system with no force working on it, which simplifies the EOM to equation 5.1. By solving for a solution of the form $x = A \sin(\omega t)$, we derive the equation for the natural period, as given in equation 5.2. This analysis applies to a simple one-DOF system; however, when multiple DOFs are present, the analysis becomes more complex, as discussed by Kollar and Tarjan [30].

$$mx''(t) = -kx(t) \quad (5.1)$$

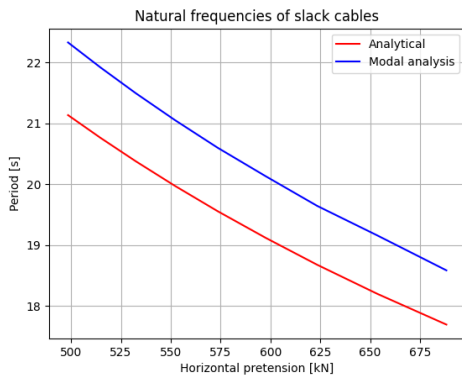
$$T = 2\pi \sqrt{\frac{m}{k}} \quad (5.2)$$

The low frequency modes are movements of the wind turbines in their different DOFs. The higher frequency modes are natural frequencies of the mooring and connection lines. It is difficult to perform hand calculations to find the natural frequencies for the entire tower and the connected system. It is however possible to perform hand calculations for singled out mooring and connection lines. A formula is presented to find the natural frequencies for horizontal slack cables by O.M. Griffin and F. Rosenthal [19]. This formula can be found below.

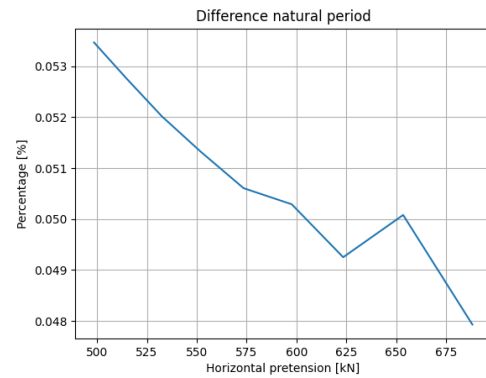
$$f_n = \frac{n}{2l} \sqrt{\frac{T_H}{m}} \quad (5.3)$$

In this formula, n is the number of the natural frequency or mode for the cable, l is the horizontal distance between the two ends. T_H is the horizontal tension at the end of the cable, and m is the mass per unit length of the cable. The issue with a floating system is that the length of the horizontal distance and the horizontal tension are dependent of each other. If you make the connection line between two wind turbines longer the increased mass will pull the two turbines towards each other and make the line hang more slack. This will increase the total tension in the line. However, it will reduce the horizontal tension. This makes it difficult to compare natural frequencies with different pretensions or distances with each other because the other parameter will change as well. It is however possible to present a few cases and compare the analytical solution to the numerical solution from the modal analysis.

To start off the triangular configuration was used to calculate the natural frequencies of the connection lines. A number of lengths ranging from 860 meter to 900 meter in steps of 5 meter was taken. A static analysis was performed to be able to calculate the distance l and find the horizontal pretension H . With the modal analysis the first natural frequencies were determined and plotted against the analytical method presented above.



(a) Analytical natural frequencies compared to modal analysis



(b) Difference between the analytical method and the modal analysis

There is a difference in the results between the model analysis and the analytical method. This is most likely due to the analytical method not accounting for extension of the cable due to its self-weight.

5.3. Convergence study

A convergence study was done to evaluate the accuracy and stability of a simulation. Besides that it is useful to determine if the chosen mesh size and time step size is accurate enough without drastically increasing the computation time. The convergence study was done for the mesh size of the mooring lines as for the time steps of the simulation. The simulations were run for EC1 with an active turbine. For the mesh size of the mooring lines distances of 1, 2, 4, 8, 16 and 32 meters were chosen. 0.05, 0.1, 0.2, 0.4 and 0.8 seconds were chosen for the time step convergence.

It is assumed that the finer the mesh the more accurate the results will be, thus the 1 meter mesh size should be the most accurate. Figure 5.8 shows the difference between the simulations of the different distances between nodes and the 1 meter node distance simulation for the load in the mooring line. The average load in the mooring line during the simulation is 1240 kN . It is clear that the finer the mesh size the more accurate the results are due to the difference with the 1 meter mesh being smaller. However, even for the larger mesh sizes the difference is less than one percent of the total load. It is clear that the difference for the 1, 2 and 4 meter distances between nodes is very small, figure 5.9 shows a zoom-in of these differences.

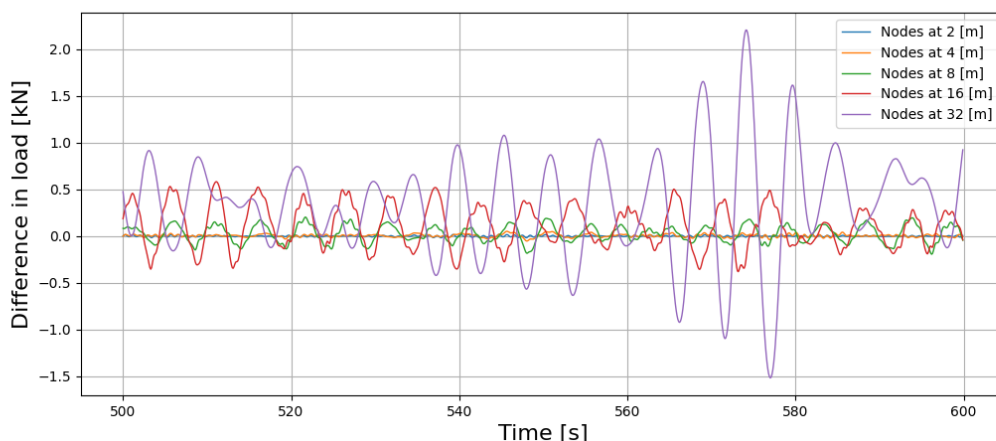


Figure 5.8: Difference for different node distances

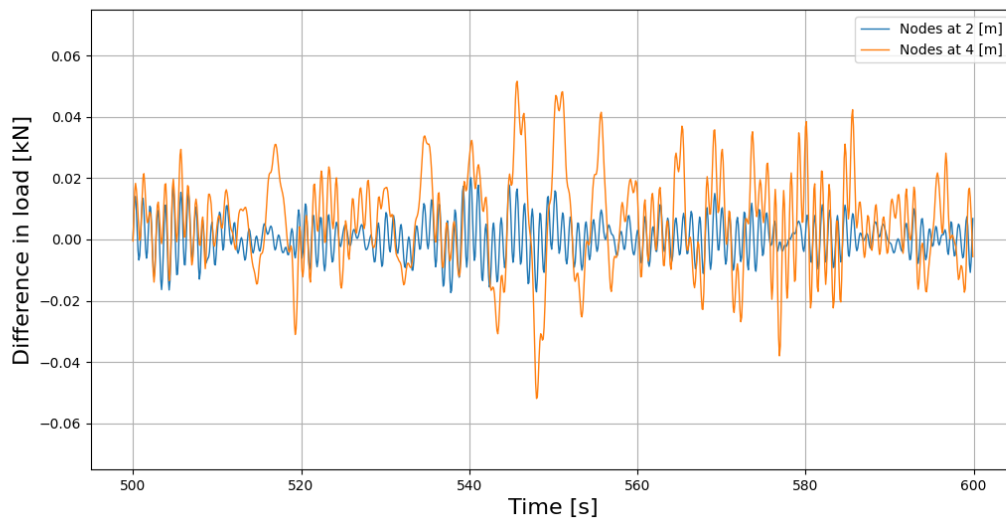


Figure 5.9: Zoomed image for difference for node distances of 1 and 2 meter

Figure 5.10 shows that the choice of a correct time step is more important than the choice for mesh size. The graph shows the difference of the load in the mooring line between the simulation with a time step of 0.05 seconds and the other time steps. The simulation with a time step of 0.8 seconds has a difference of more than one percent. This still isn't very significant but to be very precise a smaller time step needs to be chosen. The difference in calculation time for the simulations was significant with the 0.05 time step taking four times longer than the 0.8 seconds. The reason it isn't 16 times longer is because the simulation with time steps of 0.8 seconds sometimes needed more iterations to find the correct solution.

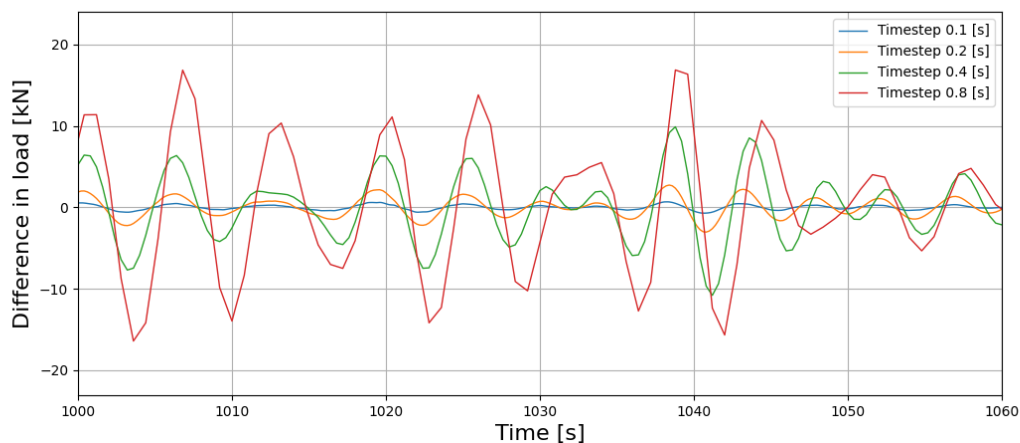


Figure 5.10: Difference for different time steps

Conclusion to the validation

The validation of the model was crucial in ensuring the reliability of the simulation results. While OrcaFlex is widely used in the industry, independent validation is challenging. However, by comparing the simulation results with real-life data from the Hywind Scotland wind farm, the model's performance was effectively assessed, highlighting both its strengths and limitations.

The initial simulations showed significant deviations in turbine inclinations compared to the real-life data,

with the model predicting much larger inclinations. By recalculating the center of gravity using static assumptions and inclination data, the model's accuracy of the real-life data improved. A recalculated COG of 21.39 meters yielded the most accurate results, reducing the root mean square of the inclination differences. However, some discrepancies persisted, likely due to the exclusion of mooring line moments in the calculations and a different type of wind turbine.

When comparing the loads in the delta lines, the simulation results aligned reasonably well with real-life data, particularly for lines under higher tension. The simulated data had less fluctuation than the real-life measurements, mainly because the real wind conditions were variable, while the simulations used constant wind speeds. Although the model provided a good estimate of overall load patterns, it lacked the precision required to predict exact load magnitudes at specific moments.

The analysis of natural frequencies for the mooring and connection lines revealed some differences between the analytical method and the numerical modal analysis, primarily because the analytical method did not account for cable extension under self-weight. Despite this, the modal analysis provided a more realistic depiction of the system's behavior.

The convergence study highlighted that mesh size had a relatively minor impact on the accuracy of the simulation results, with even coarse meshes producing acceptable outcomes. In contrast, time step selection had a more significant effect, with smaller time steps increasing precision but also substantially extending the computational time. A balance between accuracy and efficiency was demonstrated, with finer time steps being necessary for higher precision.

In summary, while the model was not perfectly aligned with real-world data, it showed sufficient accuracy for simulating floating offshore wind turbines. The validation process helped refine the model and demonstrated its capability to simulate key behaviors of FOWTs, though further refinements would improve its precision, particularly in more complex dynamic conditions.

6

Results

This chapter presents the key results and findings from the research. First, a few initial design limitations will be discussed. Next, a physical phenomenon affecting the rotation of the turbines will be explained. Afterwards, the movements of the nacelle and the forces in the mooring lines in a daisy-chained system will be compared to those in a single FOWT to evaluate how the new system performs. Finally, it is examined if the motions of the nacelle don't exceed design limits in governing conditions.

6.1. Design limitations

While setting the scope and making the model of the daisy-chained FOWTs two design limitations were discovered which should be taken into consideration during the design of a FOWT wind farm.

The first design limitation is only applicable for spar floater type floating wind turbines. Spar floaters use crowfoot mooring to create resistance against yaw movements as seen in figure 4.4a. The mooring lines each have an angle of 120 degrees between them. The delta lines creating the crowfoot connect to the mooring bracket attached to the spar floater, each mooring bracket again having an angle of 120 degrees between them. The mooring brackets connect to one delta line of each adjacent mooring line. This makes it impossible to have a line clash between two delta lines. However when designing a triangular daisy chained system a problem occurs. In this case the angle between two connection lines becomes only 60 degrees. When trying to keep the same angle for a crowfoot the delta lines of the two connection lines will have to cross each other. This will create a clash possibility between these lines. There are a few ways to prevent this, the first two are to make the angle between two delta lines in the crowfoot smaller or to completely remove the crowfoot from the design. This will however strongly affect the resistance to yaw rotation in the FOWT. An other solution is to design a hexagonal system, in this case the angles between mooring and connection lines remains 120 degrees. A final solution would be to use a different type of floater like a semi-submersible which has added mass when making a yaw rotation due to its design. In this final case crowfoot mooring wouldn't be needed.

The second design limitation relates to the water depth and the distance between the turbines. As mentioned in section 4.2.2 there is a minimum required distance between wind turbines. In this research a distance of seven times the rotor diameter is taken.[36] This is on the low side of what is suggested in the design of offshore wind farms. Sickler et al. suggests at least ten times the rotor distance between wind turbines.[47] For larger wind turbines this distance can easily be more than 1.5 kilometer. FOWT become convenient from a water depth of 50 meters. With the idea of a daisy-chained wind turbine farm being to save on costs for the installation of anchors it would be counterproductive to then design connection lines with lengths of more than 20 times the water depth. Especially since that these would most likely drag over the seabed causing them to deteriorate at a higher rate and destroying marine life. This means that daisy-chained floating wind turbine farms with conventional wind turbines only make sense for small wind turbines or larger water depths. This could be applicable for regions with

a small population but with large water depths. Islands in the Pacific Ocean for example could be a fitting location for a daisy-chained floating wind turbine farm. When performing a quick calculation, a 5 MW wind turbine with a capacity factor of 40 percent produces 17.520 MWh per year. This is enough to power 4380 European households. Assuming there are on average 2.3 people per household, this equals 60,444 people if a hexagonal wind farm configuration is used [48]. This could completely power the homes of countries and islands such as Greenland, Sint Maarten and the Faeroe Islands.

Another way to resolve this is to not use a conventional wind turbine but a vertical axis wind turbine. These consist of vertical blades connected at the top and bottom of the blade to a vertical axis. They have a smaller physical footprint compared to a conventional wind turbine and have a smaller wake distance in which nearby wind turbines lose power potential [26].

This suggests that depending on the water depth and wind turbine diameter that is required from a farm, there are certain possibilities to build different types of wind farms. In this case the rotor diameter can also be interpreted as the amount of power required from the wind farm. Figure 6.1 shows these different types. There are no values on the axis since that it is dependent of a lot more of different parameters than just water depth and rotor diameter. These parameters would be things like mooring line weight, type of mooring line, soil type, etc. Region A is where the water depth isn't deep enough for FOWTs, which is usually at 50-70 meters. Here bottom-fixed turbines are a possibility. Region B is deep enough for FOWTs but if their rotor diameter is too large they will have wake loss effects. Here vertical axis wind turbines could be a solution to still have the required power output. If the water becomes deeper (region C) daisy-chaining becomes a possibility but it must be avoided that the connection lines scrape over the seabed. This can be done by attaching buoys to the connection line or using lighter lines. For small turbines in deep water (region D) the mooring lines will have a relatively large mass and an unnecessary large floater would be needed. A possible solution is to use lighter mooring lines such as Dyneema. Region E is suitable for the type of daisy-chaining that was previously mentioned in this report.

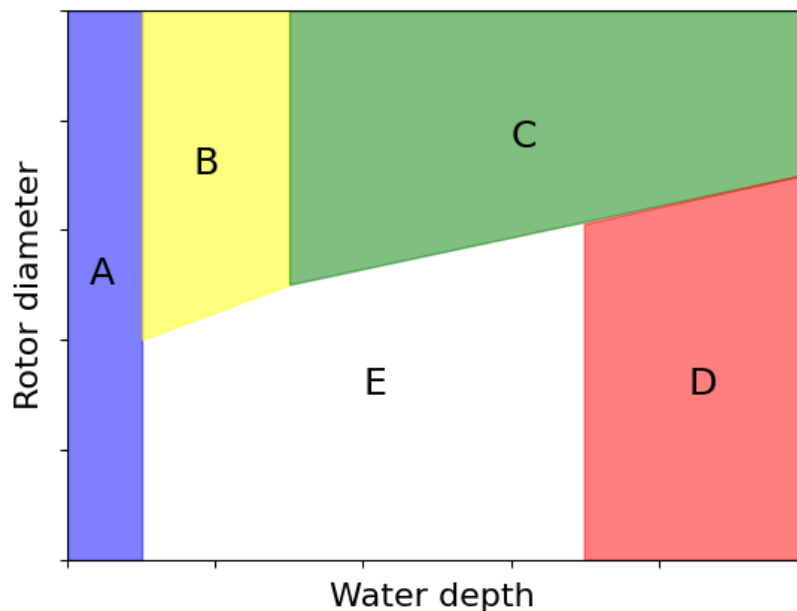


Figure 6.1: Design regions, water depth - rotor diameter relation

6.2. Yaw rotation

When running simulations for the different load cases, nothing out of the ordinary occurred for the first two ECs. However, the third EC yielded interesting results. This scenario featured a significant wave height of 11 meters and a peak period of 20 seconds. Upon examining the simulation files, it became evident that the simulation aborted before reaching the required time limit when the original base case mooring configuration was used, as mentioned in section 4.2.1 with no distancing from the spar. In contrast, when the adapted mooring was employed, the simulation did not abort but still provided intriguing data. Analyzing the data for the rotation around the z-axis of the spar floaters revealed that the cause of the simulations aborting was the excessive spinning of the spar floaters around their z-axis. Figure 6.2 illustrates the yaw rotation of one of the wind turbines in the hexagonal configuration. As shown, the simulation, which was intended to last 2000 seconds, was not completed.

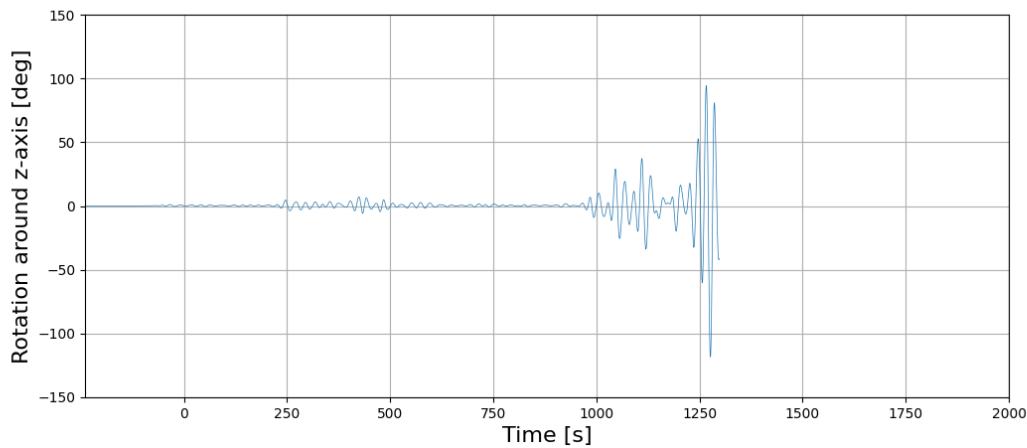


Figure 6.2: Rotation around the z-axis during an aborted simulation

By leaving out certain parameters and inputs for new simulations it was determined that the load RAOs in the model caused this spinning phenomenon to happen. When simulations were run without the load RAOs but exactly the same other parameters, it did not happen. In the model the load RAOs only have a value for surge, heave and roll due to the spar being perfectly symmetric along the z-axis. Thus there are no terms that should force the spar floater to start turning around its z-axis. The reason for the turning motion is thus due to the interaction between the mooring lines and the spar floater. In OrcaFlex it is possible to perform a modal analysis to look at the different modes of the system. It also shows the modes from all individual line-type elements. The modes are ordered from longest period to shortest period or from lowest frequency to highest frequency. The first eighteen modes of the whole system are superpositions of the six DOFs of the three different wind turbines without influence of the mooring and connection lines. For the hexagonal configuration these are the first 30 modes. The modes after that are the first natural frequencies of the connection lines. Examining the motions associated with these initial natural frequencies reveals the source of the rotation around the z-axis for the spar floaters. Due to the resonance of the connection lines, they begin to sway in their first mode, forming a U-shape. This swaying motion in the xy-plane generates a turning moment for the wind turbines. Figure 6.3 provides a sketch of these motions for clarification; please note that the sketch is exaggerated and not to scale to clearly illustrate the movements of the connection lines.

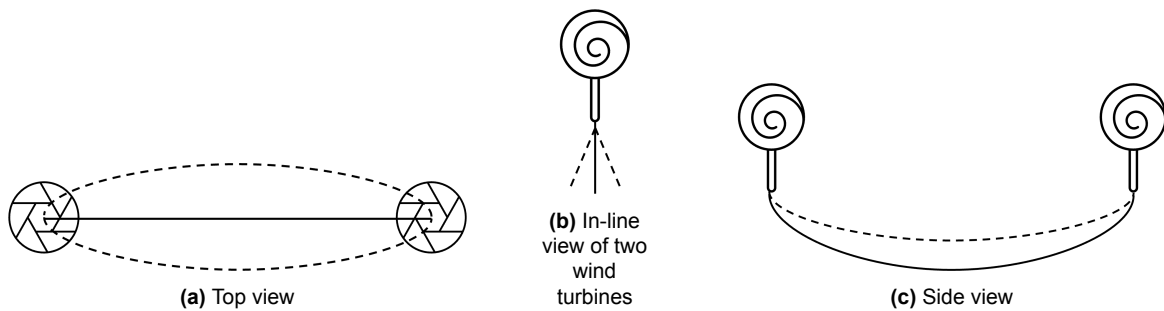


Figure 6.3: Views of the swaying motion of the connection line

Several reasons could contribute to this issue. First, the provided viscous damping for rotation around the z-axis may be incorrect or not applicable to this specific model or environmental conditions. Second, the transition from a crowfoot mooring to a mooring line positioned further from the center of the spar floater could have significantly reduced yaw damping. Lastly, it might be important to consider the first natural frequency of the connection lines during the design of a daisy-chained wind farm because swaying of this line could cause the turbines to spin around their z-axis. In the following sections, the results of various simulations will be discussed to evaluate the effects of these reasons and to assess how realistic these explanations are.

6.2.1. Viscous yaw damping

As mentioned in section 4.2.1 the supplied viscous damping was not specific to these circumstances. Viscous damping is non-linear and dependent of multiple factors. One of those factors is the velocity of the fluid squared. It is possible that the provided viscous damping was for a situation with lower wave heights. Higher wave heights will cause a higher relative fluid velocity. Since it is fluid velocity squared the viscous damping will increase quadratic. To see the effects of this, simulations were run with different viscous damping around the z-axis for the triangular configuration. The simulations were run with no yaw damping, 13000, 26000 and 130000 $kN.m/(rad/s)$ of damping. All simulations were run with EC3 and thus still had a significant wave height of 11 meter and a peak period of 20 seconds. Figure 6.4 shows a segment of the yaw motions of the blue spar floater without the data of the simulations with no damping. This is due to the motions being so large that the data of the other simulations become hard to see. In appendix F.1 graphs are shown with data of all four simulations.

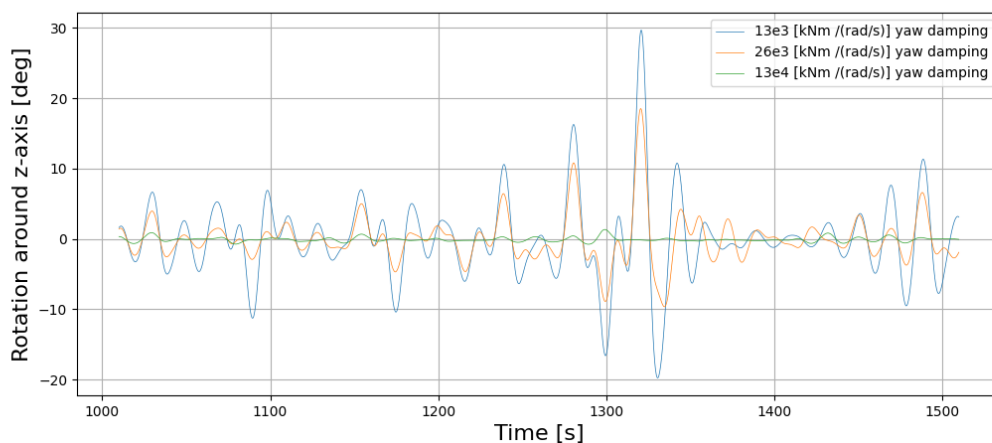


Figure 6.4: Yaw motion blue spar floater for different viscous damping

Analysis of the graphs in appendix F.1 reveals that even with the provided damping and a scenario where the damping is doubled, there remains significant rotation around the z-axis. In the simulation

with ten times the original damping, the yaw motion ranges were recorded as 4.36 degrees, 0.76 degrees, and 2.09 degrees for the green, red, and blue spar floaters, respectively. This indicates that a greater yaw damping value should be implemented for simulations under these ECs. To ascertain the correct damping value at such wave heights and fluid velocities, experimental research is needed.

6.2.2. Crowfoot compared to single mooring line

Replacing the crowfoot with a single mooring line affects the yaw rotation stiffness, even with the adapted mooring as mentioned in section 4.2.1. To see the difference for a crowfoot mooring and a single mooring line multiple simulations were run for the base case. This is done because as mentioned it isn't possible to create a triangular configuration with crowfoot mooring and for the hexagonal configuration the number of lines needed made the simulation unstable. To be able to compare the results the model had to be built in such a way that for both cases (with crowfoot and without) the mode of the natural yaw period had the same length. In the base case this is mode 6. By changing the length of the mooring lines it is possible to create different periods for mode 6. In table 6.1 and 6.2 the length of the mooring lines and the corresponding period for mode 6 are shown for respectively with and without the crowfoot.

Table 6.1: Period for mode 6 per mooring line length with crowfoot

L_M	Period (s)
870	16.20
885	17.32
900	20.29
915	24.99

Table 6.2: Period mode 6 per mooring line length without crowfoot

L_M	Period (s)
939.4	16.19
944.8	17.32
955.6	20.28
969.6	24.97

The amount of yaw motion is dependent of the length of mooring line as can be seen in figure 6.5. Even with a peak period of 20 seconds the simulation where the natural period is 25 seconds gives the largest movements. This is probably due to the mooring lines being longer and giving more space for rotation. The reason the mode might be excited even though the forcing is on a different frequency will be explained in section 6.2.3. A segment of the simulation is taken to show this clearly. With crowfoot mooring the amount of rotation is within a range of 4 to 6 degrees, this isn't a significant amount but does highlight the phenomenon that is happening since that barely any yaw movement at all is expected from a symmetrical object such as a spar floater. Looking at the y-scale of figure 6.6 it is clear that without crowfoot mooring there is significantly more movement around the z-axis. It isn't clear to see what the magnitude is for the simulations with a period of mode 6 of 16 and 17 seconds. Figure 6.7 zooms in on this and compares it to the crowfoot mooring cases.

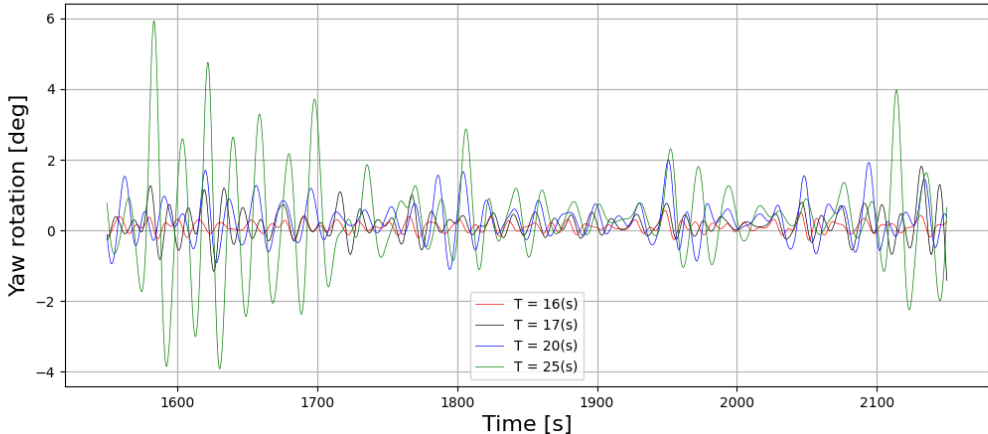


Figure 6.5: Yaw motion for different periods for mode 6 with crowfoot mooring for the base case

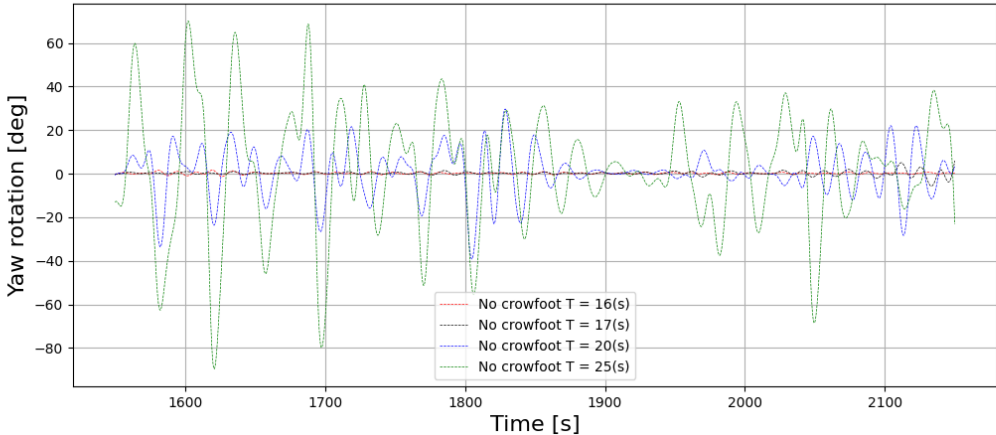


Figure 6.6: Yaw motion for different periods for mode 6 without crowfoot mooring for the base case

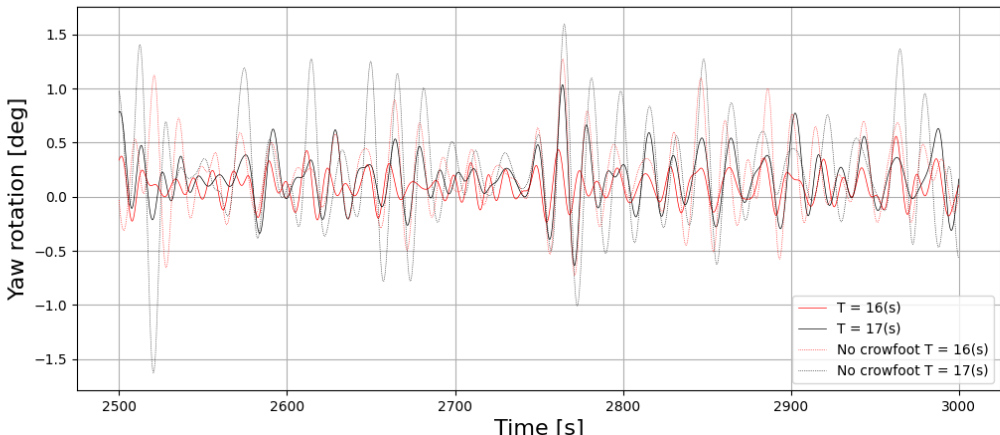


Figure 6.7: Yaw motion for periods of 16 and 17 seconds for mode 6 with and without crowfoot mooring

Looking at the data it is visible that the crowfoot mooring gives a larger resistance to the yaw movement especially for the longer mooring lines with higher mode 6 periods. For the cases with the lower period and shorter mooring lines this is also the case although for the situations without crow foot mooring the yaw movement range is between -1.5 and 1.5 which isn't significantly large. To conclude, changing the crowfoot mooring into a single line with an adapted distance from the center of the floater has effect on the yaw movements. However, crowfoot mooring doesn't completely eliminate a movement around the z-axis and in these cases the length of the mooring line has the largest influence on the amount of rotation.

6.2.3. Modes yaw movement

Looking at the simulations for ECs with a significant wave height of 11 meters and a wave period of 20 seconds for the triangular and hexagonal configurations it is clear that in both situations the spar floaters start turning around their z-axis. As mentioned before this only happens when there are load RAOs applied to the spar floaters. Figure 6.8 shows some of the rotations for spar floaters in the hexagonal configuration. It is clear that although the magnitude is not similar there are significantly large rotations even though the model has viscous damping and altered mooring.

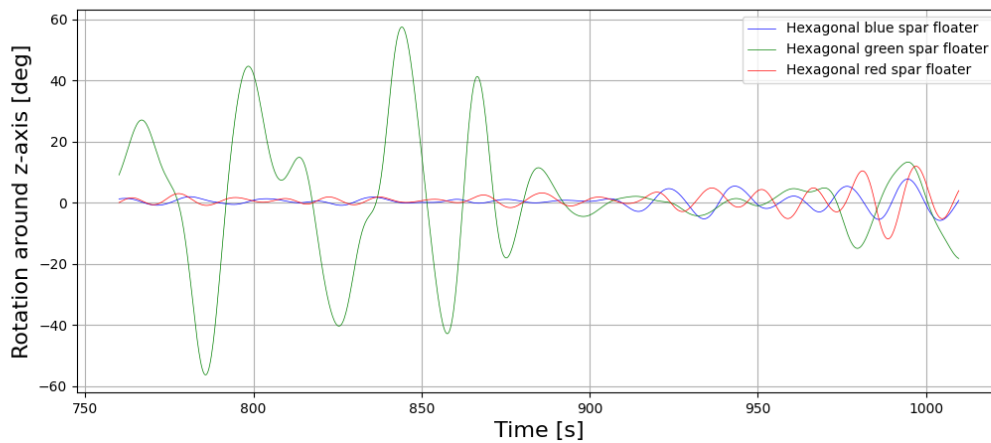


Figure 6.8: Yaw motion for periods of 16 and 17 seconds for mode 6 with and without crowfoot mooring

Looking at the spectral density graphs of the yaw rotation of the six different spar floaters shown in appendix F.2 and figure 6.9 it is clear that not all spar floaters rotate with the same frequency. The highest peaks in the spectral density graphs show the frequency at which they generally rotate. For the white and red spar floater this is at a frequency of 0.065 Hz. Green and blue rotate with a frequency of 0.045 Hz and yellow and pink have a frequency of 0.05 Hz. This means that different modes are exciting the system and making the spar floaters turn at a different rate. It is also interesting to point out that some floaters have a smaller peak at 0.025 Hz. Looking at the modal analysis all these frequencies correspond with a mode where the floaters start to turn due to the connection or mooring lines swaying side-to-side except for the 0.025 Hz peak. This peak corresponds with modes where the entire system sways the floaters in-and-out which makes them turn around all three axes. The modes that are excited are given in table 6.3 with the corresponding frequency.

Table 6.3: Modes exciting the yaw movement in a hexagonal configuration

Mode	Frequency [Hz]	Notes
13-24	0.021	Entire system swinging the spar floaters in-and-outwards
31-42	0.043 – 0.051	Swaying of the connection lines
43-48	0.063	Swaying of the mooring lines

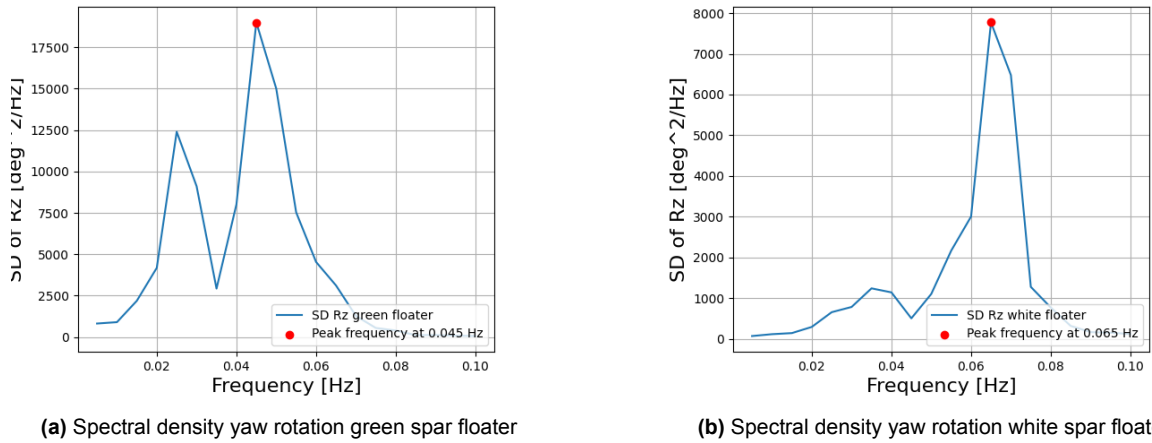


Figure 6.9: Spectral density yaw rotation for green and white spar floater in the hexagonal configuration.

The triangular configuration is used to look at the effect of the ECs direction on the SD of the rotations of the spar floaters. The direction of the environmental conditions doesn't have any effect on the modal analysis since that this is independent of external forcing. Thus all modes remain the same. Looking at the graphs in figure F.3 in appendix F.2 the peaks remain at the same frequencies compared between the two loadcases. Only the heights of the peaks change. The green spar floater however has a new highest peak as can be seen in figure 6.10. This shows that the direction of the environmental conditions has effect on which mode is most present for each spar floater. The modes that have effect on yaw rotation in the triangular configuration are given in table 6.4.

Table 6.4: Modes exciting the yaw movement in a triangular configuration

Mode	Frequency [Hz]	Notes
7-12	0.021 – 0.022	Entire system swinging the spar floaters in-and-outwards
16-18	0.046 – 0.048	Swaying of the connection lines
19-21	0.051 – 0.054	Swaying of the connection and mooring lines
22-24	0.064	Swaying of the mooring lines

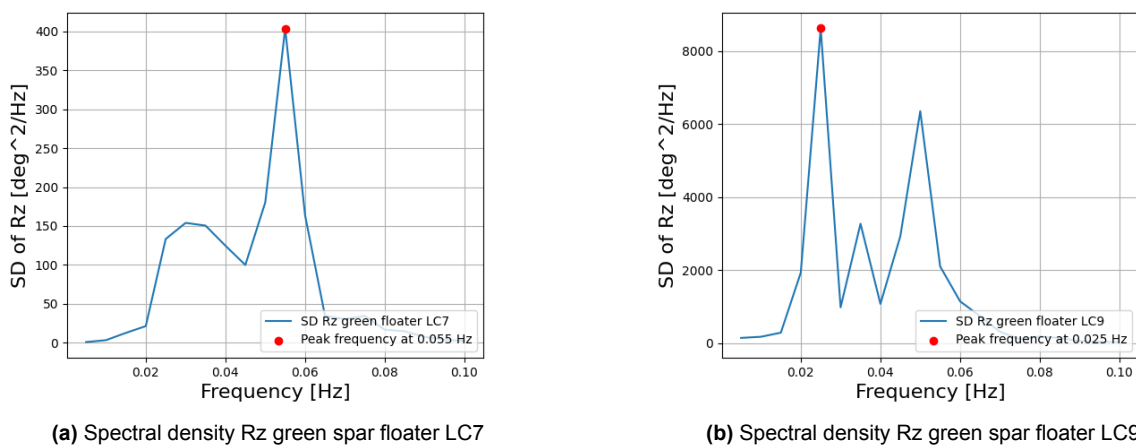


Figure 6.10: Spectral density yaw rotation for the green spar floater in the triangular configuration for LC7 and LC9.

The modes that induce yaw movement do not necessarily align with the wave peak frequency. However, the significant movement observed indicates resonance, contributing to instability in the simulations and

the overall system. The two most likely causes for this phenomenon are mode coupling and parametric resonance. Further research is required to confirm whether either of these phenomena is responsible. Below is a brief explanation of both phenomena and their potential impact on yaw movement.

Mode coupling occurs when two or more distinct vibrational or oscillatory modes of a system interact and exchange energy. While these modes are typically independent, mode coupling leads to interdependence due to interactions or non-linear effects. The entire system of mooring lines and floaters is inherently non-linear, allowing modes with significant energy from the swaying movements of the floaters, induced by the load RAOs, to transfer energy to modes where the spar floats rotate around their z-axis. Additionally, as established in section 6.2.1, the damping associated with yaw movement is relatively lower than that of other movements, creating a pathway of least resistance for energy transfer.

Parametric resonance occurs when a system's parameters, such as stiffness or length, are periodically varied, resulting in increased oscillation amplitudes. The frequency of this parameter variation typically relates to the system's natural frequency, often at double or another multiple of it. In this system, parametric resonance may arise from changes in the natural frequency of the connection lines, which depends on horizontal tension, as shown in equation 5.3. This tension fluctuates over time as the turbines move toward and away from each other.

6.3. Comparison hexagonal configuration to a single wind turbine

The hexagonal configuration performance needs to be compared to the performance of a single FOWT. To do this, simulations are run with the environmental conditions of the eleven cases supplied for the Hywind Scotland farm. These eleven conditions are run for models of a single Hywind Scotland FOWT, the base case model of the 5MW turbine with OC3 floater, the hexagonal configuration with OC3 floaters and a hexagonal configuration with the spar floater from the Hywind Scotland farm. This data can then be compared to the real-life data as well. However since that it was already shown that the model isn't perfectly accurate it is most important to compare the single FOWTs to the hexagonal configurations. The main focus here is the inclination of the spar floaters. The loads in the lines can't be compared because the hexagonal models don't have crowfoot mooring. The loads in the lines can however be compared between the base case and the daisy-chained configuration.

Table 6.5: inclination Hywind turbine model simulations

Case	Hywind data	Hywind Single FOWT	Hywind hexagonal	Lowest mean	Highest mean
1	4.89	4.00	3.70 - 4.35	Pink	White
2	2.56	3.49	3.03 - 3.75	Pink	Green
3	1.14	1.70	1.55 - 1.96	Yellow	Blue
4	3.32	4.04	3.76 - 4.40	Pink	White
5	3.77	4.36	4.11 - 4.77	Pink	White
6	3.92	4.40	4.10 - 4.81	Yellow	Blue
7	4.46	4.51	4.19 - 4.91	Blue	Red
8	3.10	3.78	3.44 - 4.12	Pink	White
9	3.45	3.99	3.68 - 4.34	Pink	White
10	0.69	1.98	1.70 - 2.19	Red	Green
11	0.67	2.01	1.72 - 2.23	Red	Blue

Looking at table 6.5 it is seen from the Hywind Single FOWT column and the Hywind hexagonal column that a hexagonal configuration doesn't perform worse than a single FOWT. The mean of the inclination of a single FOWT falls in the range of the means of all six FOWTs for all eleven cases. This suggests that a daisy-chained wind farm doesn't have a significant effect on the inclination of a FOWT compared to a FOWT with three mooring lines. The last two columns of the table show the spar floater with the least and most inclination. When comparing this with figure 4.6 and table 6.6 which shows the direction the wind is heading towards for each case it suggests the following. The spar floater with the least inclination is upwind in the wind farm and the spar floater with the most inclination is downwind in the

wind farm. Usually it is the downwind floater that is not directly across from the upwind one but the one that is two corners further in the hexagon.

Table 6.6: Wind direction for all eleven cases

Case	1	2	3	4	5	6	7	8	9	10	11
Wind direction [deg]	352	354	351	354	341	326	191	359	355	32	33

Table 6.7 shows the results of the simulations for the 5MW wind turbine. The results are the same as the ones for the Hywind wind turbine with the mean inclination for the single turbine being in the range of the means for the hexagonal configuration. It is clear that this wind turbine is more stable than the Hywind turbine which is to be expected. The spar floater is larger and the distance between the COG and the COB are also relatively further apart. It does show that the model has difficulties modeling idle situations for FOWTs since that the inclination for case 10 and 11 are larger than case 3 which isn't the case with the real-life data.

Table 6.7: Inclination 5MW wind turbine model simulations

Case	5MW base case	5MW hexagonal range	Lowest mean	Highest mean
1	3.22	3.11 - 3.45	Pink	White
2	2.87	2.76 - 3.07	Pink	Green
3	1.31	1.27 - 1.43	Pink	Blue
4	3.18	3.08 - 3.41	Pink	White
5	3.45	3.31 - 3.70	Yellow	White
6	3.52	3.28 - 3.77	Yellow	Blue
7	3.54	3.41 - 3.79	Blue	Red
8	3.07	2.94 - 3.29	Pink	Green
9	3.17	3.07 - 3.40	Pink	White
10	1.76	1.69 - 1.92	Red	Green
11	1.8	1.72 - 1.96	Red	Blue

The loads in the mooring lines for the single turbine and the hexagonal configuration are also compared to each other. Table 6.8 shows the highest force measured in a mooring, this was for all hexagonal cases the line upwind in the farm. Looking at case 3 it suggests that for low environmental conditions the highest load in the mooring line is lower than for the lines of a single turbine. This is probably due to the static state having a lower load. However, for all other cases with heavier environmental conditions the loads are much larger sometimes being 1.5 times as large. Especially comparing to the static state, it shows that this is a very large increase in the load. However, it's important to note that these loads do not exceed those typically experienced in offshore operations [8].

Table 6.8: Highest load in mooring lines in kN

Case	Single	Hexagonal
Static	1042	740
1	1401	1983
2	1410	2017
3	1152	1067
4	1367	1858
5	1390	1957
6	1372	2013
7	1291	1995
8	1410	2017
9	1386	1933
10	1285	1560
11	1290	1607

6.4. Nacelle movements

Besides comparing a single wind turbine to the daisy-chained configuration to see how they perform in regular conditions, it is also important to see if the daisy-chained configuration can handle extreme conditions. This is done by looking at the different parameters that make up the LCs and seeing what their effects are on the acceleration and inclination of the nacelle for extreme conditions. The reason for this is because the acceleration and inclination need to stay within certain design ranges. According to Miguel Taboada et al. the industry recommendations have so far usually limited the maximum accelerations at the nacelle to 0.3-0.4g ($2.9 \text{ m/s}^2 - 3.9 \text{ m/s}^2$), and the maximum inclination to 10° [50]. To start of with the different ECs will be compared for the hexagonal configuration. After that the effects of direction of these conditions will be looked at for the triangular and hexagonal configuration. Finally it will be investigated if the pretension in the mooring lines have effects on the acceleration and inclination of the nacelle. In the last case this will only be done with the triangular configuration because there isn't any data for the hexagonal configuration for different pretension in connection lines. After looking at the movements of the nacelle for each different parameter, the forces in the mooring lines will be looked at for the governing cases.

Environmental conditions

Different cases will be presented of the acceleration of the nacelle to see which load case creates the most acceleration. Only ECs one and two will be compared for the hexagon configuration. This is done because the simulations for environmental condition three were aborted by the software due to them becoming unstable because of the turning movement as described before. This turning movement caused a large acceleration thus comparing this data would give misleading results. Figure 6.11 shows the acceleration and inclination of the nacelle with the largest acceleration and largest inclination per simulation. It is clear that a higher sea-state gives larger accelerations, however the values are still well under the limit. For the inclination it is important to point out the the lower sea-state gives a larger inclination. The reason for this is the blade control. With lower wind speeds the blades are turned in such a way that they catch more wind to produce as much energy as possible. When the wind speed becomes higher the blades turn so they catch less wind and thus the inclination also becomes less. Looking at a thrust force curve in for example 'Description of an 8 MW reference wind turbine' by Cian Desmond et al. or in figure 3.6b it is seen that the most thrust force is at the rated wind speed and that if the wind speed becomes higher it gradually declines [10]. The most thrust force will give the highest inclination. This could explain why case 1 of the validation was the only case where the model underestimated the inclination. It has a wind speed close to the rated wind speed and the model used a different turbine. This would mean that the peak thrust force might have been off and thus the amount of force was underestimated.

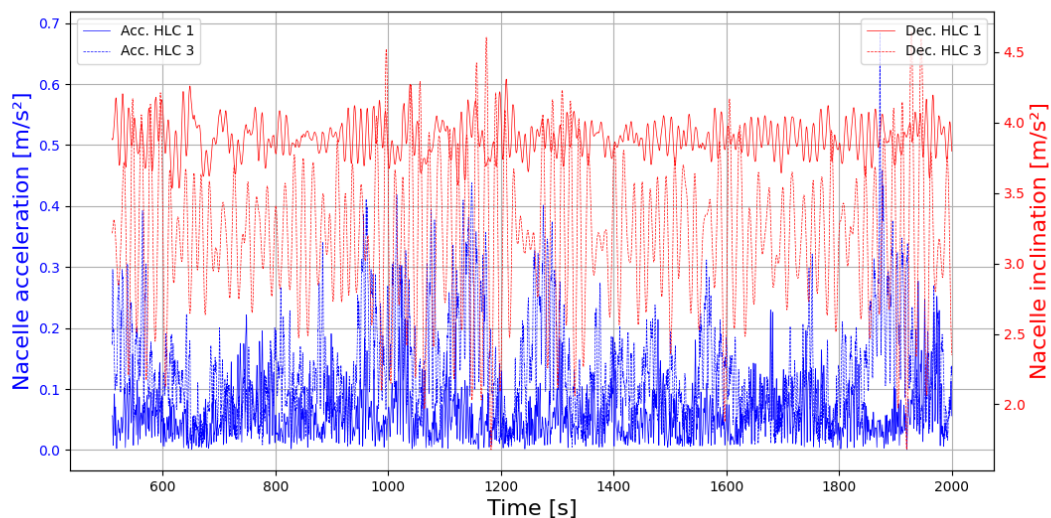


Figure 6.11: Acceleration and inclination for the nacelle for HLC1 and HLC3

Additional simulations were conducted at the rated wind speed of 11.4 m/s to evaluate its impact on nacelle inclination. This wind speed is only slightly lower than that used in EC1, which is 15 m/s. The significant wave height for these simulations was set at 8 meters. Figure 6.12 illustrates the inclination for two nacelles at the rated wind speed. The results indicate a notably higher inclination compared to simulations with higher wind speeds, although it remains below 10° . A key observation is that the variation in inclination is substantially greater for the downwind nacelle compared to the upwind nacelle. This increased variation is likely due to the downwind nacelle's mooring line becoming completely slack, resulting in reduced stiffness and stability for the spar floater.

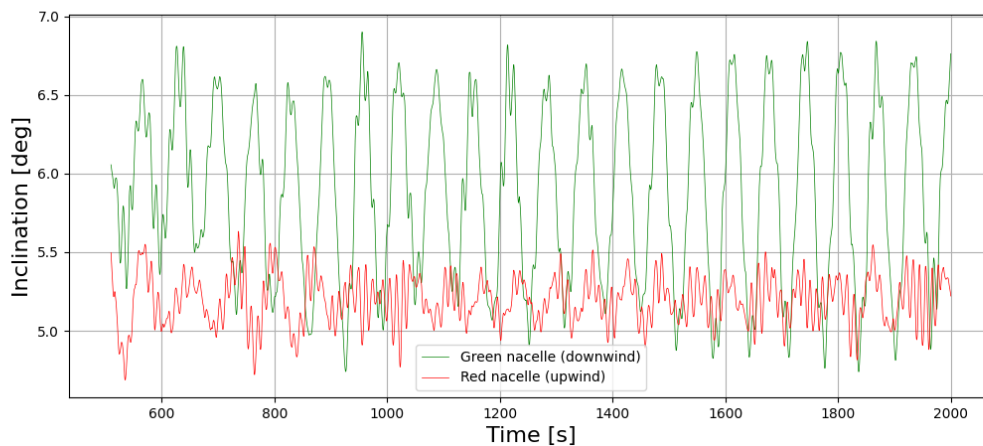


Figure 6.12: Inclination for downwind and upwind nacelles at rated wind speed

Direction environmental conditions

For the direction of the ECs in the hexagonal configuration it is expected that it has little to no effect because the system becomes more circular for every corner added. If the system would be perfectly round it wouldn't matter from which side the wind or waves would come. This suspicion is confirmed in figure 6.13 which shows the inclination of the red nacelle for HLC3 and HLC4. In HLC3 the EC is parallel with the mooring line for the red turbine/nacelle. HLC4 is perpendicular to the connection line between the red and the white turbine. This is only a difference of thirty degrees.

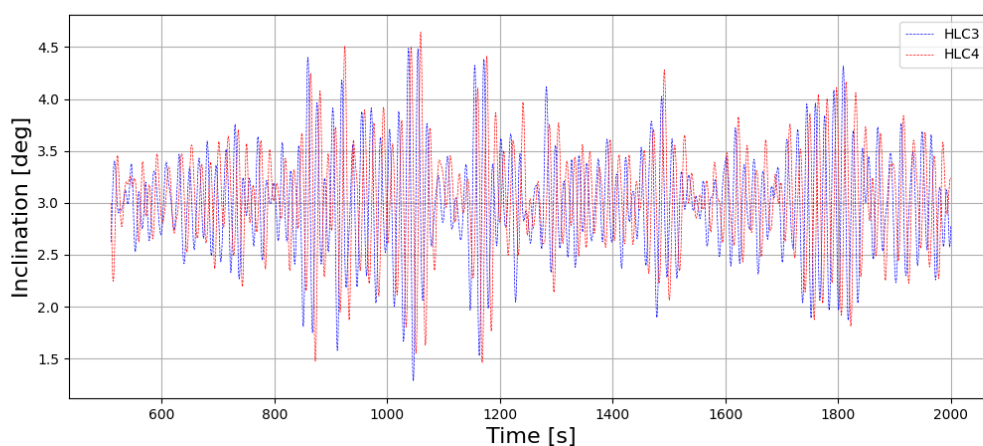


Figure 6.13: Inclination for red nacelle for different EC directions

For the triangular configuration the effect of the direction of the EC on the system is a bit more significant but not critical for the movements. Figure 6.14 shows the inclination for a certain time interval for all

three nacelles for LC1 and LC3. The whole green and blue line overlap (LC1), this is the reason the green line isn't visible. The same applies for the red and blue line for LC3 however these are visible because they are dashed. The reason they overlap is due to the symmetry of the system. For LC2 this wasn't the case however the amplitude of the inclination wasn't effected. As seen below the amplitude of the inclination remains in an allowable range for the design. This confirms that the downwind turbines have the highest inclination in the system but that the direction of the conditions on the system doesn't have a significant influence on the magnitude of the motions.

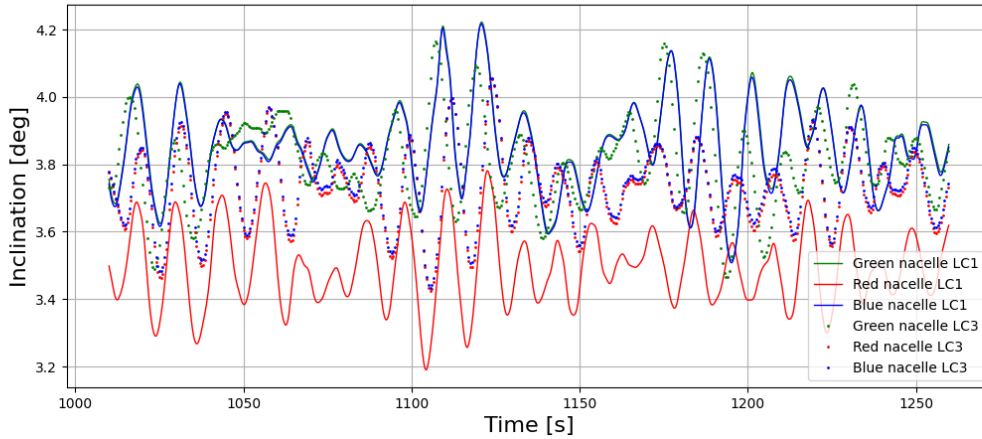


Figure 6.14: Inclination for all three nacelles for LC1 and LC3

Pretension

For the pretension LC1, LC10 and LC19 are compared. Figure 6.15 shows that a difference in pretension doesn't create larger movements for the nacelle. The inclination magnitude remains similar. The spectral density graphs are also the same shape and magnitude.

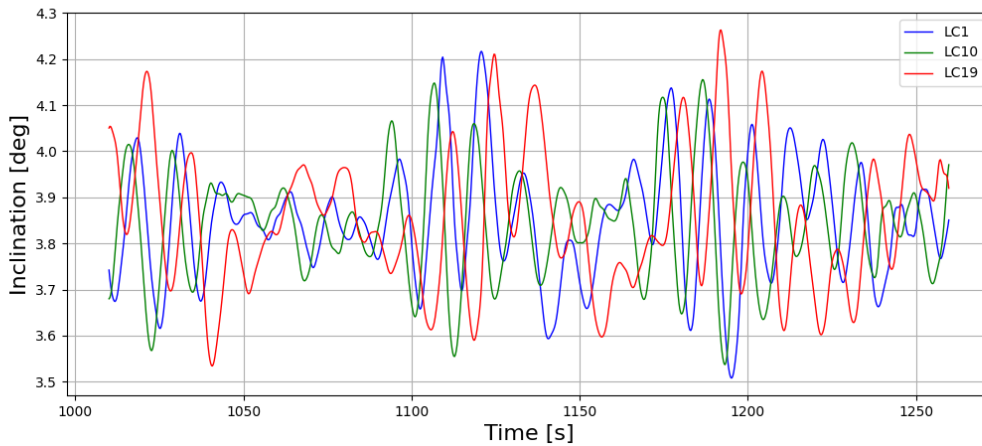


Figure 6.15: Inclination for three load cases with different pretension

Something important to note when changing the pretension is the influence on the modal analysis. The pretension influences the natural frequency of the lines which influences the different frequencies for certain modes. When comparing the spectral density of the yaw rotation of the LC16 with a high pretension to that of the normal pretension, LC7, the differences are easy to see. Shown in figure 6.16 are the spectral density graphs for the yaw rotation of the green floater for different pretensions in the system. It is clear that a higher pretension leads to a higher frequency of movement but also to larger

movements as can be seen on the y-axis. This suggests that the pretension in the system can be used to prevent the rotation of the spar floaters by designing them in such a way that the frequency isn't near the range of the waves exciting the system.

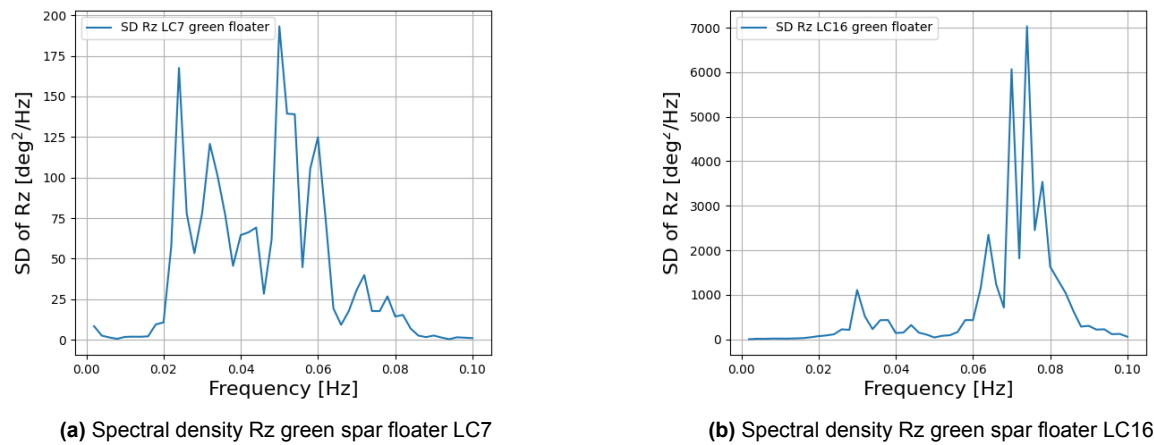


Figure 6.16: Spectral density yaw rotation for the green spar floater in the triangular configuration for LC7 and LC16.

Loads mooring and connection lines

To identify the highest forces in the mooring lines, the scenario with the greatest rotor blade forces, which corresponds to the rated wind speed case, should be examined. Intuitively, the mooring line experiencing the highest effective tension in this scenario is the upwind line in the wind farm, as it must maintain the position of all turbines. Although this report does not aim to provide design-specific conclusions regarding the load capacities that mooring and connection lines must withstand, it focuses on comparing the loads relative to a single FOWT and the static state. As discussed in section 6.3, forces in a hexagonal configuration can increase up to threefold under typical conditions. This section presents findings from the scenario with rated wind speed, which generates the highest thrust, combined with the most severe wave conditions. Table 6.9 lists the maximum loads (in kilonewtons) for each mooring and connection line during the dynamic equilibrium state of the simulation compared to the static state for both the hexagonal configuration and the base case. The EC direction is from the side of the red spar floater. Notably, the maximum force is sometimes lower than the static force because it represents the dynamic equilibrium state, where the spar floaters have stabilized in a new equilibrium position. As shown, the loads in the hexagonal configuration can increase up to four times compared to the static state.

Table 6.9: Highest load in kilonewton in mooring and connection lines for rated wind speed

Line	Maximum	Static
Mooring red	3146	751
Mooring white	2235	750
Mooring blue	651	741
Mooring green	182	735
Mooring yellow	636	734
Mooring pink	2235	742
Connection red - white	1958	656
Connection white - blue	1547	644
Connection blue - green	736	644
Connection green - yellow	726	634
Connection yellow - pink	1552	642
Connection pink - red	1952	647
Base case mooring line 1	1955	1043
Base case mooring line 2	905	1043
Base case mooring line 3	914	1043

7

Conclusion

In this chapter the research question will be answered. This is done by answering the working questions first. With this information future work could expand on this research to come closer to realizing one of many solutions for the challenges in renewable energy. The conclusion to this research can be seen as an advice for individuals or companies interested in designing and building daisy-chained floating wind farms. This research aimed to answer the following question:

"How does daisy-chaining spar floaters influence the motion and stability response in a wind farm?"

1. What parameters have influence on the motion response in a floating wind turbine farm?

The types of parameters that have influence on the motion response are the design parameters of the floating wind turbine and the external forcing parameters. Each parameter will be linked to one of the six degrees of freedom a floating wind turbine has.

First the design parameters will be elaborated on; one of the most important parameters is the distance between the COG and the COB. If the COG and COB are too close to each other the turbine will have a large rotation in pitch or roll with light wind conditions. The concept of a spar floater relies on having a sufficiently large distance between these two points, allowing a slight tilt to create a restoring arm that uprights the wind turbine. A few meters difference in the distance between the COG and COB has a big influence on the inclination of a wind turbine. Based on this research a good rule of thumb to make this distance is at least 20 percent of the total length of the floater. However, this is also dependent on the length of the tower of the wind turbine.

Secondly, for the external parameters the wind has a much larger influence than the waves. Especially since the fact that the wind doesn't need to be extreme to create the largest forces on the system. The wind has an effect on the roll and pitch motions of a turbine and on the sway and surge motions. The roll and pitch create inclination and the surge and sway moves the turbines around creating forces in the mooring and connection lines. The most important parameter for the waves is their peak period, as described in section 6.2.3, which can induce certain motions in the system. This aspect will be addressed further in a different working question.

2. How are the motions of a floating wind turbine influenced by connecting it to another floating wind turbine?

As described in section 6.2.3, due to the connection lines between two floating wind turbines, it is possible to have a resonance where the connection lines start swaying. This resonance creates excessive

movements around the z-axis for the spar floaters. These excessive movements also happen for a single wind turbine but at a lesser extent. The reason it happens more when there are connection lines is because the natural frequency of a connection line is lower (± 0.05 Hz compared to ± 0.07 Hz) than the natural frequency of a mooring line for a single wind turbine. When waves with a lower frequency excite the system they usually have higher significant wave heights. These higher waves put more energy into the system which is divided over the modes that make the spar floaters turn. To prevent this from happening the mooring should be designed in such a way that its natural frequency is not in a range that can coincide with the peak frequency of large waves. This can be done by reducing the weight of the connection lines and adding more horizontal pretension to have a higher natural frequency. Another solution is to increase the weight and lower the natural frequency. Both solutions bring their own new design challenges. A third solution would be to alter the design of the spar floater by creating yaw plates or extending the connection point of the mooring and connection lines outwards.

3. How do the motions and forces in the daisy-chained configuration compare to the base case?

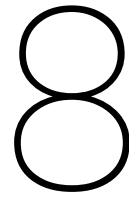
In chapter 4 the base case is defined as a single floating wind turbine. Based on the model presented in this report, connecting floating wind turbines doesn't affect the motions for roll and pitch significantly. Upwind turbines in the farm showed less inclination than a single FOWT. The downwind turbines exhibited a bit more than a single FOWT. This can be taken into consideration when designing a wind farm where there is a dominant wind direction. The downwind spars could then be designed with a lower COG. The motions in surge and sway directions however, are larger in a daisy-chained configuration suggested by the significantly larger loads in the mooring lines. There is more room to stretch the connection and mooring lines. This should be taken into account when designing an umbilical that can handle these motions as well.

As mentioned before, connecting floating wind turbines creates much larger loads in the mooring and connection lines, which can be at least four times higher or lower than the static state, depending on the design. This could cause increased fatigue in the system at a higher rate. This should be taken into account during the design of the mooring system. A possible solution is to add extra mooring lines as redundancy. However, adding extra mooring lines would negate the intended benefit of reducing anchor points.

4. What is the magnitude of the forces in the mooring and connection lines relative to the safe working load of available industry equipment?

Based on this specific case the maximum magnitude of the loads in the mooring and connection lines is approximately 3.1 meganewton. For steel wire rope this is well below the available SWL in the industry.[20] The same goes for marine chains.[8] However, the model doesn't have a built-in function to stop the simulations if the SWL is exceeded for the used lines. The lines used were relatively heavy for their width. The choice (if a steel wire rope is used in a design) of which steel wire rope is used should be fine tuned.

To answer the research question concisely, daisy-chaining floating wind turbines introduces the possibility of creating a system where connection lines can resonate at high sea states. Due to this resonance the spar floaters rotate excessively around their z-axis. If this issue is addressed in the design, a daisy-chained wind farm becomes a feasible solution.



Discussion and recommendations

This chapter provides a discussion on the implications of the results. In addition to this, the limitations of the model are discussed and how this has impacted the results, as well as how these issues might be addressed in future research involving the used model. Additionally, recommendations for separate future research are provided.

Discussion

Looking back at the results and conclusions it seems that it is feasible to create a daisy-chained floating wind farm. However, in many cases it would probably not be the best solution. As mentioned in section 6.1 the circumstances in which a daisy-chained wind farm would be the best feasible solution are quite limited. The ratio between the water depth and the required power should be within certain margins. Even though the world is quite large, finding a suitable location for a daisy-chained floating wind farm would be challenging. The amount of power generated and financial cost, per square kilometer in a daisy-chained floating wind farm, is most likely lower and much costlier than a regular wind or solar farm. However, vertical axis wind turbines might be a feasible solution to increase the amount of power per square kilometer and would be easy to implement in a daisy-chained floating farm.

The design of the mooring system is a crucial aspect of designing a daisy-chained floating wind farm. Not only must it resist the forces acting on the system, but as shown in section 6.2, it can also influence the motions of the wind turbines. For the simulations, steel wire rope with a relatively heavy mass was modelled. This mass affects the natural frequency of a connection or mooring line. The first instinct in designing a connection line with a natural frequency outside the range of the wave frequency is to make it heavier or longer. However, this approach is more costly and complicates installation and maintenance. A potentially counterintuitive solution might be to use polyester rope or Dyneema. When tensioned, these materials would have a significantly higher natural frequency than steel wire rope, which would likely avoid resonance with lower wave conditions. However, the safe working load would be lower compared to steel wire rope or chain. This approach would be especially useful for farms with smaller turbines. Another possibility would be to design a solution where a polyester rope is combined parallel with a slack chain. The polyester rope would be tensioned during calm conditions. When the tension increases and the rope starts stretching, the slack chain starts stretching as well and takes on a larger portion of the force.

Looking at the forces in the mooring lines, the type of mooring lines needed to be able to resist the magnitude of forces would have large dimensions. The dimensions of a steel wire rope would be a diameter of 70 millimeter and a mass of 22 kilogram per meter. For a chain it would be a width of 230 millimeter with a mass of 95 kilogram per meter. Due to the mass, the system would become very stiff and the loads will most likely be very concentrated increasing the risk of failure. Extra monitoring would be needed to ensure that no failure occurs. The redundancy in the system is practically non-existent because if a single mooring line fails all turbines will collide with each other. This could be prevented

by adding an anchor point in the middle of the hexagon and expanding the hexagonal field or designing for safe-life design. To increase the redundancy it could be useful to add two mooring lines on the most outward turbines so that if one fails the entire system doesn't fail. Looking at it from a mooring and connection line point of view a floating solar farm would be a lot more practical for daisy-chaining since the loads would be a lot lower and a collision between solar panels could be damped with bumpers or guide frames.

As described before, many assumptions and simplifications were made for the viscous damping. A provided linear value is used and added on top of the damping obtained from the OrcaWave software. OrcaFlex software uses a linear damping matrix. The problem arises that viscous damping is dependent on the square of the velocity of the surrounding fluid, therefore, it is not linear and cannot be simply added to a linear term. This by itself is already a rough approximation of reality. Additionally, the linear damping term was derived from a free-decay response test and was, therefore, only suitable for that specific case. It is unclear what the conditions of that case were, but it is unlikely that they involved the same water velocity as in the simulations conducted for this research. Because of the quadratic nature of viscous damping a difference in the fluid velocity could quickly result in a large difference in viscous damping terms. To address this in future research, software that implements non-linear damping matrices can be used.

Another simplification in the model is the replacement of the crowfoot mooring by a mooring line that is distanced from the center of the floater. This distancing creates a larger restoring moment with a smaller rotation from the spar floater. However, this does not fully replicate the yaw stiffness provided by the crowfoot mooring. This distancing is also not a feasible design option. However, designing wider spar floaters might solve this problem, though this would increase material costs. Crowfoot mooring is applicable in the hexagonal configuration. However, the software struggled with running simulations due to the number of lines it had to calculate. This issue might be solved by lowering the number of nodes modelled for each delta line or using different software. Running the hexagonal model with crowfoot mooring would have been useful for section 6.2.2 to see if turbines would still rotate around their z-axis.

For the validation, simulations were run with the same turbine as the 5MW wind turbine that is provided by Orcina. The height of the tower is adjusted to that of the Hywind tower but the diameter is unknown and is kept the same. The rotor and nacelle dimensions are also kept the same as the 5MW turbine. It is classified information what the shape of the blades is and what the specifics are of the gearbox in the nacelle for the Hywind Scotland wind farm. The diameter of the rotors is 30 meters larger for the Hywind turbines and each is a 6MW turbine. The decision was made to not alter the diameter since that the code for the rotor pitch and generator torque was specifically written for a 5MW wind turbine. This has implications for the accuracy of the validation but not for the overall results. A larger rotor diameter should give a larger inclination due to the larger thrust force, in the simulations. Another point of discussion for the validation is the provided COG for the model. This is assumed to be incorrect due to the relatively small distance between COG and COB and the fact that the inclination in all the simulations was excessive. The provider of the data and the data description file was contacted about this, but no reply was given. For this reason a new COG was manually calculated making some simplifications and assumptions. It was simplified as a static state, where a new COG was determined using the sum of moments, the average inclination, the force on the rotor, and the system's mass. The forces in the mooring lines were neglected, which introduces some inaccuracy. For the overall research, this does not have significant consequences, but it is worth noting.

Recommendations for further research

To start off, there is a summary of how the limitations of the model can be resolved in future research. Different software could be used that takes non-linear matrices so that viscous damping can be modelled more accurate. Besides that more computational power would be needed to be able to model crowfoot mooring that has significantly more lines and thus nodes to compute in the FEM. A different proposal for the modelling process is to use a vessel-type structure instead of a spar floater in OrcaFlex. In OrcaFlex spar floaters take single linear added mass and damping matrices dependent of a singular

frequency. A vessel-type can incorporate specific matrices for each frequency, which will be slightly more accurate. The vessel type also implements wave drift QTFs. For this research, the wave drift QTF was not highly relevant, as only a single wave train was modeled. However, it will be crucial when simulating more complex wave environments. However, the largest force displacing the floating wind turbine is most likely due to wind rather than wave drift.

Furthermore, extra research can be conducted on this study by exploring the parameters that were kept constant. A few examples are the water depth, the weight of the mooring lines or allocating different directions for the wave and wind forcing. Another parameter that could be changed is the type of floater used in the design. A semi-submersible, for example, would have added mass around the z-axis. This might prevent the yaw rotation created by the swaying of the connection lines. The configuration could also be changed to include two mooring lines per floater to limit the increase in loads, this way it is still possible to cut down the amount of anchor points by 33%. Another configuration that could be tested is a square field or an expanded hexagon farm, although the latter would likely require more advanced software.

Something that was left completely out of the scope of this research are the anchors. It should be looked into whether anchors exist that can bear the loads effectively under various operational conditions. During the simulations, it became evident that some anchors in the system needed the capability to withstand upward forces. The magnitude of these forces has not been investigated. A study could be done to see if it is financially viable to daisy-chain a wind farm, because a reduction in the number of anchors might lead to increased costs in the quality and size of the anchors required. Besides the anchors, it should also be investigated if the umbilicals that transport the power to the coast can withstand the displacements. Due to the daisy-chaining the spar floaters move a lot more. An umbilical should be designed to withstand these movements.

In addition to recommendations on feasibility and design research, further studies should also focus on the theoretical aspects underlying the modeling process and the interpretation of the results. Two possible explanations were given for the excitation of the modes to turn the spar floaters, parametric resonance and mode coupling. An in depth look into the software and the underlying calculations could be done to find out what exactly is the reason of these movements happening. It could also be investigated why the load RAOs have such large effects on the results.

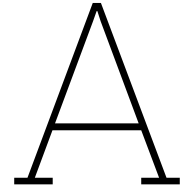
This thesis represents an early step towards overcoming the complex challenges in the design, construction, and operation of daisy-chained floating wind farms. This research contributes to the growing amount of knowledge aimed at advancing renewable energy solutions that are both scalable and sustainable. The findings here pave the way for more resilient designs and more efficient operational models, offering a foundation for future innovation in floating offshore wind technology. As global demand for renewable energy continues to rise, the insights provided by this work not only push the boundaries of current engineering practices but also underscore the potential of floating wind farms to become a transformative element in our transition towards cleaner energy systems. Ultimately, this research serves as a stepping stone, inspiring further advancements that will help unlock the full potential of offshore wind power for generations to come.

References

- [1] Amanda Adams and David Keith. “Are global wind power resource estimates overstated?” In: *Environmental Research Letters* 8 (Mar. 2013), p. 015021. DOI: 10.1088/1748-9326/8/1/015021.
- [2] *Beaufort wind force scale*. Mar. 2016. URL: <https://www.metoffice.gov.uk/weather/guides/coast-and-sea/beaufort-scale>.
- [3] Lars Bergdahl. *Mooring design for WECs*. Dec. 2016, pp. 159–202. DOI: 10.1007/978-3-319-39889-1_{_}7. URL: https://doi.org/10.1007/978-3-319-39889-1_7.
- [4] BVG. *Wind farm costs | Guide to a floating offshore wind farm*. URL: <https://guidetofloatingoffshorewind.com/wind-farm-costs/>.
- [5] Stephan C. Carlson. *Catenary | Mathematics, Physics Engineering*. July 1998. URL: <https://www.britannica.com/science/catenary>.
- [6] Subrata Kumar Chakrabarti. *Hydrodynamics of offshore structures*. WIT press, 1987.
- [7] J. Chung and G.M. Hulbert. “A time integration algorithm for structural dynamics with improved numerical dissipation: the Generalized- α method”. In: *Journal of Applied mechanics* 60/ (June 1993), pp. 371–375.
- [8] Damen. *Studlink chain offshore*. May 2016. URL: <https://www.damenmc.com/wp-content/uploads/2023/04/Product-Sheet-Chain-Studlink-Offshore-may-2016-1.pdf> (visited on 05/27/2024).
- [9] TU Delft. *Aerodynamic loading*. 2023. URL: <https://brightspace.tudelft.nl/d2l/le/content/520136/viewContent/3103538/View>.
- [10] Cian Desmond et al. “Description of an 8 MW reference wind turbine”. In: *Journal of Physics: Conference Series* 753 (Sept. 2016), p. 092013. DOI: 10.1088/1742-6596/753/9/092013.
- [11] DNVGL. “DNVGL-ST-0119 Floating Wind Turbine Structures: Technical Report”. In: (2018).
- [12] DNVGL. *Floating Wind: Turning ambition into action*. Tech. rep. Nov. 2022. URL: <https://www.dnv.com/focus-areas/floating-offshore-wind/floating-wind-turning-ambition-into-action/>.
- [13] Rubén Durán Vicente et al. *Pathway to cost reduction in floating wind technology*. Tech. rep. Mar. 2020. URL: <https://corewind.eu/wp-content/uploads/files/presentations/Pathway-to-cost-reduction-in-floating-wind-technology.pdf>.
- [14] EWEA. *Deep water: the next step for offshore wind energy*. Tech. rep. 978-2-930670-04-1. July 2013. URL: www.ewea.org/report/deep-water.
- [15] O. M. Faltinsen. *Sea loads on ships and offshore structures*. Oct. 1990. URL: <http://fipak.areeo.ac.ir/site/catalogue/18314286>.
- [16] Casey M. Fontana et al. “Multiline anchor force dynamics in floating offshore wind turbines”. In: *Wind energy* 21.11 (July 31, 2018), pp. 1177–1190. DOI: 10.1002/we.2222. URL: <https://doi.org/10.1002/we.2222>.
- [17] M.A. van der Giessen. *Feasibility of mooring system optimization for floating wind turbines in deep water based on static analysis | TU Delft Repository*. June 2021. URL: <https://resolver.tudelft.nl/uuid:97b54836-a075-4404-bab3-84d9075f68ed>.
- [18] CGP Grey. *Hexagons are the Bestagons*. Nov. 2020. URL: <https://www.youtube.com/watch?v=th0ifuHs6eY>.
- [19] O. M. Griffin and F. Rosenthal. “The dynamics of Slack Marine cables”. In: *Journal of offshore mechanics and Arctic engineering* 111.4 (Nov. 1989), pp. 298–302. DOI: 10.1115/1.3257098. URL: <https://doi.org/10.1115/1.3257098>.

- [20] Hendrik Veder Group. *Steel wire rope*. Tech. rep. URL: https://www.hendrikvedergroup.com/wp-content/uploads/2021/02/2-HVG-Catalogus_TAB_4-Steel-wire-rope.pdf.
- [21] GWEC. *Global Wind Report 2024*. Tech. rep. Apr. 2024. URL: https://gwec.net/wp-content/uploads/2024/04/GWR-2024_digital-version_final-1.pdf.
- [22] Matthew Hall and Andrew Goupee. "Validation of a lumped-mass mooring line model with DeepCwind semisubmersible model test data". In: *Ocean Engineering* 104 (2015), pp. 590–603. ISSN: 0029-8018. DOI: <https://doi.org/10.1016/j.oceaneng.2015.05.035>. URL: <https://www.sciencedirect.com/science/article/pii/S0029801815002279>.
- [23] Martin Hansen. *Aerodynamics of wind turbines*. May 2015. DOI: 10.4324/9781315769981. URL: <https://doi.org/10.4324/9781315769981>.
- [24] K. Hasselmann et al. *Measurement of Wind-Wave Growth and Swell Decay during the Joint North Sea Wave Project (JONSWAP)*. *Suppl. A*. Deutsches Hydrographisches Institut, 1973.
- [25] Leo H. Holthuijsen. *Waves in Oceanic and Coastal Waters*. Cambridge University Press, 2007. DOI: 10.1017/CB09780511618536.
- [26] M Huang. *Wake and wind farm aerodynamics of vertical axis wind turbines* | *TU Delft Repository*. DOI: 10.4233/uuid:14619578-e44f-45bb-a213-a9d179a54264. URL: <https://resolver.tudelft.nl/uuid:14619578-e44f-45bb-a213-a9d179a54264>.
- [27] *Hywind Scotland*. URL: <https://www.equinor.com/energy/hywind-scotland>.
- [28] J. Jonkman. *Definition of the floating system for Phase IV of OC3*. Tech. rep. May 2010. DOI: 10.2172/979456. URL: <https://doi.org/10.2172/979456>.
- [29] Journé and Massie. *Offshore Hydromechanics*. 1st ed. Jan. 2001.
- [30] László P. Kollár and Gabriella Tarján. "8 - Basics of vibration". In: *Mechanics of Civil Engineering Structures*. Ed. by László P. Kollár and Gabriella Tarján. Woodhead Publishing Series in Civil and Structural Engineering. Woodhead Publishing, 2021, pp. 299–343. ISBN: 978-0-12-820321-7. DOI: <https://doi.org/10.1016/B978-0-12-820321-7.00008-3>. URL: <https://www.sciencedirect.com/science/article/pii/B9780128203217000083>.
- [31] Kai-Tung Ma et al. "Chapter 4 - Mooring design". In: *Mooring System Engineering for Offshore Structures*. Ed. by Kai-Tung Ma et al. Gulf Professional Publishing, 2019, pp. 63–83. ISBN: 978-0-12-818551-3. DOI: <https://doi.org/10.1016/B978-0-12-818551-3.00004-1>. URL: <https://www.sciencedirect.com/science/article/pii/B9780128185513000041>.
- [32] Kai-Tung Ma et al. "Chapter 5 - Mooring analysis". In: *Mooring System Engineering for Offshore Structures*. Ed. by Kai-Tung Ma et al. Gulf Professional Publishing, 2019, pp. 85–114. ISBN: 978-0-12-818551-3. DOI: <https://doi.org/10.1016/B978-0-12-818551-3.00005-3>. URL: <https://www.sciencedirect.com/science/article/pii/B9780128185513000053>.
- [33] Kai-Tung Ma et al. "Chapter 8 - Anchor selection". In: *Mooring System Engineering for Offshore Structures*. Ed. by Kai-Tung Ma et al. Gulf Professional Publishing, 2019, pp. 155–174. ISBN: 978-0-12-818551-3. DOI: <https://doi.org/10.1016/B978-0-12-818551-3.00008-9>. URL: <https://www.sciencedirect.com/science/article/pii/B9780128185513000089>.
- [34] Kai-Tung Ma et al. "Chapter 9 - Hardware—off-vessel components". In: *Mooring System Engineering for Offshore Structures*. Ed. by Kai-Tung Ma et al. Gulf Professional Publishing, 2019, pp. 175–198. ISBN: 978-0-12-818551-3. DOI: <https://doi.org/10.1016/B978-0-12-818551-3.00009-0>. URL: <https://www.sciencedirect.com/science/article/pii/B9780128185513000090>.
- [35] Robert McNeel. *Rhinoceros 3D*. URL: <https://www.rhino3d.com/>.
- [36] Johan Meyers and Charles Meneveau. "Optimal turbine spacing in fully developed wind farm boundary layers". In: *Wind energy* 15.2 (Apr. 2011), pp. 305–317. DOI: 10.1002/we.469. URL: <https://doi.org/10.1002/we.469>.
- [37] Laurens Moerland. *Jumbo Offshore completes another first by installing Petrobras torpedo pile mooring system with just one vessel*. Sept. 2022. URL: <https://www.jumbomaritime.nl/of-fshore/jumbo-offshore-completes-another-first-by-installing-petrobras-torpedo-pile-mooring-system-with-just-one-vessel/>.

- [38] *Offshore Renewable Energy | Innovation Centre | ORE Catapult*. URL: <https://ore.catapult.org.uk/>.
- [39] Orcina. *K01 5MW spar FOWT*. Tech. rep. 2018. URL: <https://www.orcina.com/wp-content/uploads/examples/k/k01/K01%205MW%20spar%20FOWT.pdf>.
- [40] Orcina. *K03 15MW semi-sub FOWT*. Tech. rep., pp. 1–12. URL: <https://www.orcina.com/wp-content/uploads/examples/k/k03/K03%2015MW%20semi-sub%20FOWT.pdf>.
- [41] Orcina. *Orcaflex Manual*. 2024. URL: <https://www.orcina.com/>.
- [42] R Pool. *Deep water wind turbines*. Oct. 2010.
- [43] A. Ross and Orcina Ltd. *Wind Turbine Validation Report*. Tech. rep. 01. Apr. 2018, pp. 1–66. URL: <https://www.orcina.com/wp-content/uploads/resources/validation/R14050101-Wind-Turbine-Validation-Report.pdf>.
- [44] Saegusa and NEDO. *NEDO's activities toward expansion of floating offshore wind power generation*. July 7, 2022. URL: <https://www.nedo.go.jp/content/100949195.pdf>.
- [45] Camiel Schreuder. “Evaluating the feasibility of shared mooring systems on a combined solar and wind farm array”. 2023.
- [46] S Sharma and Vikram University. *Metacenter and metacentric height*. URL: https://vikramuniv.ac.in/files/wp-content/uploads/BE_ME_4th_sem_Metacenter__MetacentricHeight_Shivam_Sharma.pdf.
- [47] Maaik Sickler et al. “Offshore Wind farm optimisation: A comparison of performance between regular and irregular wind turbine layouts”. In: *Wind energy science* 8.7 (Oct. 2022), pp. 1225–1233. DOI: 10.5194/wes-8-1225-2023. URL: <https://doi.org/10.5194/wes-8-1225-2023>.
- [48] Tsemekidi-Tzeiranaki Sofia et al. “Energy consumption and energy efficiency trends in the EU-28 for the period 2000-2016”. In: *JRC Science for policy report* (Jan. 2018). DOI: 10.2760/574824. URL: <https://publications.jrc.ec.europa.eu/repository/handle/JRC114100>.
- [49] V. Sundar. *Ocean Wave Mechanics: Applications in Marine structures*. John Wiley Sons, Feb. 2015.
- [50] Miguel Taboada et al. “An Evaluation of the Effect that Motions at the Nacelle have on the Cost of Floating Offshore Wind Turbines”. In: OTC Offshore Technology Conference Day 2 Tue, May 05, 2020 (May 2020), D021S019R004.
- [51] Yutaka Tanaka. “Active vibration compensator on moving vessel by hydraulic parallel mechanism”. In: *International journal of hydromechatronics* 1.3 (Jan. 2018), p. 350. DOI: 10.1504/ijhm.2018.094887. URL: <https://doi.org/10.1504/ijhm.2018.094887>.
- [52] M.J. Tucker, P.G. Challenor, and D.J.T. Carter. “Numerical simulation of a random sea: a common error and its effect upon wave group statistics”. In: *Applied Ocean Research* 6.2 (1984), pp. 118–122. ISSN: 0141-1187. DOI: [https://doi.org/10.1016/0141-1187\(84\)90050-6](https://doi.org/10.1016/0141-1187(84)90050-6). URL: <https://www.sciencedirect.com/science/article/pii/0141118784900506>.
- [53] Vryhof. *Vryhof Manual: The Guide to Anchoring*. 5th ed. Jan. 2015. URL: https://www.plaisance-pratique.com/IMG/pdf/Vryhof_Anchor_Manual2015.pdf.



Elastic mooring equations

When including elasticity in the mooring equations it becomes non-linear and there are no general analytical solutions. Numerical tools are needed to solve the equations such as a FEM solver to solve it such as OrcaFlex [41]. Figure A.1 shows an element of the mooring line. $d\psi$ denotes the displacement in the direction normal to the mooring line, $d\phi$ denotes the displacement in the direction tangential to the mooring line. A difference with the static solution is the change in length of a segment by $T/(EA)$.

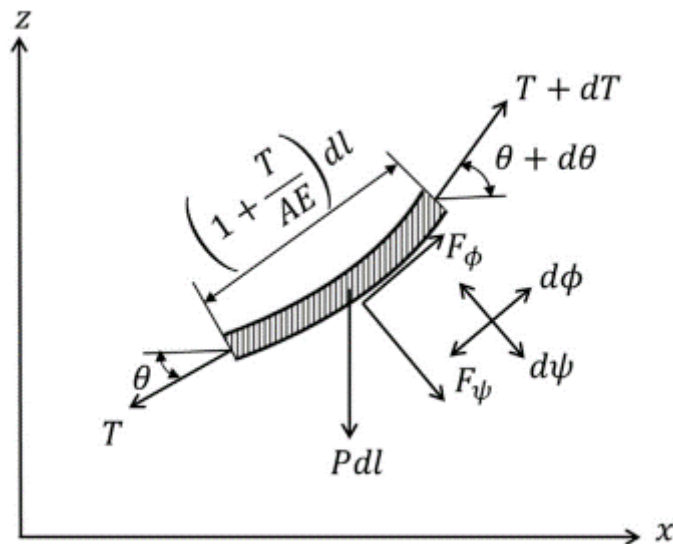


Figure A.1: Forces on an element of a mooring line with elasticity (Ma et al., 2019)[32]

Line bending and torsional stiffness are not taken into account since they are insignificant for chains, wires and ropes with a large curvature. This gives the following equations per element segment based on Newton's second law of motion.

$$-T + (T + dT) \cos d\theta - P \sin \theta dl + F_\phi \left(1 + \frac{T}{EA}\right) dl = m \frac{d^2 \phi(l)}{dt^2} \quad (\text{A.1})$$

$$(T + dT) \sin d\theta - P \cos \theta dl - F_\psi \left(1 + \frac{T}{EA}\right) dl = m \frac{d^2 \psi(l)}{dt^2} \quad (\text{A.2})$$

This can be rewritten knowing that for an infinitesimal element dl the $\cos d\theta = 1$, $\sin d\theta = d\theta$ and $dT, d\theta = 0$ applies.

$$dT - P \sin \theta \, dl + F_\phi \left(1 + \frac{T}{EA}\right) dl = m \frac{d^2 \phi(l)}{dt^2} \quad (\text{A.3})$$

$$T \, d\theta - P \cos \theta \, dl - F_\psi \left(1 + \frac{T}{EA}\right) dl = m \frac{d^2 \psi(l)}{dt^2} \quad (\text{A.4})$$

When calculating the hydrodynamic forces with a combination of Morison equations for a moving structure in still water and moving water around a still structure the following equations can be found based on force dynamic balance. This is the relationship between the (x, z) coordinate system and (l, θ) .

$$dx = \left(1 + \frac{T}{EA}\right) \cos \theta \, dl \quad (\text{A.5})$$

$$dz = \left(1 + \frac{T}{EA}\right) \sin \theta \, dl \quad (\text{A.6})$$

The relationship between (x, z) and (ϕ, ψ) can also be established. These formulas rotate the coordinate system in the direction of the mooring line.

$$d\psi = dz \cos \theta - dx \sin \theta \quad (\text{A.7})$$

$$d\phi = dx \cos \theta - dz \sin \theta \quad (\text{A.8})$$

It is possible to solve these equations numerically with appropriate boundary conditions. These boundary conditions are the location of the connection point too the floating structure, the seabed conditions and the properties of the mooring line.

B

NREL 5MW and OC3 Hywind spar

This appendix shows the main properties of the the NREL 5MW wind turbine and the OC3 Hwind spar floater.

B.1. NREL 5 MW wind turbine

Table B.1: Data overview of the 5MW turbine

Property	Value	Unit
Rating	5	[MW]
Blade quantity	3	[-]
Rotor diameter	126	[m]
Hub diameter	3	[m]
Cut-in, Rated, Cut-out wind speed	3 , 11.4 , 25	[m/s]
Main shaft tilt	5	[°]
Rotor mass	110	[tonne]
Nacelle mass	240	[tonne]
Tower mass	347.46	[tonne]

Table B.2: Properties of the 5MW blades

Property	Value	Unit
Blade material	Glass fiber	[-]
Blade length (root to tip)	61.5	[m]
Overall blade mass	17.7	[tonne]
Radial center of mass (relative to blade root)	20.475	[m]
Blade pre-cone angle	2.5	[°]

Table B.3: Drivetrain properties

Property	Value	Unit
Gearbox ratio	97:1	[-]
Rated rotor speed	12.1	[rpm]
Rated generator speed	1173.7	[rpm]
Generator inertia about high-speed shaft	0.534	[tonne · m ²]

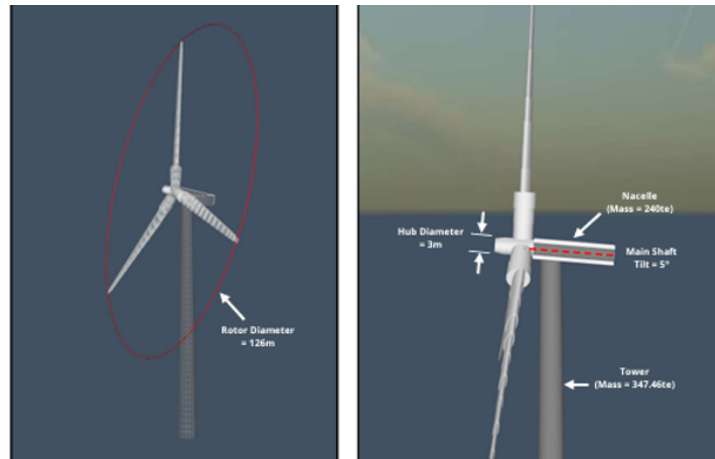


Figure B.1: Wind turbine system (A. Ross, 2018) [43]

B.2. Tower

Table B.4: Geometric properties of the tower

Property	Value	Unit
Length	77.6	[m]
Base elevation (relative to SWL)	+10.0	[m]
Base outer diameter	6.5	[m]
Base wall thickness	0.027	[m]
Top elevation (relative to SWL)	+87.6	[m]
Top outer diameter	3.87	[m]
Top wall thickness	0.019	[m]

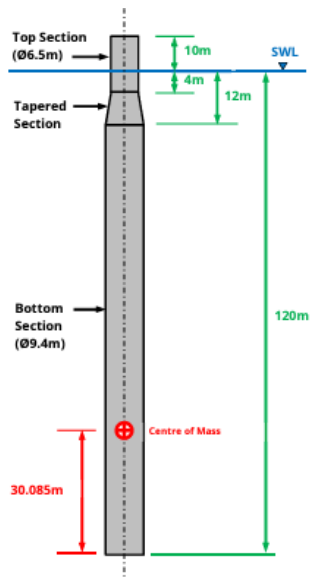
Table B.5: Physical properties of the tower

Property	Value	Unit
Overall integrated mass	249.718	[tonne]
COG location (above SWL)	43.318	[m]
Material	Steel	[-]
Material effective density	8.50	[tonne/m ³]
Material Young's modulus	210	[GPa]
Material Shear Modulus	80.8	[GPa]
Poisson ratio	0.30	[-]
C_a	1.00	[-]
C_d	1.20	[-]

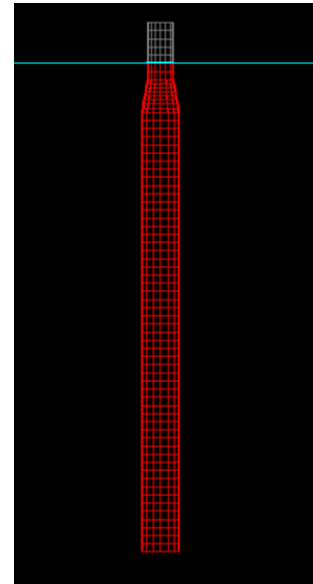
B.3. OC3 Hywind spar floater

Table B.6: Spar floater geometric properties

Property	Value	Unit
Overall length	130	[m]
Total draft	120	[m]
Elevation to floater top	10	[m]
Top section OD / length	6.5 / 14	[m]
Tapered section length	8	[m]
Bottom section OD / length	9.4 / 108	[m]



(a) Spar floater geometry (static position) (A. Ross, 2018) [43]



(b) Mesh view of the spar floater in OrcaWave

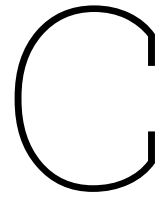
Figure B.2: Spar floater

Table B.7: Spar floater structural properties

Property	Value	Unit
Overall mass	7466	[tonne]
Sea water displacement	8029	[tonne]
Roll inertia	4229230	[tonne · m ²]
Pitch inertia	4229230	[tonne · m ²]
Yaw inertia	164230	[tonne · m ²]
COG (rel. to platform base)	30.085	[m]

Table B.8: Spar floater hydrodynamic properties

Property	Value	Unit
Normal drag coefficient	0.60	[-]
Normal added mass coefficient	0.97	[-]
Normal inertia coefficient	1.97	[-]
Axial inertia coefficient	1.00	[-]



Load RAOs, added mass and damping matrices

C.1. Load RAOs

Table C.1: Haskind load RAOs

Period [s]	Surge	Heave	Roll
	Amplitude [kN/m]	Amplitude [kN/m]	Amplitude [kN.m/m]
4	603.2	39.8	2998.2
6	967.5	135.2	1.10E+04
8	1109.7	209.9	2.12E+04
10	1177.5	251.8	3.22E+04
11	1189.5	261.2	3.72E+04
12	1187.8	263.3	4.14E+04
14	1149.3	248.9	4.68E+04
16	1078.7	217.1	4.86E+04
18	992.5	176.3	4.79E+04
20	902.5	132.6	4.58E+04
22	815.5	89.8	4.28E+04
24	735.0	49.8	3.96E+04
26	662.3	13.3	3.65E+04
28	597.4	19.3	3.34E+04
30	540.0	48.3	3.06E+04
32	489.4	74.0	2.80E+04

Table C.2: Diffraction load RAOs

Period [s]	Surge	Heave	Roll
	Amplitude [kN/m]	Amplitude [kN/m]	Amplitude [kN.m/m]
4	612.1	40.0	3029.24
6	974.9	135.3	1.11E+04
8	1117.4	210	2.13E+04
10	1185.4	251.9	3.24E+04
11	1197.5	261.3	3.75E+04
12	1195.8	263.5	4.17E+04
14	1157.1	249.2	4.71E+04
16	1086.1	217.4	4.90E+04
18	999.4	176.6	4.83E+04
20	908.8	132.9	4.61E+04
22	821.2	90.1	4.32E+04
24	740.2	50.1	3.99E+04
26	667	13.6	3.67E+04
28	601.7	19.1	3.37E+04
30	543.9	48.1	3.08E+04
32	492.9	73.8	2.82E+04

C.2. Added mass matrices

$T_p : 11s$

$$\begin{bmatrix}
 8089 \text{ tonne} & 0 & 0 & 0 & -4.91 \times 10^5 \text{ tonne} \cdot \text{m} & 0 \\
 0 & 8089 \text{ tonne} & 0 & 4.91 \times 10^5 \text{ tonne} \cdot \text{m} & 0 & 0 \\
 0 & 0 & 280 \text{ tonne} & 0 & 0 & 0 \\
 0 & 4.91 \times 10^5 \text{ tonne} \cdot \text{m} & 0 & 3.85 \times 10^7 \text{ tonne} \cdot \text{m}^2 & 0 & 0 \\
 -4.91 \times 10^5 \text{ tonne} \cdot \text{m} & 0 & 0 & 0 & 3.85 \times 10^7 \text{ tonne} \cdot \text{m}^2 & 0 \\
 0 & 0 & 0 & 0 & 0 & 0
 \end{bmatrix}$$

$T_p : 16s$

$$\begin{bmatrix} 8089 \text{ tonne} & 0 & 0 & 0 & -4.93 \times 10^5 \text{ tonne} \cdot \text{m} & 0 \\ 0 & 8089 \text{ tonne} & 0 & 4.93 \times 10^5 \text{ tonne} \cdot \text{m} & 0 & 0 \\ 0 & 0 & 283 \text{ tonne} & 0 & 0 & 0 \\ 0 & 4.93 \times 10^5 \text{ tonne} \cdot \text{m} & 0 & 3.86 \times 10^7 \text{ tonne} \cdot \text{m}^2 & 0 & 0 \\ -4.93 \times 10^5 \text{ tonne} \cdot \text{m} & 0 & 0 & 0 & 3.86 \times 10^7 \text{ tonne} \cdot \text{m}^2 & 0 \\ 0 & 0 & 0 & 0 & 0 & 0 \end{bmatrix}$$

 $T_p : 20s$

$$\begin{bmatrix} 8075 \text{ tonne} & 0 & 0 & 0 & -4.93 \times 10^5 \text{ tonne} \cdot \text{m} & 0 \\ 0 & 8075 \text{ tonne} & 0 & 4.93 \times 10^5 \text{ tonne} \cdot \text{m} & 0 & 0 \\ 0 & 0 & 281 \text{ tonne} & 0 & 0 & 0 \\ 0 & 4.93 \times 10^5 \text{ tonne} \cdot \text{m} & 0 & 3.86 \times 10^7 \text{ tonne} \cdot \text{m}^2 & 0 & 0 \\ -4.93 \times 10^5 \text{ tonne} \cdot \text{m} & 0 & 0 & 0 & 3.86 \times 10^7 \text{ tonne} \cdot \text{m}^2 & 0 \\ 0 & 0 & 0 & 0 & 0 & 0 \end{bmatrix}$$

 T_p : limiting to zero seconds or infinite frequency

$$\begin{bmatrix} 7814 \text{ tonne} & 0 & 0 & 0 & -4.89 \times 10^5 \text{ tonne} \cdot \text{m} & 0 \\ 0 & 7814 \text{ tonne} & 0 & 4.89 \times 10^5 \text{ tonne} \cdot \text{m} & 0 & 0 \\ 0 & 0 & 281 \text{ tonne} & 0 & 0 & 0 \\ 0 & 4.89 \times 10^5 \text{ tonne} \cdot \text{m} & 0 & 3.85 \times 10^7 \text{ tonne} \cdot \text{m}^2 & 0 & 0 \\ -4.89 \times 10^5 \text{ tonne} \cdot \text{m} & 0 & 0 & 0 & 3.85 \times 10^7 \text{ tonne} \cdot \text{m}^2 & 0 \\ 0 & 0 & 0 & 0 & 0 & 0 \end{bmatrix}$$

C.3. Damping matrices

 $T_p : 11s$

$$\begin{bmatrix} 68 \text{ kN/(m/s)} & 0 & 0 & 0 & -2154 \text{ kN/(rad/s)} & 0 \\ 0 & 68 \text{ kN/(m/s)} & 0 & 2154 \text{ kN/(rad/s)} & 0 & 0 \\ 0 & 0 & 6.68 \text{ kN/(m/s)} & 0 & 0 & 0 \\ 0 & 2150 \text{ kN} \cdot \text{m/(m/s)} & 0 & 67841 \text{ kN} \cdot \text{m/(rad/s)} & 0 & 0 \\ -2150 \text{ kN} \cdot \text{m/(m/s)} & 0 & 0 & 0 & 67841 \text{ kN} \cdot \text{m/(rad/s)} & 0 \\ 0 & 0 & 0 & 0 & 0 & 0 \end{bmatrix}$$

 $T_p : 16s$

$$\begin{bmatrix} 18 \text{ kN/(m/s)} & 0 & 0 & 0 & -831 \text{ kN/(rad/s)} & 0 \\ 0 & 18 \text{ kN/(m/s)} & 0 & 831 \text{ kN/(rad/s)} & 0 & 0 \\ 0 & 0 & 1.53 \text{ kN/(m/s)} & 0 & 0 & 0 \\ 0 & 831 \text{ kN} \cdot \text{m/(m/s)} & 0 & 37595 \text{ kN} \cdot \text{m/(rad/s)} & 0 & 0 \\ -831 \text{ kN} \cdot \text{m/(m/s)} & 0 & 0 & 0 & 37595 \text{ kN} \cdot \text{m/(rad/s)} & 0 \\ 0 & 0 & 0 & 0 & 0 & 0 \end{bmatrix}$$

$T_p : 20s$

$$\begin{bmatrix} 6.6 \text{ kN/(m/s)} & 0 & 0 & 0 & -335 \text{ kN/(rad/s)} & 0 \\ 0 & 6.6 \text{ kN/(m/s)} & 0 & 335 \text{ kN/(rad/s)} & 0 & 0 \\ 0 & 0 & 0.3 \text{ kN/(m/s)} & 0 & 0 & 0 \\ 0 & 335 \text{ kN} \cdot \text{m/(m/s)} & 0 & 17053 \text{ kN} \cdot \text{m/(rad/s)} & 0 & 0 \\ -335 \text{ kN} \cdot \text{m/(m/s)} & 0 & 0 & 0 & 17053 \text{ kN} \cdot \text{m/(rad/s)} & 0 \\ 0 & 0 & 0 & 0 & 0 & 0 \end{bmatrix}$$

C.4. Viscous damping matrix

$$\begin{bmatrix} 100 \text{ kN/(m/s)} & 0 & 0 & 0 & 0 & 0 \\ 0 & 100 \text{ kN/(m/s)} & 0 & 0 & 0 & 0 \\ 0 & 0 & 130 \text{ kN/(m/s)} & 0 & 0 & 0 \\ 0 & 0 & 0 & 0 & 0 & 0 \\ 0 & 0 & 0 & 0 & 0 & 0 \\ 0 & 0 & 0 & 0 & 0 & 13,000 \text{ kN} \cdot \text{m/(rad/s)} \end{bmatrix}$$

D

Loadcases

Table D.1: Loadcases triangular configuration

Loadcase	Environmental Conditions	Direction Conditions	Pretension mooring
LC1	1	1	1
LC2	1	2	1
LC3	1	3	1
LC4	2	1	1
LC5	2	2	1
LC6	2	3	1
LC7	3	1	1
LC8	3	2	1
LC9	3	3	1
LC10	1	1	2
LC11	1	2	2
LC12	1	3	2
LC13	2	1	2
LC14	2	2	2
LC15	2	3	2
LC16	3	1	2
LC17	3	2	2
LC18	3	3	2
LC19	1	1	3
LC20	1	2	3
LC21	1	3	3
LC22	2	1	3
LC23	2	2	3
LC24	2	3	3
LC25	3	1	3
LC26	3	2	3
LC27	3	3	3

Table D.2: Loadcases hexagonal configuration

Loadcase	Environmental Conditions	Direction Conditions	Pretension mooring
HLC1	1	1	1
HLC2	1	2	1
HLC3	2	1	1
HLC4	2	2	1
HLC5	3	1	1
HLC6	3	2	1

Table D.3: Parameters for the loadcases

	Hs [m]	Tp [s]	Windspeed [m/s]	Direction [deg]	Horizontal pretension [kN]
1	5	11	15	30	1003
2	8	16	22	60	4019
3	11	20	27	90	633

E

Validation data

E.1. Environmental conditions for the validation cases

Case	Date	Hs	Tp	Wind	Current	Wave-dir	Wind-dir	Curr-dir	Comment
1	2018-03-26 23:30	2.2	10.6	8.5	0.24	14	172	16	
2	2018-01-14 15:40	4.2	8.7	20.4	0.32	165	174	24	
3	2018-04-14 00:40	2.1	10.5	5.2	0.32	107	171	195	
4	2018-02-13 01:20	2.1	6.5	15.5	0.27	201	174	187	
5	2018-02-24 04:50	2.5	7.3	14.1	0.17	164	161	150	
6	2018-01-09 09:40	3.2	9.3	13.9	0.09	131	146	303	
7	2018-01-06 08:00	4.4	10.9	13.7	0.21	17	11	19	
8	2018-07-29 04:00	3.0	7.9	16.6	0.33	161	179	44	
9	2018-05-02 04:00	2.3	6.5	15.6	0.12	185	175	233	
10	2018-01-24 11:30	3.9	8.3	30.0	0.27	174	212	27	Idle
11	2018-01-24 11:40	3.9	8.3	30.3	0.30	175	213	37	Idle

Table E.1: Environmental conditions for the validation cases

E.2. Loads in the delta lines

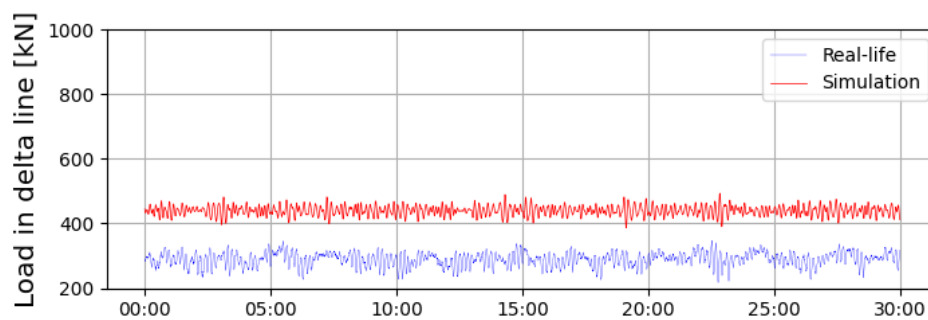


Figure E.1: Load in mooring line 1, delta line 1 for case 1

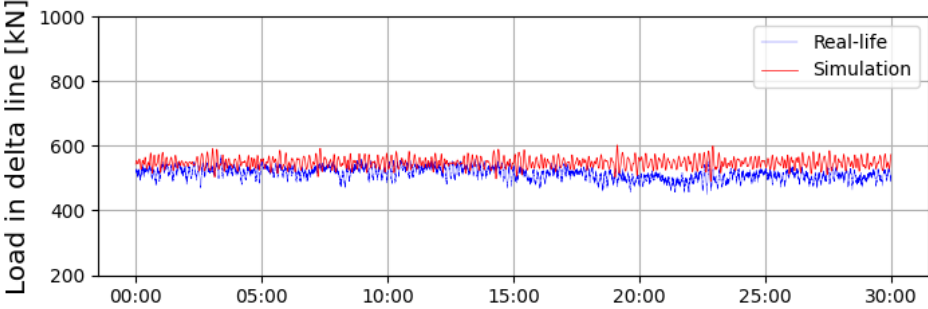


Figure E.2: Load in mooring line 1, delta line 2 for case 1

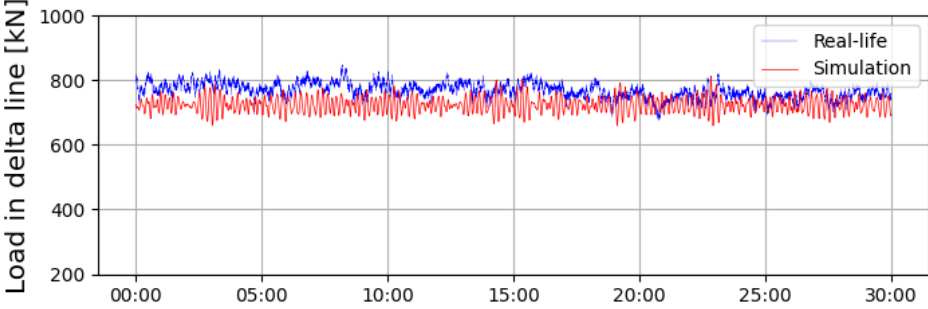


Figure E.3: Load in mooring line 2, delta line 1 for case 1

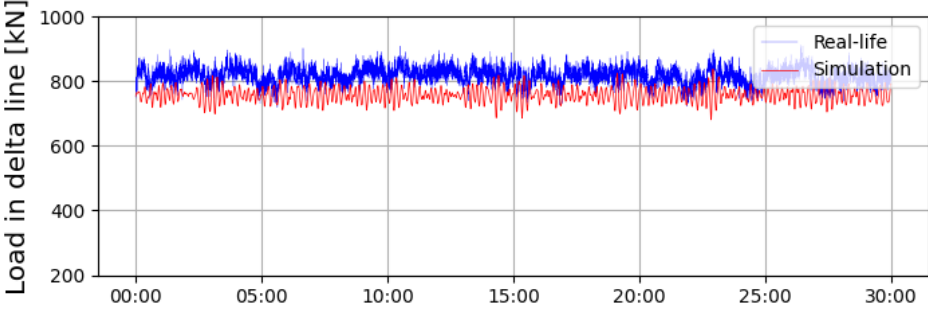


Figure E.4: Load in mooring line 2, delta line 2 for case 1

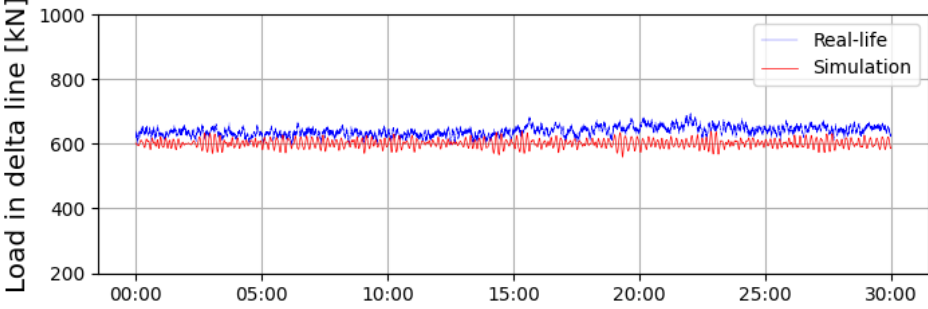


Figure E.5: Load in mooring line 3, delta line 1 for case 1

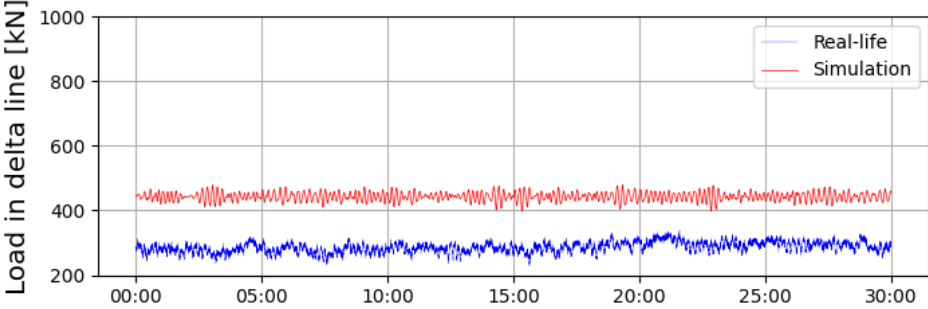


Figure E.6: Load in mooring line 3, delta line 2 for case 1

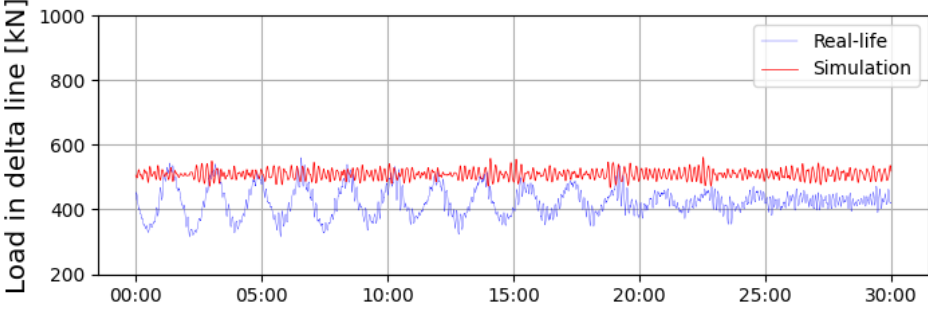


Figure E.7: Load in mooring line 1, delta line 1 for case 3

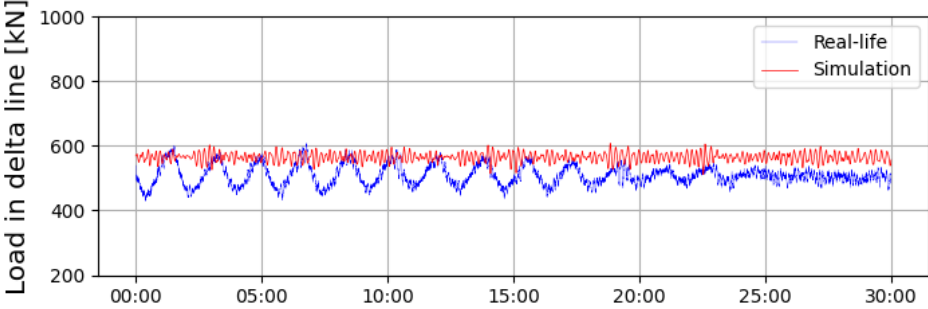


Figure E.8: Load in mooring line 1, delta line 2 for case 3

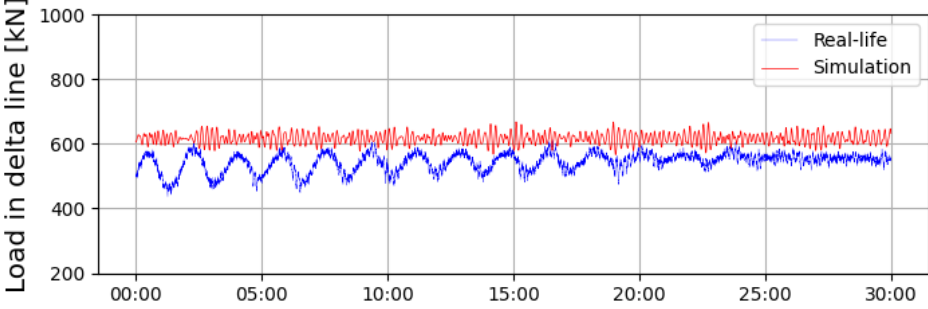


Figure E.9: Load in mooring line 2, delta line 1 for case 3

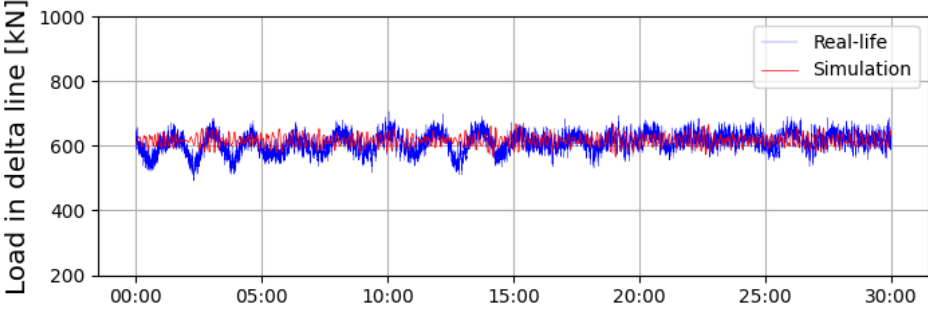


Figure E.10: Load in mooring line 2, delta line 2 for case 3

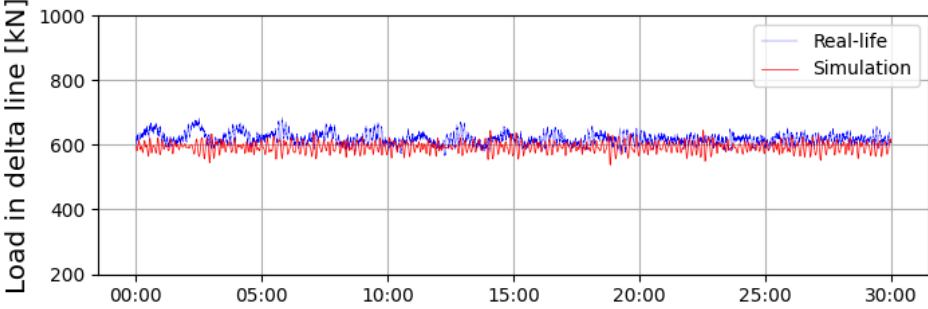


Figure E.11: Load in mooring line 3, delta line 1 for case 3

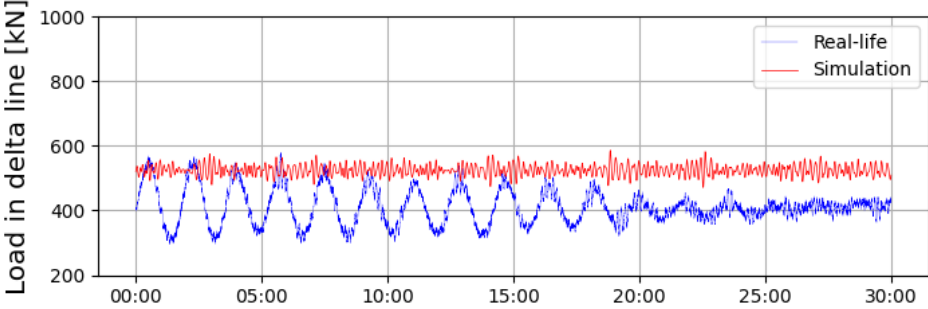


Figure E.12: Load in mooring line 3, delta line 2 for case 3

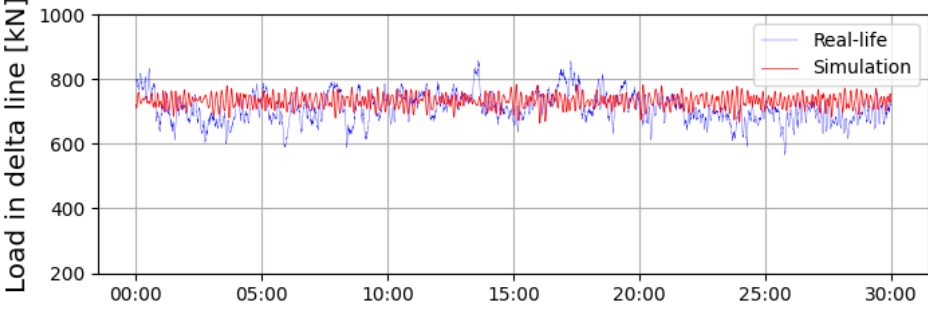


Figure E.13: Load in mooring line 1, delta line 1 for case 7

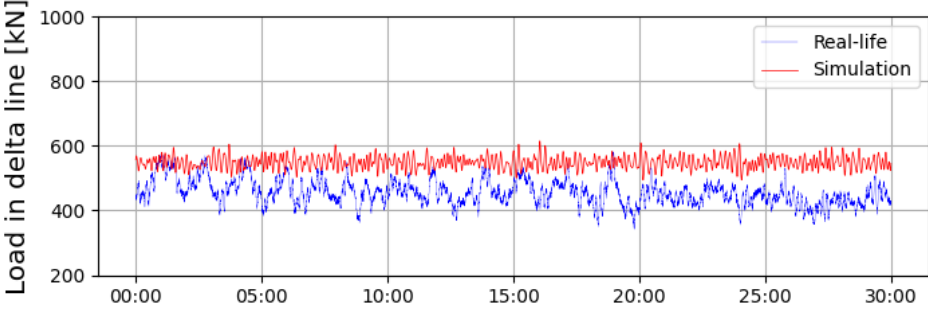


Figure E.14: Load in mooring line 1, delta line 2 for case 7

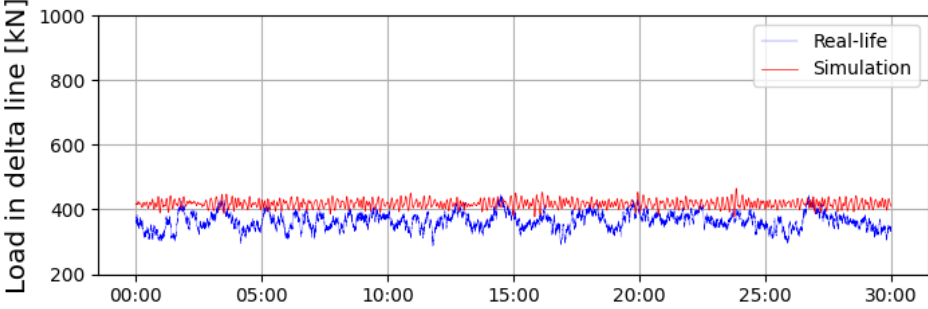


Figure E.15: Load in mooring line 2, delta line 1 for case 7

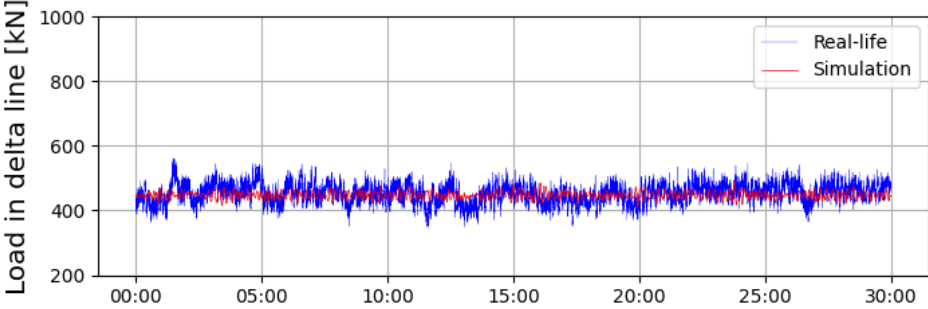


Figure E.16: Load in mooring line 2, delta line 2 for case 7

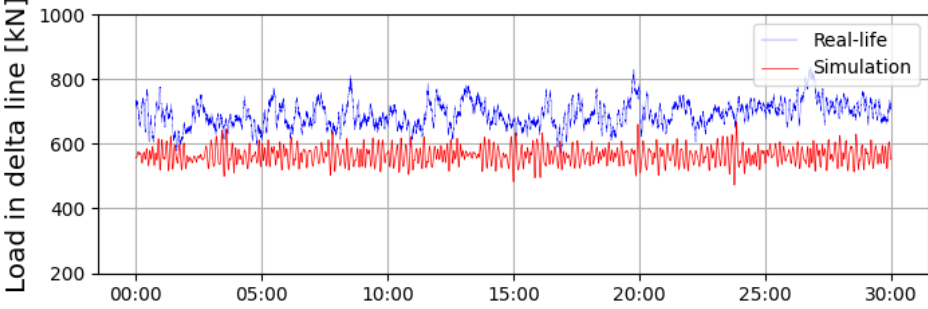


Figure E.17: Load in mooring line 3, delta line 1 for case 7

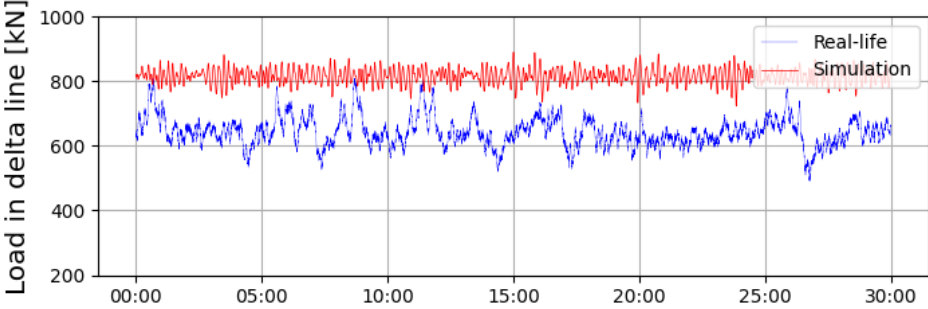


Figure E.18: Load in mooring line 3, delta line 2 for case 7

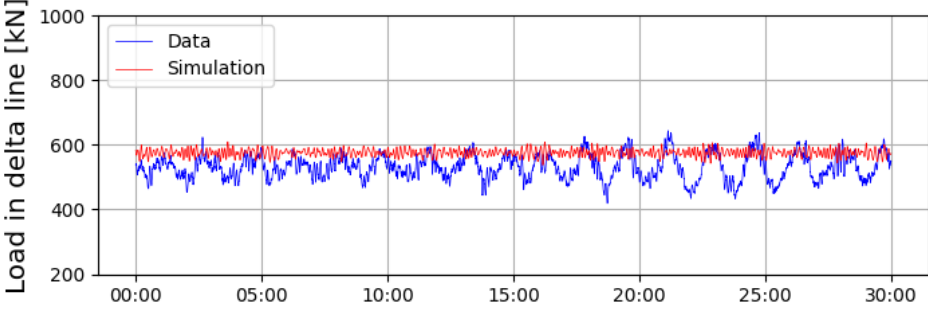


Figure E.19: Load in mooring line 1, delta line 1 for case 11

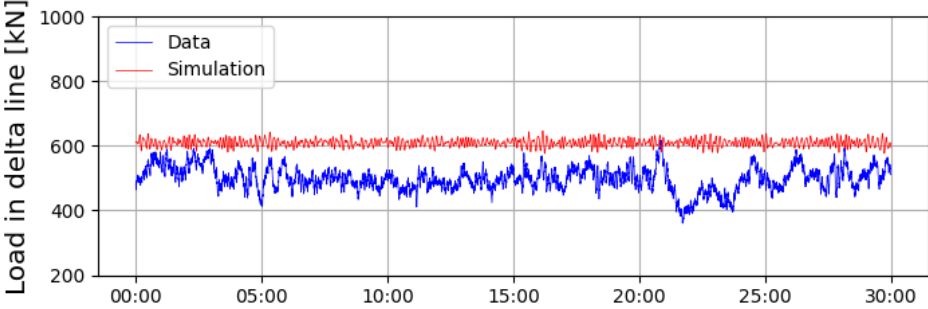


Figure E.20: Load in mooring line 1, delta line 2 for case 11

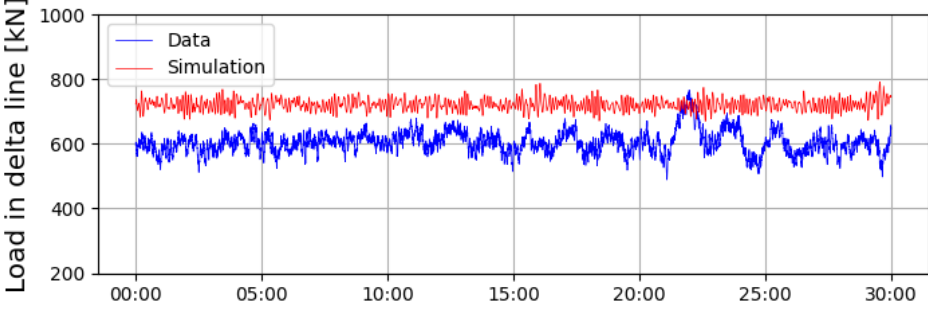


Figure E.21: Load in mooring line 2, delta line 1 for case 11

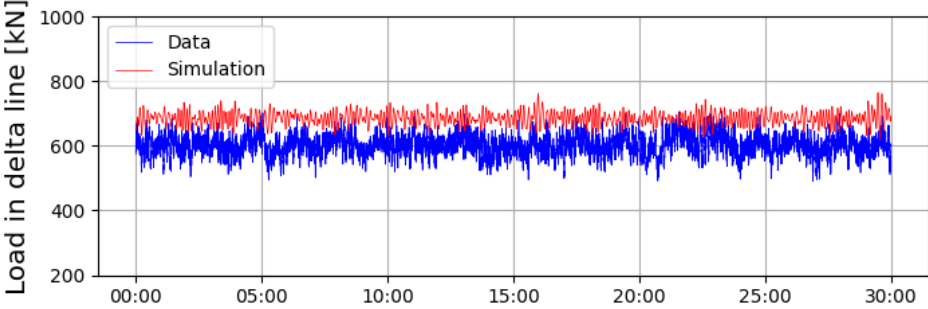


Figure E.22: Load in mooring line 2, delta line 2 for case 11

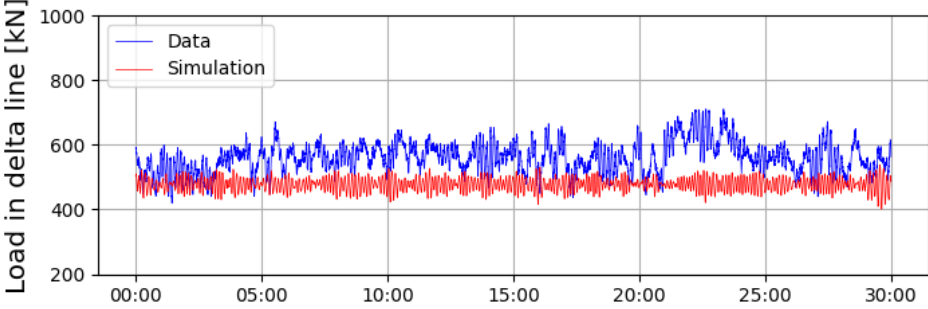


Figure E.23: Load in mooring line 3, delta line 1 for case 11

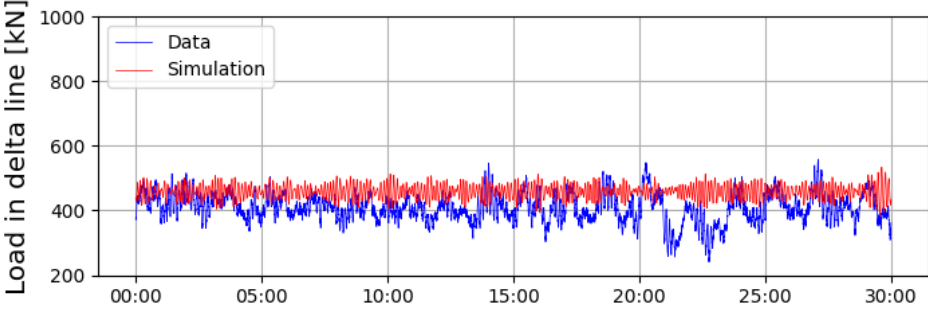
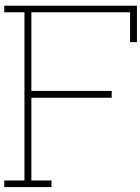
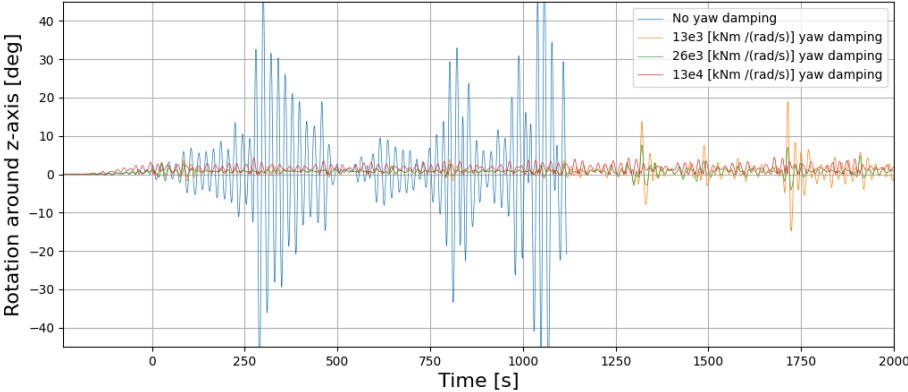


Figure E.24: Load in mooring line 3, delta line 2 for case 11

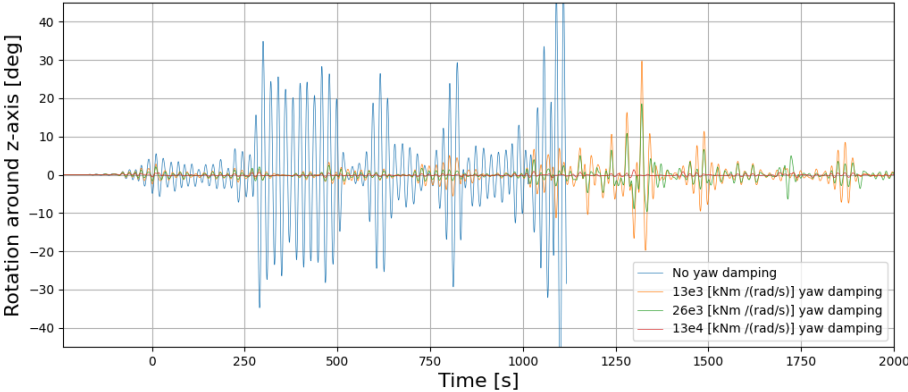


Results graphs

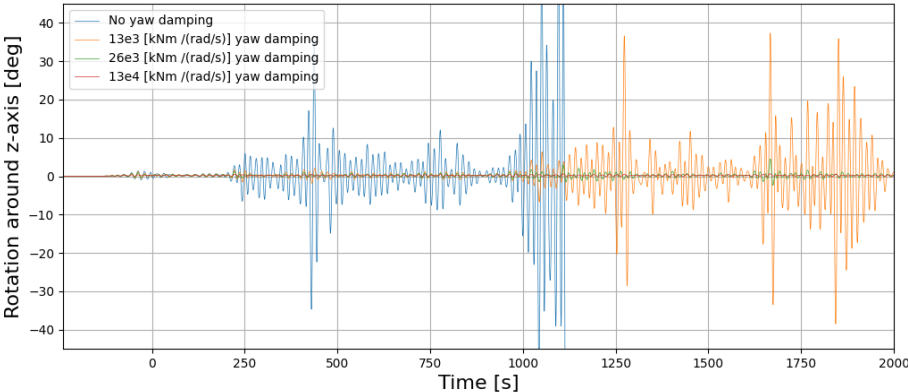
F.1. Graphs viscous damping



(a) Yaw motion green spar floater for different viscous damping



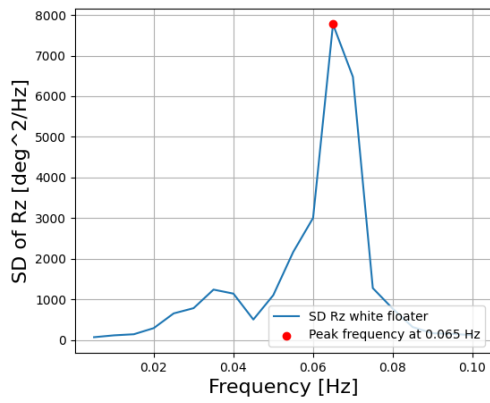
(b) Yaw motion blue spar floater for different viscous damping



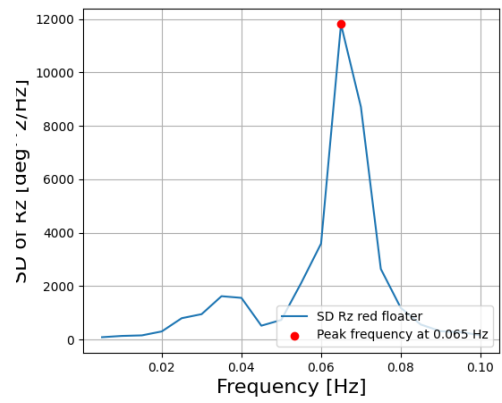
(c) Yaw motion red spar floater for different viscous damping

Figure F.1: Yaw motions for the three spar floaters in the triangular configuration with different viscous damping

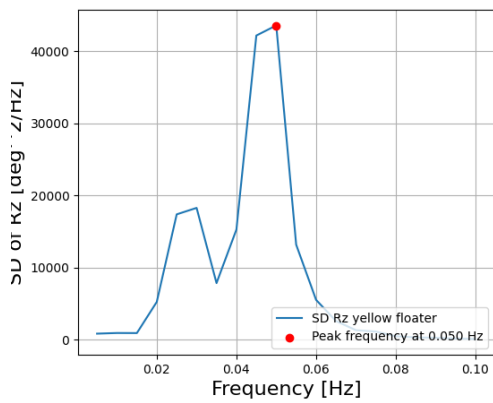
F.2. Spectral density graphs



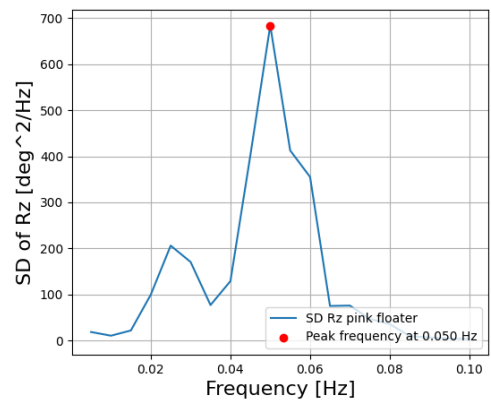
(a) Spectral density Rz white spar floater



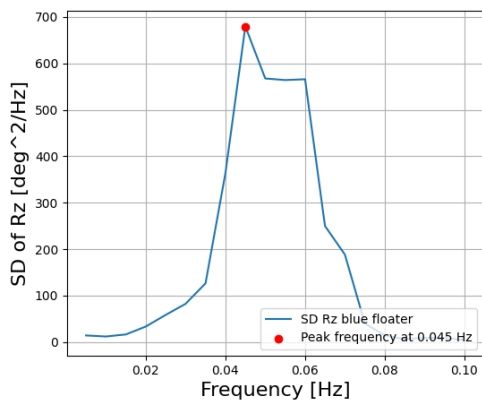
(b) Spectral density Rz red spar floater



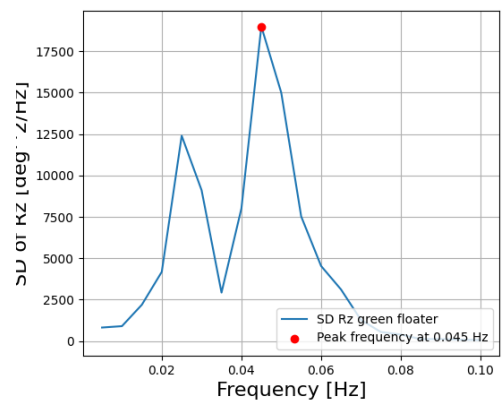
(c) Figure 3



(d) Spectral density Rz pink spar floater

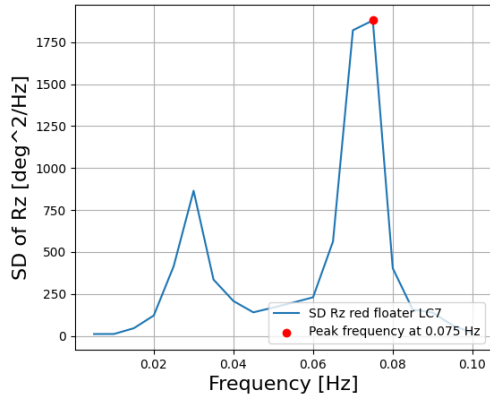


(e) Spectral density Rz blue spar floater

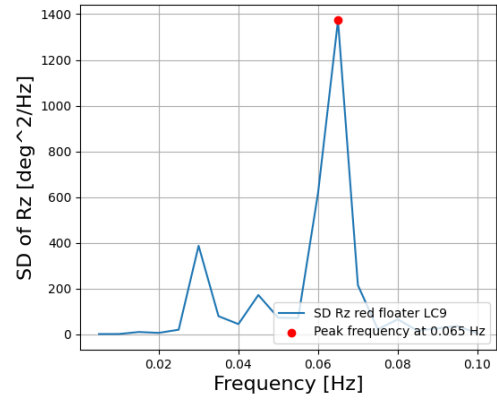


(f) Spectral density Rz green spar floater

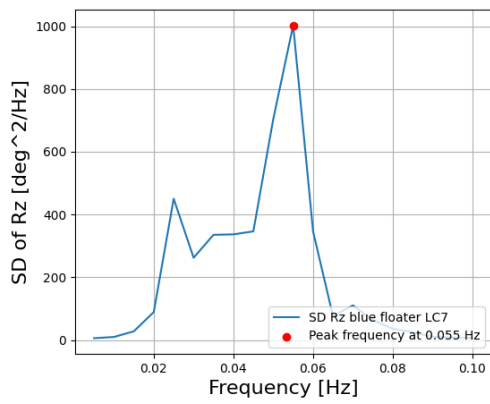
Figure F.2: Spectral densities Rz spar floaters hexagonal configuration



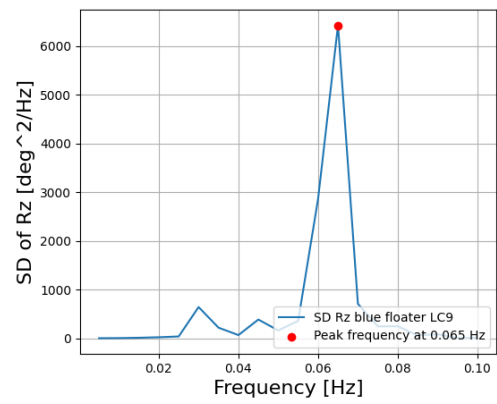
(a) Spectral density Rz red spar floater LC7



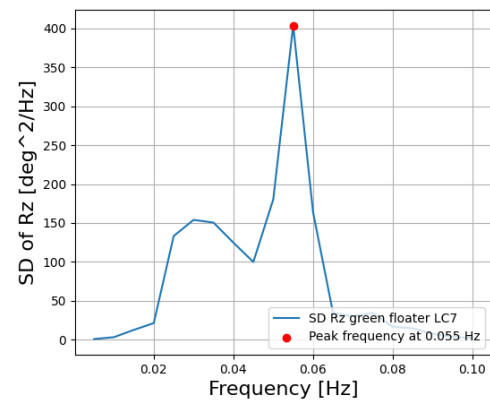
(b) Spectral density Rz red spar floater LC9



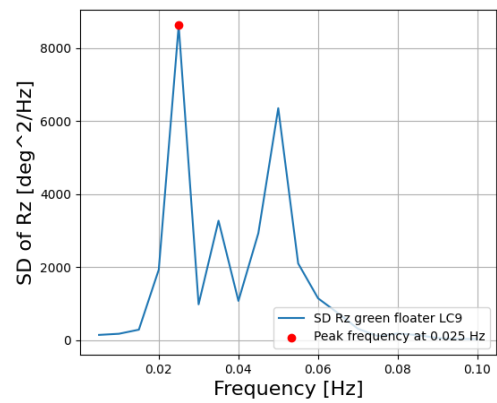
(c) Spectral density Rz blue spar floater LC7



(d) Spectral density Rz blue spar floater LC9



(e) Spectral density Rz green spar floater LC7



(f) Spectral density Rz green spar floater LC9

Figure F.3: Spectral densities Rz spar floaters triangular configuration for two environmental directions